CHARACTERIZING AND CONTROLLING EXTREME OPTICAL NONLINEARITIES IN PHOTONIC CRYSTAL FIBERS

By

SHENGBO XU

A DISSERTATION PRESENTED TO THE GRADUATE SCHOOL
OF THE UNIVERSITY OF FLORIDA IN PARTIAL FULFILLMENT
OF THE REQUIREMENTS FOR THE DEGREE OF
DOCTOR OF PHILOSOPHY

UNIVERSITY OF FLORIDA

2006

This dissertation is dedicated to my family, for their love and support.

ACKNOWLEDGMENTS

I would like to express sincere acknowledgements to my advisor, Dr. David Reitze, for leading me to this exciting field. His experience, expertise and constant wise guidance are invaluable to my doctoral research and the completion of this dissertation. I would also like to thank him for everything he did during my internship at Intel, without his help and encouragement, I could never have this chance to broaden my horizon and expand my expertise. I could not have imagined having a better mentor for my Ph. D.

My thanks go to the fellow graduate students in the group: Xiaoming Wang, Vidya Ramanathan and Jinho Lee, for their open minds, all the supports and helpful discussions. You guys are a great fun team to work with. I would also like to thank the support stuffs in the department, especially Darlene Latimer, for making my life a lot easier outside research.

Finally, I want to thank my parents and my wife Yuanjie Li for their love and encouragement all the way since the beginning of my studies, without their enthusiasms this dissertation could not have been possible. I love you.

TABLE OF CONTENTS

page

LIST OF TABLES

LIST OF FIGURES

Abstract of Dissertation Presented to the Graduate School
of the University of Florida in Partial Fulfillment of the
Requirements for the Degree of Doctor of Philosophy

CHARECTERIZING AND CONTOLLING EXTREME OPTICAL NONLINEARITIES IN PHOTONIC CRYSTAL FIBERS

By

Shengbo Xu

May 2006

Chair: David H. Reitze
Major Department: Physics

The development of the photonic crystal fibers (PCFs or microstructured fibers) has been one of the most intellectually exciting events in the optics community within the past few years. The introduction of air-hole structures in PCFs allows for new degrees of freedom to manipulate both the dispersion and optical nonlinearities of the fibers. Not only the zero group-velocity-dispersion of a PCF can be engineered from 500 nm to beyond 1500 nm, but the extremely high optical nonlinearities of PCFs also lead to ultrabroadband supercontinuum generation (>1000 nm) when pumped by nanoJoules femtosecond Ti:Sapphire laser pulses. Therefore, PCF is an ideal system for investigating nonlinear optics.

In this dissertation, we present results of controlling nonlinear optical processes in PCFs by adjusting the input pulse properties and the fiber dispersion. We focus on supercontinuum, resulting from the extreme nonlinear processes. A simulation tool based

on the extended nonlinear Schrödinger equation is developed to model our experiments and predict output spectra.

To investigate the impact of input pulse properties on the supercontinuum generation, we perform open- and closed-loop control experiments. Femtosecond pulse shaping is used to change the input pulse properties. In the open-loop (intuitively designed) control experiments, we investigate the effects of input pulse spectral phase on the bandwidth of supercontinuum generation. Furthermore, we use phase-sculpted temporal ramp pulses to suppress the self-steepening nonlinear effect and generate more symmetric supercontinuum spectrum. Using the genetic algorithm in closed-loops (adaptive) control experiment to synthesize the appropriate temporal pulse shape, we enhance the supercontinuum generation bandwidth and perform control of soliton self-frequency shift. For both the open- and closed-loop control, simulation results show good agreement compared with the experiment optimized spectra. To our knowledge, this is the first time that femtosecond pulse shaping has been used to control the pulse nonlinear propagations in PCFs.

We also develop a pulse compression model to study how the microstructured fiber dispersion characteristics can affect the supercontinuum temporal compressions. Using numerically simulated dispersion-flattened microstructured fibers at different wavelengths, simulation results show that it is possible to compensate the stable supercontinuum spectral phase and compress the pulse to the few-cycle regime.

CHAPTER 1
INTRODUCTION

Optical fibers have tremendous impact on the modern world. In 1979, progress in the fiber fabrication technology made it possible to manufacturer optical fibers with loss merely 0.2 dB/km in the 1550 nm wavelength region [1]. Conventional optical fibers are made of fused silica, which has zero group velocity material dispersion wavelength at 1300 nm. The design of the conventional fiber (e.g., core size, refractive index differences between core and cladding) can shift the zero GVD of the fiber to 1550 nm. Optical fibers at this wavelength with low loss and small dispersion have revolutionized the telecommunications industry [2]. Meanwhile, optical fibers have also rapidly progressed the field of nonlinear fiber optics in the last 30 years [3]. Various nonlinear effects, including self-phase modulation, stimulated Raman scattering, parametric four-wave-mixing, etc., have been studied extensively and the theory is well established by now.

The emergence of photonic crystal fibers (PCFs) [4, 5] and their ability to easily generate supercontinuum have been one of the hottest topics in the optics community for the past several years. Photonic crystal fibers (e.g., microstructured fibers and photonic bandgap fibers) exhibit many special properties when compared to that of conventional fibers, mainly because of their unique design structures. Microstructured fibers [6] consist of a solid silica core surrounded by an array of air holes running along the fiber and its light guiding mechanisms is similar to that of conventional fibers. Photonic bandgap fibers (PBFs) [7] have a hollow core surrounded by the air-holes array, and the

guided light is confined to the low index core by the photonic bandgap effect. The air-holes configuration of the PCFs gives a whole new level of freedom in the fiber design. Many PCFs that exhibit novel dispersion and nonlinear properties have been developed by carefully choosing the core size and air-filling fraction (air-hole size and pitch) of the PCFs. In particular, the zero group velocity dispersion wavelength of the PCFs can be engineered at any wavelength from 500 nm to above 1500 nm, which evidently make the Ti:Sapphire laser wavelength in the anomalous dispersion region of the PCFs. The tailorable dispersion properties and high nonlinearities exhibit in the PCFs lead to the ultrabroadband supercontinuum generation. The impact of the supercontinuum generation on the optical community is phenomenal and it has led to a renewed interest in investigating nonlinear fiber optics. In principle, the nonlinear mechanisms that lead to the supercontinuum generation for PCFs are similar to that of conventional fibers. However, the unique dispersion properties and high nonlinearities of the PCFs determine that the magnitude of the nonlinear processes is large in magnitude and the required power for the input pulse to generate sufficient broadband spectrum is much less than that for the conventional fibers. As a result, over an octave-spanning ultrabroadband supercontinuum can be generated using Ti:Sapphire laser pulses with only nJ-level energy [6].

The PCFs and the subsequent supercontinuum generation exhibit unparalleled properties, well beyond what conventional fiber can ever offer. These properties have distinguished themselves through a wide range of applications in the ever-widening area of science and technology. For example, the most important application of the supercontinuum generation lies in the field of optical metrology. The ultrabroad

bandwidth coherent light makes the measurement of relative frequency offsets possible. This led to the work of absolute optical frequency measurement which is one of the subjects of the 2005 Nobel price in Physics by Theodor Hänsch and John L. Hall [8].

Because supercontinuum generation in PCFs is a nonlinear effect in the extreme sense of "nonlinear," researchers have put a great deal of effort to understand what kind of nonlinear interactions in the PCFs lead to the supercontinuum generation, what role and order and magnitude they are playing in the generation process. During this exploration, various simulation models have definitely played an important role. Simulation models based on the nonlinear Schrödinger equation are by far the most successful methods and have been well accepted by many researchers [9]. Now, it is commonly understood that supercontinuum generation is initialized by high order soliton generation, followed by the soliton splitting among with other nonlinear effects [10, 11]. Meanwhile, however, broadband noise of the supercontinuum generation in the PCFs has led to amplitude fluctuations as large as 50% for certain input pulse parameters [12]. Furthermore, supercontinuum generation is found to be extremely sensitive to the input pulse noise. Both the experiment and simulation have revealed that for the reasonable power fluctuations of the laser systems, sub-nanometer spectral structures of the supercontinuum vary from shot to shot [9, 13]. This problem greatly limits the application scope of supercontinuum generation.

Although controlling supercontinuum generation (or any nonlinear process) is in general difficult because of the intrinsic fiber nonlinearity response to the input electric field, control of the supercontinuum generation is desirable and it will allow us to tailor the supercontinuum properties to suit for a specific application. It is also commonly

understood that the supercontinuum generations depend critically on both the input pulse properties and PCF characteristics. In this dissertation we will present the results of controlling supercontinuum generations using both of these two approaches. In particular, we investigate how the femtosecond pulse shaping can be used to control the supercontinuum generation by controlling the evolution of the temporal and spectral structure of optical pulses propagating in the microstructured fibers. We also simulate the supercontinuum pulse compression using the dispersion-flattened microstructured fibers.

Femtosecond pulse shaping promises great advantages to the fields of fiber optics and photonics, ultrafast spectroscopy, optical communications and physical chemistry. In general, the pulse characteristics (e.g., pulse intensity modulation and pulse spectral chirp) one wants to use for a specific application may be different from what a laser system can directly offer. On the other hand, when optical pulses travel in a complex optical system, the optical components in the system will introduce significant amount of dispersion, which compromises the characteristics of ultrashort optical pulses. All these problems can be solved using femtosecond pulse shaping to alter the pulse intensity temporal profile for a specific application. Meanwhile, working with adaptive search algorithms (such as genetic algorithms) to efficiently search all the possible solutions for a direct target, adaptive pulse shaping has proven to be very useful when an intuitive driving pulse can not be directly derived.

In this dissertation, we use femtosecond pulse shaping to change the input pulse properties and control the supercontinuum generations in the PCFs. Depending on whether an intuitive driving pulse is available, we present the results of both open- and closed-loop (adaptive) control experiments. Open-loop control schematics utilize

underlying physics to derive a suitable driving pulse. The experiment results of pulse shaping that change both the pulse spectral chirps and pulse intensity modulation (ramp pulse) are presented. Meanwhile, a simulation model based on the extended nonlinear Schrödinger equation using a split-step Fourier method is developed. We use this simulation tool to model our experimental control results. We use the adaptive pulse shaping to control supercontinuum bandwidth and soliton self-frequency shift. Again, the nonlinear Schrödinger equation modeled results for the adaptive pulse shaping helps us to understand why the final derived driving pulse can interact with the PCF and achieve the desired supercontinuum. To our knowledge, this is the first demonstration on how femtosecond pulse shaping can be used to control the evolution of the temporal and spectral structure of optical pulses propagating in PCFs.

Pulse compression is one of the most obvious, yet most challenging, applications of the supercontinuum generations in PCFs. Because of the ultra-broad bandwidth of the supercontinuum, pulse duration of the compression results is expected to be within the few-optical-cycle regime. However, the fluctuations in the spectral phase of the supercontinuum generation for the input pulse and propagation noise greatly increase the difficulties of performing the pulse compression. Experimentally, the coherence of the supercontinuum (used as a benchmark for the potential compressibility of the supercontinuum generation) can be severely compromised due to the inherent fluctuations of the input pulse. However, theoretical investigations have revealed that the coherence increases linearly with a shorter fiber propagation length [14] and there exists an optimum compressed distance at which compressed pulses with negligible fluctuation and time shift can be obtained [15]. Therefore all current pulse compression experiments

involve a short piece of PCF, ranging from several mm to cm. Pulse characterization techniques such as FROG or SPIDER are used to retrieve the spectral phase of the supercontinuum. Current state of art compression experiment uses femtosecond pulse shaping (or even adaptive pulse shaping) with adequate phase compensation to generate compress pulses several femtoseconds in duration [16, 17].

Meanwhile, the dispersion of the PCFs is one of the main reasons that lead to the instabilities of the supercontinuum spectral phase, as evidenced by the increase in coherence when shortening the pulse propagation length. The unique PCFs structures provide another way to alter (minimize) the fiber dispersion even for a wide wavelength (over 300 nm, see Reeves et al. [18]). We use the simulation model based on the idea of dispersion-flattened PCF to perform the pulse compression for the controlled supercontinuum generation.

The layout of this dissertation is described as follows. An introduction of the PCFs will be given in chapter 2, including the discussion of both the dispersion properties and nonlinearities of the conventional fibers and PCFs, as well as a layout of the nonlinear fiber optics: the extended nonlinear Schrödinger equation. In chapter 3 we will give an overview of some relevant experimental techniques, which consist of the methods of generating, characterizing, and temporal tailoring ultrashort pulses. Open-loop investigations of the influences of input pulse linear and quadratic chirp on the supercontinuum generation will be given in chapter 4, as well as the control results of suppressing the pulse self-steepening nonlinear effect in the supercontinuum generations. Chapter 5 discusses the closed-loop control experiments (adaptive pulse shaping), including the investigations of spectral broadening enhancement, soliton self-frequency

shift. We will discuss our supercontinuum generation pulse compression model and results using the dispersion-flattened PCF in chapter 6. Finally, in chapter 7, we present our conclusions.

CHAPTER 2
PHOTONIC CRYSTAL FIBERS

The main work of this dissertation concerns the application of shaped femtosecond optical pulses in controlling the nonlinear interactions in photonic crystal fibers (PCFs). In this chapter, we will first summarize the propagation, dispersion and optical nonlinearities in conventional fibers in section 2.1. This will lead to the discussion of nonlinear fiber optics (the extended nonlinear Schrödinger equation), including various nonlinear effects that govern the nonlinear pulse propagation in the conventional fibers and PCFs. In section 2.3, we will discuss various configurations of PCFs that have different fiber properties (nonlinearities and dispersion) and applications, followed by the discussion of mechanisms of supercontinuum generations and its applications.

2.1 Conventional Fiber Optics – Propagation, Dispersion, and Optical Nonlinearities

Pulses propagating in the PCFs follows the same dispersion and nonlinear propagation principles as that in the conventional fibers, although the nonlinearities exhibited in the PCFs are in much larger scales because of the special configuration (smaller mode volume, zero dispersion point, dispersion profile) of PCFs. Nonlinear pulse propagation in the conventional fibers has been studied extensively over the past few decades and the theories are well established. Therefore, before beginning a discussion of PCFs, it is important to understand how conventional fibers work. Section 2.1 will give an overview of dispersion effect and optical nonlinearities in conventional fibers, followed by the well-established nonlinear pulse propagation theory (the nonlinear Schrödinger equation) in section 2.2.

Uncladded glass fibers were first fabricated in the 1920s. It was not until the 1950s that people realized that using a cladding layer is extremely important to the fiber characteristics and fiber optics experienced a phenomenal rate of progress [19]. In the simplest form, conventional optical fibers are cylindrical dielectric waveguides (fiber core), made of low loss materials such as silica glass, surrounded by a cladding layer made of doped silica glass with slight lower constant refractive index than the core. Such fibers are generally referred as step-index fibers. In graded-index fibers, the refractive index of the core decreases gradually from center to the core boundary. Modern fabrication technology produces fiber optical loss close to the theoretical minimum [1] (0.2 dB/km at 1550 nm), a loss level determined by the fundamental Rayleigh scattering in silica. The availabilities of low loss silica fibers led to a revolution in the field of optical fiber communications as well as the emergence in the field of nonlinear fiber optics.

Guidance of light in optical fibers based on total internal reflection (TIR); that is, an optical fiber consists of a central core of refractive index n_1, where the light is guided, surrounded by an outer cladding area of a slightly lower refractive index n_2, the light rays with incident angle on the core-cladding interface greater than the critical angle $\theta_c = \sin^{-1}(n_2 / n_1)$ experience TIR. Therefore, the light rays incident on the fiber end satisfied the TIR can be guided without any refractive loss in the fiber core. The fiber can guide the light rays with different incident angles (different modes), as long as TIR is satisfied.

In general, however, the TIR theory is too simplistic to explain fiber modes and propagation. One needs to start from Maxwell's equations and apply appropriate fiber

boundary conditions to derive the mode solutions of the wave equation. A brief discussion will be given in this section. Interested readers can refer to Buck [20] and Agrawal [3] for more detailed discussion.

Starting from Maxwell's equations in the optical fibers,

$$\begin{aligned} \vec{\nabla} \times \vec{E} &= -\partial \vec{B} / \partial t, \\ \vec{\nabla} \times \vec{H} &= \partial \vec{D} / \partial t, \\ \vec{\nabla} \cdot \vec{D} &= 0, \\ \vec{\nabla} \cdot \vec{B} &= 0, \end{aligned} \tag{2.1}$$

where $\vec{E}$ and $\vec{H}$ are electric and magnetic field vectors, $\vec{D}$ and $\vec{B}$ are electric and magnetic flux densities. Using the constitutive relations in optical fibers given by

$$\begin{aligned} \vec{D} &= \varepsilon_0 \vec{E} + \vec{P}, \\ \vec{B} &= \mu_0 \vec{H}, \end{aligned} \tag{2.2}$$

one finds

$$\nabla \times \nabla \times \vec{E} = -\frac{1}{c^2} \frac{\partial^2 \vec{E}}{\partial t^2} - \mu_0 \frac{\partial^2 \vec{P}}{\partial t^2}. \tag{2.3}$$

In general, the polarization $\vec{P}$ can be expanded in powers of the electric field $\vec{E}$

$$\vec{P} = \varepsilon_0 \left(\chi^{(1)} \cdot \vec{E} + \chi^{(3)} \vdots \vec{E}\vec{E}\vec{E} + \cdots \right). \tag{2.4}$$

$\chi^{(3)}$ is the third order susceptibility that governs the third order nonlinear effects. In general, $\chi^{(2)}$ (second order susceptibility) should also be present in equation 2.4. However, even order nonlinear effects disappear for silica fiber as required by symmetry and are not included in the equation.

Solving equation 2.3 requires the nonlinear $\chi^{(3)}$ effect to be included, which will lead to the derivation of the extended nonlinear Schrödinger equation discussed in the next section.

For the mode propagation discussion, one can treat the nonlinear effect as a small perturbation to the total induced polarization and simply ignore it in the following discussion. This lead to the electric field wave equation

$$\nabla^2 \tilde{\vec{E}} + n^2(\omega)\frac{\omega^2}{c^2}\tilde{\vec{E}} = 0, \tag{2.5}$$

where $n(\omega)$ is the refractive index of the fiber and $\tilde{\vec{E}}(r,\omega)$ is the Fourier transform of $\vec{E}(r,t)$. For an optical fiber, the natural symmetry is that of a cylinder. Thus, expressing the wave equation (2.5) in cylindrical coordinates ρ, ϕ and z, and assuming

$$\tilde{E}_z(r,\omega) = A(\omega)F(\rho)\exp(\pm im\phi)\exp(i\beta z), \tag{2.6}$$

where A is a normalization constant, β is the propagation constant (βz represents the phase of the field), and m is an integer, $F(\rho)$ is the solution of the well-known differential equation for Bessel functions

$$\frac{d^2F}{d\rho^2} + \frac{1}{\rho}\frac{dF}{d\rho} + (n^2k_0^2 - \beta^2 - \frac{m^2}{\rho^2})F = 0, \tag{2.7}$$

with solutions taking the form

$$\begin{aligned} F(\rho) &= J_m(\kappa\rho), \quad \rho \le a, \\ F(\rho) &= K_m(\gamma\rho), \quad \rho \ge a, \end{aligned} \tag{2.8}$$

where a is the fiber core radius and

$$\begin{aligned} \kappa^2 &= n_1^2k_0^2 - \beta^2, \\ \gamma^2 &= \beta^2 - n_2^2k_0^2. \end{aligned} \tag{2.9}$$

Similar derivations for the magnetic field from equation 2.5 to 2.9 can be obtained. Simply applying the boundary conditions that the tangential components of the electric

field and magnetic field are continuous across the core-cladding interface, one can derive the eigenvalue equation as

$$\left[\frac{J_m^{'}(\kappa a)}{\kappa J_m(\kappa a)}+\frac{K_m^{'}(\gamma a)}{\gamma K_m(\gamma a)}\right]\left[\frac{J_m^{'}(\kappa a)}{\kappa J_m(\kappa a)}+\frac{n_2^2}{n_1^2}\frac{K_m^{'}(\gamma a)}{\gamma K_m(\gamma a)}\right]=\left(\frac{m\beta k_0(n_1^2-n_2^2)}{an_1\kappa^2\gamma^2}\right)^2. \qquad (2.10)$$

In general, the eigenvalue equation 2.10 has several solutions for β for each integer m. It is customary to express these solutions by β_{mn}, where both m and n are integers and represent mode indeces. Each eigenvalue β_{mn} corresponds to one specific mode supported by the fiber. The corresponding modal field distribution can be obtained from equation 2.6. There are two types of mode, designated as HE_{mn} and EH_{mn}. For $m=0$, these modes corresponds to the fundamental transverse-electric (TE) and transverse-magnetic (TM) mode; whereas for $m>0$, all six components of the electromagnetic field are nonzero.

The number of modes supported by the fiber depend on its design parameter, namely the core radius and the core-cladding index difference n_2-n_1. It is useful to define a normalized frequency parameter and it has a straightforward way to determine how many eigenmodes an optical fiber can support. Normalized frequency parameter can be expressed as,

$$V=ak_0\sqrt{n_1{}^2-n_2{}^2}, \qquad (2.11)$$

where $k_0=2\pi/\lambda_0$ is wave number corresponds to the central wavelength of the incident light in the vacuum. Using the normalized parameter, a complete set of eigenmodes can be derived. When the normalized frequency parameter is smaller than 2.405 (from the solution of the first zero of the Bessel function), only the fundamental mode is allowed to

propagate, in which case the fiber is called a single-mode fiber. Note that with fixed fiber parameters, there is a lowest wavelength (cutoff wavelength) that the fiber can sustain single-mode fiber. Single-mode fibers are widely used in pulse applications.

The description of fibers includes two physical effects, fiber dispersion and nonlinear effects, both of which will be laid out in more detail in the next section. Below, we will take an example of optical fibers in telecommunications to briefly illustrate how these two aspects influence the performance of high speed optical networks.

Optical fibers have revolutionized the telecommunications industry within the last decade. Single-mode fiber allows for a higher capacity to transmit information via the light pulses because it can retain the fidelity of each light pulse over longer distances. Supercontinuum generation offers the possibility of generating over 1000 dense wavelength-division multiplexing channels (DWDM) using only one single laser source, using over 10 THz single mode fiber bandwidth [21]. However, fiber dispersion, apart from the optical loss, will damage the fidelity and cause inter-symbol interference (ISI). Modern communication requires a high data transmission rate when using a single-mode fiber, thus short pulses are preferred.

For propagating optical pulses, the mode-propagation constant β solved in equation (2.10) can be expanded in a Taylor series at ω_0 where the pulse spectrum is centered,

$$\beta(\omega) = n(\omega)\frac{\omega}{c} = \beta_0 + \beta_1(\omega - \omega_0) + \frac{1}{2}\beta_2(\omega - \omega_0)^2 + \cdots, \qquad (2.12)$$

where

$$\beta_m = \left(\frac{d^m \beta}{d\omega^m}\right)_{\omega=\omega_0} \qquad (m = 0, 1, 2, ...). \qquad (2.13)$$

The parameters β_1 and β_2 can be expressed as

$$\beta_1 = \frac{1}{v_g} = \frac{n_g}{c} = \frac{1}{c}(n + \omega\frac{dn}{d\omega}),$$
$$\beta_2 = \frac{1}{c}(2\frac{dn}{d\omega} + \omega\frac{d^2n}{d\omega^2}), \tag{2.14}$$

where n_g is group index and v_g is group velocity. The envelope of an optical pulse moves at the group velocity v_g and the phase of underlying field evolves at phase velocity v_p, as shown in figure 2.1. β_2 is commonly referred as group velocity dispersion (GVD), and the convention is that $\beta_2 > 0$ for normal dispersion and $\beta_2 < 0$ for anomalous dispersion. GVD is mainly responsible for pulse broadening. The dispersion parameter D (in the unit of $ps/km \cdot nm$) is commonly used in the fiber optics literature in stead of β_2. Its relation to β_2 is

$$D = \frac{d\beta_1}{d\lambda} = -\frac{2\pi c}{\lambda^2}\beta_2. \tag{2.15}$$

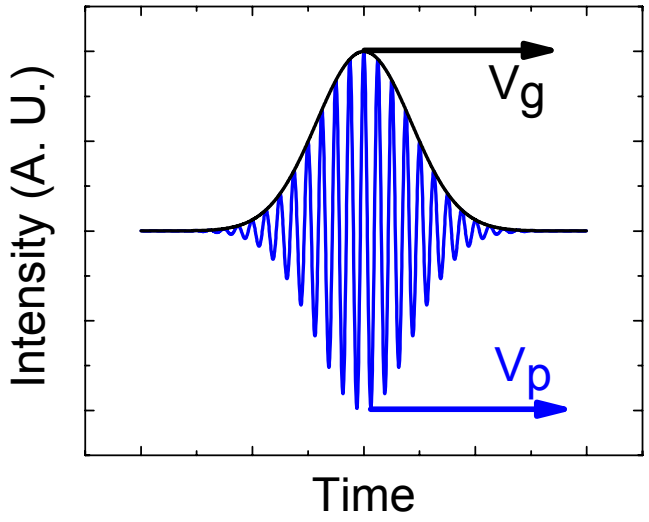

Figure 2.1: Illustrations of the group velocity for pulse envelope and phase velocity of the underlying field.

β_3 is the third order dispersion (TOD) and its inclusion is necessary when the pulse wavelength approaches the zero GVD point.

Dispersion causes individual frequency components in a pulse to travel at a different velocity; thus, the individual frequency components making up the pulse separate and "diphase". As a result, the pulse duration increases as it propagates. For telecommunication applications, information distortion can be manifested in the temporal spreading and consequent overlap of individual pulses, thus ISI. This effect can be minimized by choosing the central wavelength of the pulse close to the zero dispersion point of the group velocity dispersion.

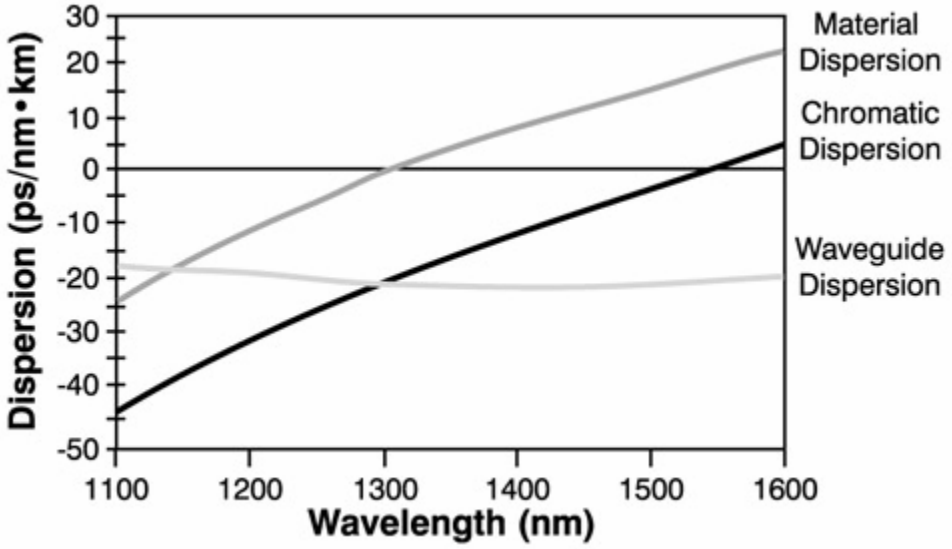

Figure 2.2: Illustration of material dispersion for fused silica (zero GVD at 1.3 μm) as well as the waveguide dispersion contribution to the chromatic dispersion. Refer to Goff and Hansen [71].

There are three contributions to the fiber dispersion (chromatic dispersion). The first is the material dispersion, which manifests itself through the frequency dependence of the material refractive index ($n(\omega)$, as noted above). This intrinsic dispersion is determined by the material itself, and we have little control over this. The zero group

velocity dispersion (GVD) for the fused silica is 1.3 μm , as shown in figure 2.2. Waveguide dispersion comes about because of the effective mode index of the dielectric waveguiding is wavelength dependent as well. The waveguide dispersion contribution can easily be manipulated. Changing the core size and the refractive index difference between the core and cladding can evidently change the waveguide dispersion. (As we will discuss below, the waveguide dispersion contribution of photonic crystal fibers is extremely larger compared to that of conventional fiber). Figure 2.2 illustrates that the zero chromatic dispersion of the fiber is shifted from the 1.3 μm zero material dispersion point to 1.55 μm because of the waveguide dispersion contribution, thus the name zero-dispersion-shifted fiber. Furthermore, some fiber designs allow the waveguide dispersion to be customized and fine tuned. For example, graded-index fiber allows the refractive index of the core being designed in the form of a parabolic curve and decreasing toward the cladding [22]. Dispersion-compensating fiber (DCF) can be designed to have the exact opposite dispersion of the fiber that is used in a transmission system, therefore nullifying the dispersion caused by that fiber [23, 24]. However, all the designs and controls of the waveguide dispersion have limitations, with zero group velocity dispersion between 1.3 and 1.55 μm . The last contribution to the fiber dispersion is the modal dispersion, which results from the group velocity differences between different guided modes in a multi-mode fiber. Modal dispersion cannot exist in a single-mode fiber, since by definition only one mode propagates in the fiber.

Pulses propagating in optical fibers also experience nonlinear effects, apart from the dispersion effects. The magnitude of nonlinear effects is directly related to the input pulse peak intensity. These nonlinear effects can be generalized as generating new

frequency components (colors), or characterized as effects corresponding to different nonlinear mechanisms such as self-phase modulation (SPM), stimulated Raman scattering (SRS), etc. All these different nonlinear effects will be discussed in details in the next section. Since SiO_2 is a symmetric molecule, second order $\chi^{(2)}$ effects such as second-harmonic generation and sum-frequency generation cannot happen in silica fiber as required by symmetry. The nonlinearities in optical fibers are small, but they accumulate as light passes through many kilometers of fiber, especially when dense wavelength-division multiplexing (DWDM) [25] packs many channels into a single fiber. Unfortunately, the optical nonlinearities in a fiber are also governed by a material-dependent parameter, the nonlinear index of refraction n_2, and therefore selection of the material forces us to live with the size of the nonlinearity. For fused silica, $n_2 = 2 \times 10^{-16} cm^2 / W$. However, a fascinating manifestation of the fiber nonlinearity occurs through temporal optical solitons [26] (discussed in details in the next section), formed as a result of the perfect balance between the anomalous group velocity dispersion and SPM nonlinear effect. Soliton effects are evidently extremely useful for the telecommunication application. The shape of the fundamental soliton does not change during propagation as a result of GVD and SPM completely balancing each other at a critical power (the *fundamental soliton power)*, whereas higher-order solitons (providing certain higher input power levels) propagate in a periodic evolution pattern with original shape recurring at multiples of the soliton period.

On the other hand, optical fibers allow high optical intensities to be maintained over relatively long fiber length; therefore can be used to enhance the nonlinear effects. For example, zero-dispersion-shifted fiber can have the zero GVD at 1550 nm where

fiber has minimum loss (0.2 dB/km). As the intense pulse propagates in an optical fiber, SPM along with all other nonlinear effects can lead to significant broadening of the optical spectrum; this very broad and continuous spectrum is called supercontinuum (SC). SC generation was first observed in 1970 by focusing picosecond pulses into a glass sample as a nonlinear medium [27], SPM is the primary mechanism that led to spectral broadening. Since then, the nonlinear media used for SC generation has evolved from gases and liquids to optical fibers. Figure 2.3 is an example of supercontinuum generation in conventional fiber. A supercontinuum bandwidth of 210 nm was generated by using 500 fs pulse with over 4 m conventional fiber and the energy per pulse is 90 pJ [28].

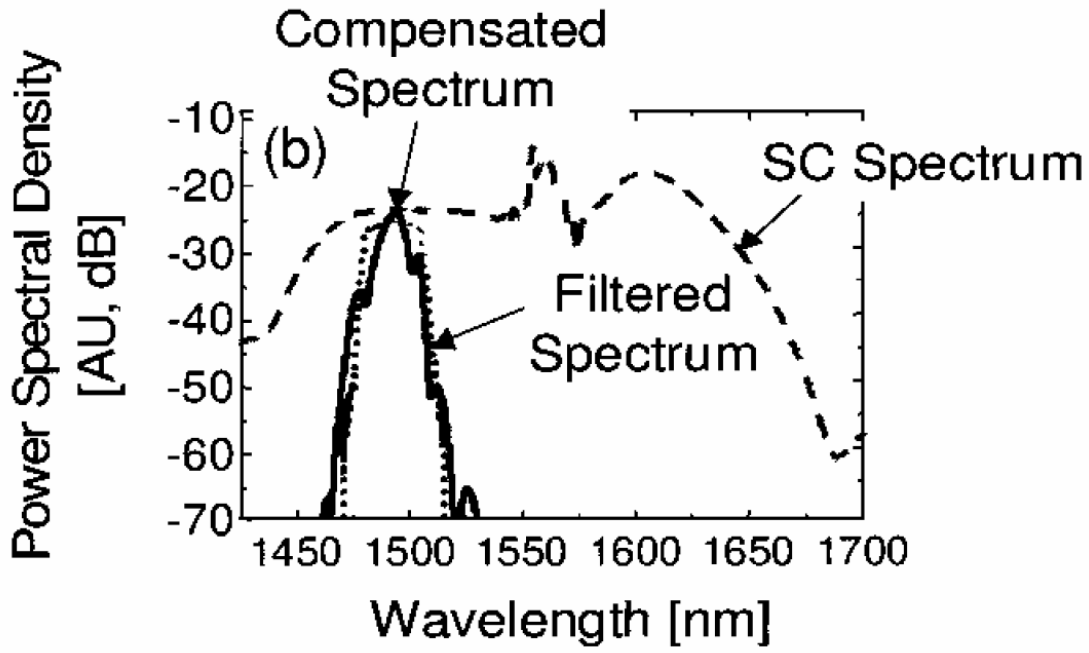

Figure 2.3: An example of 210 nm supercontinuum generation in the conventional fiber (dashed line). Refer to Nowak et al. [28].

The high effective nonlinearities of optical fibers have led to a dramatic reduction in the pump power requirements compared with those for other nonlinear media. The high optical intensities maintained over the propagation length will trigger a variety of

other nonlinear effects other than SPM, generating a much broader SC with a relative low input pulse peak level. As a result, SC generation is much easier and has important applications in various fields such as telecommunication, optical metrology and medical science, some of which will be discussed in more details in section 3.

The problem of wavelength mismatch between optical fiber's zero group velocity dispersion wavelength and femtosecond laser's operating wavelength great limits the application of conventional optical fibers being used for SC generation. Ti:sapphire lasers are the most predominately used tunable solid-state ultrafast laser, with a central wavelength around 800 nm and optical bandwidths of over 300 nm, producing pulses in duration from a few femtoseconds to several picoseconds and pulse energies from nJ for the oscillators to as much as 25J for amplified sources, which makes Ti:Sapphire a great candidate as the laser source for the SC generation. However, at this wavelength range, silica fiber has such a large material dispersion (100 ps/km.nm) that the contribution of waveguide dispersion can essentially be ignored [3]. As a result, the initial input pulse with a short duration and intensive peak power experiences massive fiber dispersion, the pulse duration broadens very fast and the peak intensity drops dramatically. Therefore, the breadth and strength of the significant nonlinear interactions as well as the abilities of generating a very broad supercontinuum for Ti:Sapphire ultrafast laser source are greatly diminished.

The key technological advance which has revolutionized the ability to investigate fiber dispersion and more importantly optical nonlinearities is the invention of photonic crystal fibers. We will discuss this in great detail in section 2.3, but first will layout the theory of nonlinear fiber optics.

2.2 Nonlinear Fiber Optics: Extended Nonlinear Schrödinger Equation

For an understanding of the nonlinear phenomena in optical fibers as well as the mechanisms that leads to supercontinuum generation, it is necessary to consider the theory of electromagnetic wave propagation in dispersive nonlinear media, in particular, optical fibers. Before specifically focusing on photonic crystal fibers, in this section we review pulse propagation in optical fibers from a general perspective.

This section follows closely to the Agrawal's "Nonlinear Fiber Optics" [3]. In a frame of reference moving at the group velocity of the pulse, an extended nonlinear Schrödinger equation (NLSE) that governs the optical pulse propagation in single-mode fibers can be derived under the slowly varying envelope approximation ($\Delta\omega/\omega << 1$) as

$$\frac{\partial A}{\partial z}+\frac{\alpha}{2}A-\sum_n \frac{i^{n+1}}{n!}\beta_n\frac{\partial^n A}{\partial T^n}=i\gamma\left(1+\frac{i}{\omega_0}\frac{\partial}{\partial T}\right)\left(A(z,T)\int_{-\infty}^{\infty}R(T')\left|A(z,T-T')\right|^2 dT'\right) \quad (2.16)$$

where $A(z,t)=A_0(z,t)\cdot e^{i\phi(z,t)}$ is the intensity temporal profile of the pulse, α is the fiber loss, β -terms correspond to the chromatic dispersion (CD) of the fiber. The mode propagation constant is

$$\beta(\omega)=n(\omega)\frac{\omega}{c}=\sum\frac{\beta_m}{m!}(\omega-\omega_0)^m, \quad (2.17)$$

where $\beta_m=\left(\frac{d^m\beta}{d\omega^m}\right)_{\omega=\omega_0}$ and describes the wave-vector of the light in the fiber. $\gamma=\frac{n_2\omega_0}{cA_{eff}}$ is the nonlinear parameter, a very important parameter that determines the magnitude of the optical nonlinearity.

The predominant nonlinearity for silica fiber is the third order nonlinearity, governed by $\chi^{(3)}$. since the second-order nonlinearity dispears due to the inversion sysmmetry at the silica molecular level and the magnitudes of higher-order nonlinearities

are too small for silica. The third-order nonlinear susceptibility is responsible for elastic nonlinear processes such as self-phase modulation (SPM), cross-phase modulation (CPM), four-wave mixing (FWM) and third-harmonic generation (THG). The nonlinear-index coefficient n_2 is related to $\chi^{(3)}$ as

$$n_2 = \frac{3}{8n_0}\mathrm{Re}(\chi^{(3)}), \tag{2.18}$$

where n_0 is the linear refractive index.

Elastic nonlinear processes correspond to photon-photon interactions and no energy is exchanged between the electromagnetic field and the dielectric medium. THG and FWM are usually not efficient in optical fibers, unless special efforts are made to achieve phase matching. Nonlinear fiber optics also involves the stimulated inelastic scattering in which the optical field transfer part of its energy to the nonlinear medium via photon-phonon interactions. These phenomena includes stimulated Raman scattering (SRS) and stimulated Brillouin scattering (SBS).

The right hand side of the extended NLSE (Eq. 2.16) accounts for the nonlinear response of the fiber. The response function $R(t)$ can be written as

$$R(t) = (1 - f_R)\delta(t) + f_R h_R(t), \tag{2.19}$$

where f_R=0.15 represents the fractional contribution of the delayed Raman response. The Raman response function $h_R(t)$ takes an approximate analytic form as (τ_1=12.2 fs and τ_2=32 fs)

$$h_R(t) = \frac{\tau_1^2 + \tau_2^2}{\tau_1 \tau_2}\exp(-t/\tau_2)\sin(t/\tau_1). \tag{2.20}$$

There are two very important length scales in nonlinear fiber optics: the dispersion length

$$L_D = T_0^2 / |\beta_2|, \tag{2.21}$$

and the nonlinear length

$$L_{NL} = 1/(\gamma P_0). \tag{2.22}$$

L_D and L_{NL} provide the length scales over which dispersive or nonlinear effects become dominant for pulse evolution.

For pulses shorter than 5 ps but wide enough to contain many optical cycles (width>>10 fs), the extended nonlinear Schrödinger equation can be simplfied as

$$\frac{\partial A}{\partial z} + \frac{\alpha}{2} A - \sum_n \frac{i^{n+1}}{n!} \beta_n \frac{\partial^n A}{\partial T^n} = i\gamma \left(|A|^2 A + \frac{i}{\omega_0} \frac{\partial}{\partial T} (|A|^2 A) - T_R A \frac{\partial |A|^2}{\partial T} \right), \tag{2.23}$$

using a Taylor-series expansion such that

$$|A(z, T - T')|^2 \approx |A(z,T)|^2 - T' \frac{\partial}{\partial T} |A(z,T)|^2 , \tag{2.24}$$

and

$$T_R \equiv \int_{-\infty}^{\infty} tR(t)dt . \tag{2.25}$$

The term proportional to β_3 governs the effects of 3rd order dispersion and become important for untrashort pulses because of their wide bandwidth. The term proportional to β_2 is responsible for group velocity dispersion (GVD). It causes *temporal pulse broadening* when an unchirped pulse propagates in a single-mode fiber. Higher order dispersion become dominant when the input pulse central wavelength is near the zero GVD fiber dispersion or when the bandwidth of the pulse becomes a significant fraction of the central frequency. The term proportional to $|A|^2 A$ is responsible for SPM nonlinear effect, a phenomenon that leads to *spectral broadening* of optical pulses. In the anomalous-dispersion regime of an optical fiber, interplay between GVD and SPM can cooperate in such a way that the pulse propagates as an optical soliton. In the normal-

dispersion regime, the combined effects of GVD and SPM can be used for pulse compression. The term proportional to ω_0^{-1} is responsible for self-steepening (SS) and shock formation. The last term proportional T_R to is responsible for self-frequency shift (SFS) induced by intrapulse Raman scattering.

A fascinating manifestation of the fiber nonlinearity occurs through optical solitons, formed as a result of the interplay between the nonlinear and dispersive effects, i.e., anomalous fiber dispersion. A soliton is a special kind of wave packet that can propagate undistorted over long distances. If we define a parameter N as

$$N^2 = L_D / L_{NL} = \gamma P_0 T_0^2 / |\beta_2|, \tag{2.26}$$

the integer values of N are found to be related to the soliton order. In time domain, the solution to the nonlinear Schrödinger equation for pure soliton propagation produces a solution of the form $A(t) = \sec h(t)$, as the solution given by Zakharov and Shabat using the inverse scattering method in 1971 [29]. The soliton order N is determined not only by the characteristics of input pulse (T_0, P_0 and γ), but also the properties of the fiber itself (γ and β_2). Only a certain combination of these parameters can reach a soliton solution, given by an integer value of N. Note that to form a higher order soliton, the input peak power required increases quadratically, which is in turn more difficult. The shape of the fundamental soliton (N=1) does not change during propagation, whereas higher-order solitons propagate in a periodic evolution pattern with original shape recurring at multiples of the soliton period $z_0 = L_D \cdot \pi / 2$. As shown in figure 2.4 (a), fundamental soliton propagates in the fiber without distortion as GVD and SPM complete balance each other. For the higher order soliton (figure 2.4 (b)), SPM dominates initially

but GVD soon catches up and leads to the pulse contraction; therefore higher-order solitons propagate in a periodic evolution pattern with original shape recurring at multiples of the soliton period. From a physical point of view, soliton is generated because of the interplay between self-phase modulation and anomalous group velocity dispersion. When the soliton pulse propagates through the fiber, self-phase modulation generates new frequency components that are red-shifted near the red-end and blue-shifted near the blue-end of the spectrum. As the red components travel slower than the blue components in the anomalous dispersion regime, self-phase modulation leads to a pulse narrowing effect which counteracts group velocity dispersion's pulse broadening effect. By carefully choosing self-phase modulation and anomalous group velocity dispersion parameters, the pulse itself can become a soliton by adjusting itself to a hyperbolic-secant shape during propagation to make such cancellation as complete as possible.

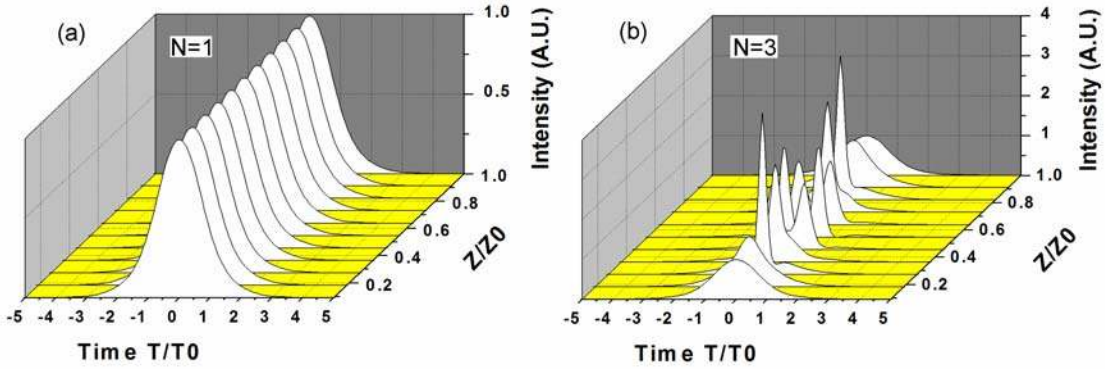

Figure 2.4: Temporal evolution over one soliton period for the first-order and the third-order soliton. (a) The first order soliton (fundamental soliton) propagates without distortion. (b) The third order soliton repeats itself over one soliton period.

Two other important nonlinear effects occurring during pulse propagation are self-steepening and self-frequency shift induced by intrapulse Raman scattering. Self-steepening results from the intensity dependence of group velocity in such a way that the

peak moves at a lower speed than the wings in time domain. As the pulse propagates along the fiber, the temporal shape becomes asymmetric, with its peak shifting toward the trailing edge [Fig. 2.5 (a)]. As a result of self-steepening, the trailing edge becomes steeper and steeper as the pulse propagates which implies larger spectral broadening on the blue side as self-phase modulation generates blue components near the trailing edge. Intrapulse Raman scattering affects the pulse spectrum in such a way that the Raman gain amplifies the low frequency components of a pulse by transferring energy from the high-frequency components of the same pulse. As a result, the pulse spectrum shifts toward the low-frequency (red) side as the pulse propagates inside the fiber, a phenomenon referred as the self-frequency shift [Fig. 2.5 (b)].

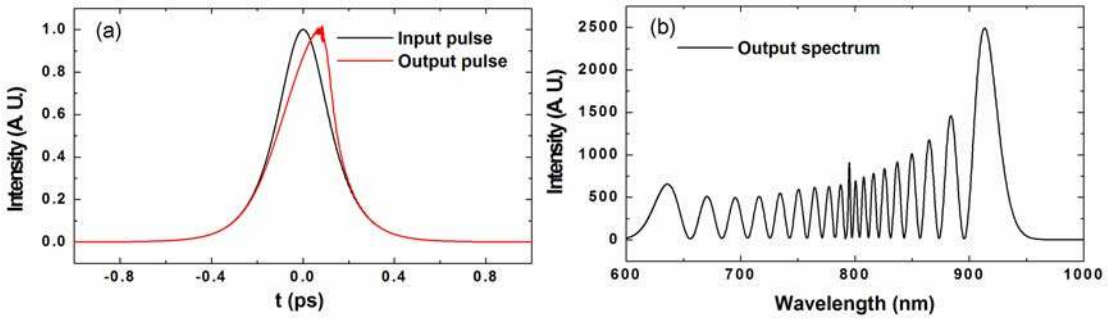

Figure 2.5: Illustrations of self-steepening and self-frequency shift nonlinear effects. a) Self-steepening effect in a nondispersive fiber propagation case. b) Spectrum showing the combined effects of self-steepening and self-frequency shift, the spectral modulation is induced by self-phase modulation.

2.3 Supercontinuum Generations in Photonic Crystal Fibers

Supercontinuum generations in photonic crystal fibers results from high nonlinearities and low fiber dispersion properties of the photonic crystal fibers. In this section we will first discuss various types of PCFs that have different dispersion and nonlinear properties, followed by the fascinating supercontinuum generation and applications.

2.3.1 Photonic Crystal Fibers

The idea of photonic crystal fibers (PCFs) can be traced back to early 1970s [30], when it was suggested that a cylindrical Bragg waveguide with a central core surrounded by rings of high- and low-refractive index might be produced. However, it was not until 1990s when the advances in the technology enabled the fabrication of these complex waveguide structures [4]. It is not an overstatement to say that the development of photonic crystal fibers (PCFs) is one of the most exciting events in optics for the past few years. Its impact on the optics community has been phenomenal and has led to a renewed interested in investigating nonlinear optical phenomena.

PCFs may be divided into two categories: microstructured fibers, in which light is guided in a solid core by the similar principle as that of conventional fibers, and photonic bandgap fibers where the guided light is confined to the low index (hollow) core by the photonic bandgap (PBG) effect.

Microstructured fibers consist of a solid silica core surrounded by an array of air holes running along the fiber, as shown in figure 2.6 (a). Since the microstructured cladding area (the microstructured air-filled region) is a mixture of silica and air holes, an effective refractive index is used to calculate the modal properties [32]. Light can still be guided inside the core according to the principle of total internal reflection as in standard optical fibers because the cladding has a lower effective refractive index than the solid core.

Photonic bandgap fibers exhibit a hollow core or a core made of a dielectric whose refractive index is lower than the silica refractive index [Fig. 2.6 (b)]. The guiding mechanism of the photonic bandgap fibers differs dramatically from the microstructured

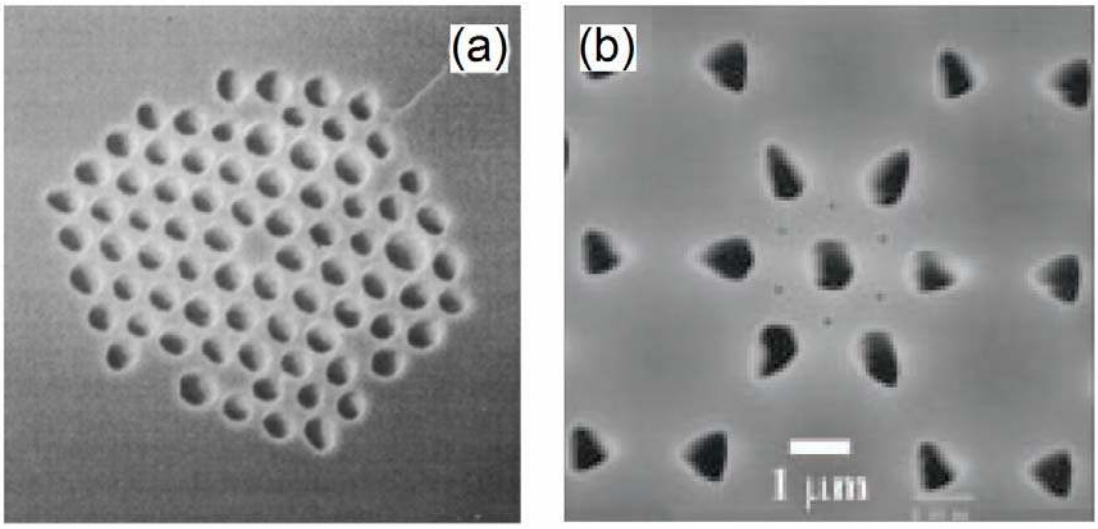

Figure 2.6: Cross-section electron micrograph of microstructured fiber and photonic band-gap fiber. (a) Microstructured fiber, refer to Ranka et al. [5]. (b) Photonic band-gap fiber, refer to Russell [31]. The darker spots with different shapes in both figures are air holes.

fiber and conventional fibers. In photonic bandgap fibers, the periodicity of the air-hole lattice enables to trap the light in the core by two-dimensional photonic bandgaps [33]. The term photonic crystal comes from the analogy between electrons in the periodic potential of a semiconductor crystal and photons in a periodic index profile (formed by a regular air hole pattern). Similarly, photonic bandgap results from the well-known Bloch Theorem, which in turn means no light propagation modes are allowed in the photonic bandgap. As a result, only light with a given wavelength range can be guided in the hollow or dielectric core, as the PBG effect makes propagation in the microstructured cladding region impossible [7].

The fabrication process of the PCFs is a basic stack-and-draw method [31]. First, capillary tubes and rods made of silica are stack together. In this step, an arrangement of the capillary tubes allows changing the air silica structure, therefore, providing the control flexibility of effective index of the cladding area. The PCFs are then fabricated by

feeding the stack into a hot furnace with a certain heating temperature at a proper speed, much in the same manner as conventional fibers. Various PCFs with complex air hole structures can be fabricated with different dispersion and nonlinear properties that are well suited for intended applications.

Photonic crystal fibers exhibit many unique features when compared to standard optical fibers. The introduction of air-holes structure allows new degrees of freedom to manipulate both the dispersive and nonlinear properties of the PCFs. Many parameters can affect properties of the PCFs dramatically. These parameters include the size and shape of air-holes, air filling fraction, the choices of material used to fabricate PCFs as well as the dielectric core of photonic bandgap fibers.

A detailed discussion of photonic bandgap crystals and fibers is beyond the scope of this dissertation, and can be found in Cregan et al. [7] and Knight et al. [34]. Only the properties of microstructured fiber will be discussed in the following section.

The fiber mode theory describe in section 3.1 has found to be quite useful for describing mode propagation properties of the microstructured fiber. However, due to the intrinsic structure differences between the microstructured fibers and conventional fibers, it is crucial to be able to model the microstructured fiber in more rigorous ways, i.e., it requires field analysis using the exact boundary conditions of the microstructured air-holes configuration. These microstructured fiber modal methods include beam propagation method [35], effective index modal [36], scalar beam propagation method [37] and vectorial plane-wave expansion method [38], multipole expansion method [39] and finite-element method [40, 41], etc. As a result, a large number of new microstructured fibers have been designed with novel waveguide properties suitable for a

wide range of applications. For instance, the effective index method allows rigorous calculation of effective refractive index of the cladding, which in this case is usually wavelength-dependent. The normalized frequency parameter V for a conventional fiber can eventually exceed single-mode limit of 2.405, providing a short wavelength and a large core radius. However, properly choosing the air-filling fraction of the microstructured fiber (defined as the ratio of the hole diameter d to the pitch of the lattice Λ), the normalized frequency parameter V can stay constant even at short wavelengths [42] or even with a large core radius [43, 44]. Making this constant V smaller than 2.405, a microstructured fiber can sustain the single-mode property over a very broad wavelength range, thus the name of endless single-mode microstructured fiber [42]. Other microstructured fibers that exhibit interesting properties include single-polarization single-mode PCF [45], highly birefringent PCF [46] and cobweb microstructured fiber [47], etc.

As mentioned in section 2.1, conventional fibers have large normal material dispersion at the Ti:Sapphire laser operating wavelength, with modifications of the waveguide properties having little impact. This large normal dispersion greatly diminishes the magnitude of nonlinear effects and impairs the possibilities of supercontinuum generation. The invention of microstructured fibers has opened new opportunities for exploring nonlinearities in microstructured fibers.

The strong wavelength dependence of the effective refractive index of the cladding of microstructured fibers leads to a new range of dispersion properties that cannot be achieved with conventional fibers. The waveguide dispersion properties of the microstructured fibers strongly depend on the air-filling fraction and core size. For

instance, increasing the air-filling fraction as well as decreasing the core size can dramatically increase the waveguide dispersion, allowing compensation of the silica material dispersion at any wavelengths range from 500 nm to beyond 1500 nm [48]. As a result, the zero group velocity dispersion wavelength can be pushed far below 800 nm [Fig. 2.7 (a)], making the Ti:Sapphire laser operating wavelength in the anomalous dispersion region and soliton propagation, for the first time, available for the visible

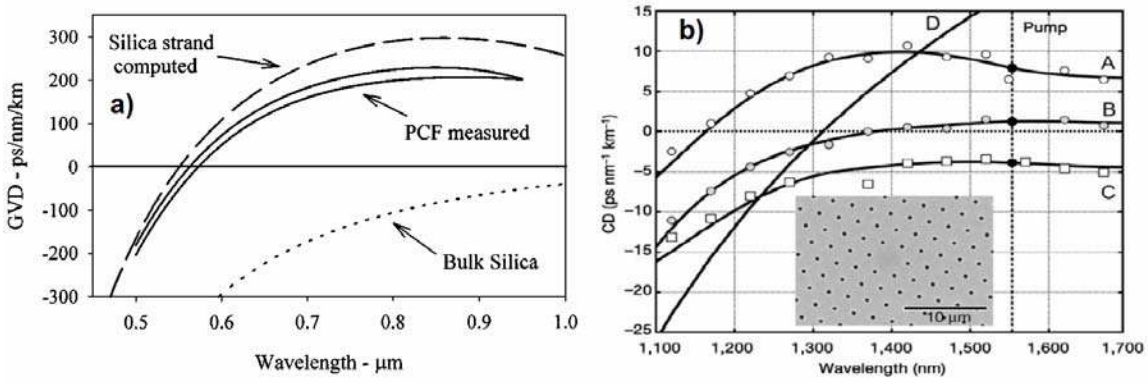

Figure 2.7: Illustrations of tailorable dispersion properties of microstructured fibers. (a) Measured dispersion curve of a microstructured fiber with zero GVD below 600nm, refer to Knight et al. [48]. (b) Microstructured fiber with a flat dispersion (curve B) by adjusting pitch size as 2.41 μm and air-filling fraction as 0.22, refer to Reeves et al. [18].

wavelength range. Furthermore, by choosing the proper fiber parameters such as air hole size and pitch, one can easily tailor the dispersion characteristics of the microstructured fiber, such as fabricating fibers with very low and flat dispersion over a relatively broad wavelength range [18], e.g., dispersion-flattened microstructured fiber (DFMF), as we can see in curve B in Fig. 2.7 (b). In general, a proper choice of air-hole sizes and pitches enable to engineer a variety of dispersion profiles. This precise control of the fiber dispersion greatly expands the horizon of fiber applications and allows customized fiber with tailored dispersion characteristics being used in a desired application.

The interest in microstructured fibers is not only because of their special waveguide properties, but more importantly, lies in the fact of the significant nonlinearities that exhibit in the microstructured fibers. Actually, the high efficiency of various nonlinear effects is directly related to the unique waveguide properties that allow the engineering of the zero dispersion point and tailoring the dispersion profile, in addition to the extremely small core area. When laser pulses with their central wavelength near the zero dispersion point propagate in microstructured fibers, the high peak intensities dominate the pulse evolution and $L_{NL} << L_D$. In particular, the pulse can still maintain a short duration and high intensity over a much longer fiber propagation length, inducing an extraordinary larger nonlinearity when compared to conventional fibers. As a result, this greater nonlinearity reduces the threshold pulse energy for observing nonlinear effects and nonlinear optical processes take place on a *grand scale* in microstructured fibers. These different nonlinear processes, including SPM, SRS, FWM and THG, have been observed in the microstructured fiber [49-52]. Furthermore, combining with the tailorable dispersion characteristics of the microstructured fibers, a number of dramatic nonlinear optical effects are observed at ~800 nm that were not previously possible or have been severely limited [6]. On the other hand, large core single-mode microstructured fibers can also be fabricated to minimize the nonlinear optical effects.

Now let us turn to the most dramatic and amazing of the nonlinearities, ultra-broadband supercontinuum generation.

2.3.2 Supercontinuum Generation in Microstructured Fibers

Supercontinuum generation is definitely the most fascinating outcome of the invention of microstructured fibers. In particular, it results directly from the combination of microstructured fibers' enhanced nonlinearities and unique engineer-able dispersion

properties. Ranka's postdeadline talk at Conference on Laser and Electro-Optics (CLEO) in 1999 as well as the paper published in early 2000 have a tremendous impact on the research conducted on fiber design probabilities, fiber dispersions and nonlinearities, as well as many important applications in the past few years. In this paper [6], an ultra broadband supercontinuum ranges from 400 nm to 1600 nm (figure 2.8) is generated in a

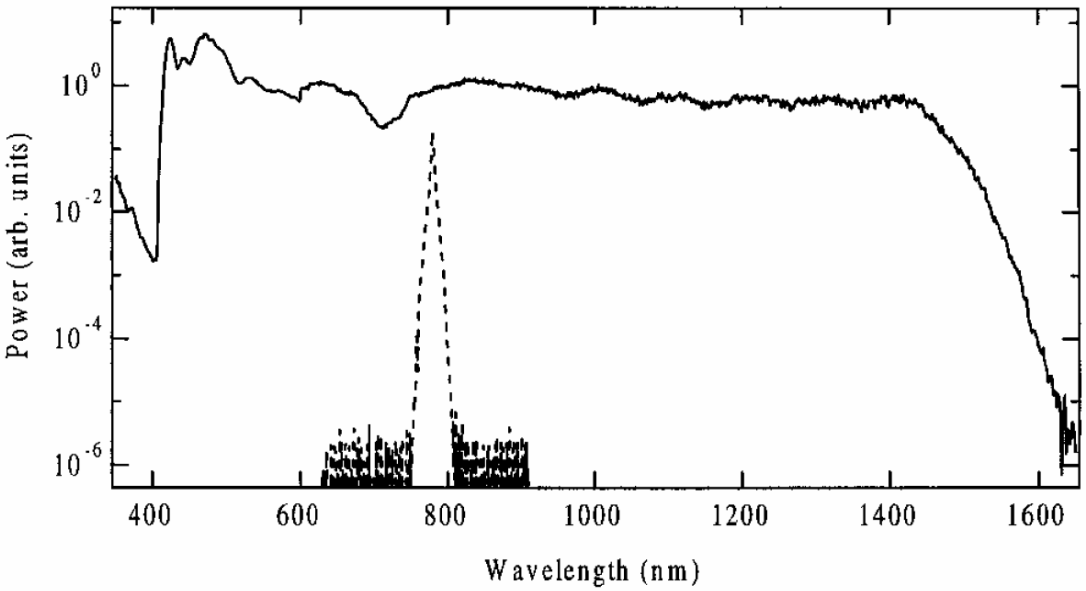

Figure 2.8: An ultra broadband supercontinuum generated in a 75-cm section of microstructure fiber. The dashed curve shows the spectrum of the initial 100-fs pulse. Refer to Ranka et al. [6].

specially designed "microstructured fiber" using Ti:Sapphire laser 100 fs pulses with 790 nm central wavelength and only 0.8 nJ energy. The microstructured fiber consists of a silica core of 1.7 μm surrounded by an array of 1.3 μm diameter air holes in a hexagonal close-packed arrangement, see Fig. 2.6 (a), sustaining single-mode laser pulse propagation for wavelengths range from 500 nm to 1600 nm. It is quite surprising that the mode is well confined within the first air hole ring next to the core; the outer rings of air holes do not affect the fiber waveguide properties at all. With this air hole and pitch configuration, zero group velocity dispersion wavelength is pushed down to 767 nm,

making the Ti:Sapphire input pulse central wavelength in the anomalous fiber dispersion region. Nonlinear optical effects, include pulse compression, soliton propagation and efficient four-wave mixing are observed at 800 nm. All these nonlinear effects have been severely limited at this wavelength for conventional fibers.

The intensive interest in the supercontinuum generations is well justified. First, performing the experiment of supercontinuum generation is not hard at all, considering the popularization of the Ti:Sapphire laser all over the world and the advantage of low power requirement. Numerous papers have been published on this subject, taking up a large portion of microstructured fiber literature. Many of the papers are about the applications of supercontinuum generation, which will be presented in details in the next section. The more significant reason for the interest in the supercontinuum generations lies in its complex process, that is, how the ultra broadband supercontinuum is generated?

From a general point of view, there are two contributions which lead to ultra broadband supercontinuum generation. The first one comes from geometry. A microstructured fiber has an extremely small core area, nearly two orders of magnitude smaller when compared to that of conventional single-mode fiber. The tighter confinement of the mode propagation leads to an increased power density and enhanced effective nonlinearities. The second contribution is the tailorable dispersion characteristics of the microstructured fibers, resulting from both the ability to precisely engineer the air hole and pitch size as well as the high refractive index difference between the core and cladding. As a result, the zero GVD dispersion can be pushed down to visible wavelength range and the input Ti:Sapphire laser pulse that experiences a low fiber dispersion maintains a high peak power while propagating along. The enhanced

fiber nonlinearities combining with the intensive peak power of the laser pulse trigger many nonlinear processes, generating the ultra broadband supercontinuum.

In principle, the supercontinuum generation process in microstructured fibers is not different from that in conventional fibers. Well established theories (see, for example Broderick et al [49] and references therein) explaining many nonlinear processes in optical fibers has been developed over years. However, supercontinuum generation is a nonlinear process in the extreme. It is evident that supercontinuum generation is not resulting from or dominant by one individual nonlinear process; on the contrary, it results from the complex interplay between various nonlinear optical processes and dispersion characteristics of microstructured fibers. The complexity also lies in the fact that the significant pulse spectral broadening process usually happens within the first several millimeters of the microstructured fiber at sufficiently high power due to the enhanced nonlinearities and low dispersion. It is crucial to understand the supercontinuum generation dynamics; in particular, the roles of different nonlinear optical processes play in a certain pulse propagation stages and their contributions to the final supercontinuum characteristics. The interpretations of the supercontinuum generation dynamics from the experimental data are sometimes misleading, as it is usually hard to separately study the individual nonlinear effect in the experiment when various nonlinear effects are interacting together in a tangled state. The extended NLSE model using the split-step Fourier transform method has proven to be a well-suited numerical technique that can truly simulate the pulse nonlinear propagation processes in the microstructured fibers. Besides the ability of investigating individual nonlinear effect and its contribution to the supercontinuum generation, this simulation model has also predicted some new

supercontinuum properties that have been experimentally verified. However, the complexity and ultra broadband properties of the supercontinuum generation require a large number of data points and an extremely small propagation step when implement the extended NLSE simulation model, necessitating the use of high speed computers only available to general researchers in the last five to ten years.

Many papers have been published from the extensive research on the formation and evolution of the supercontinuum. A consentaneous conclusion has been formed based on the rigorous simulation and experimental results [10, 11]. It is believed that the development and evolvement of the supercontinuum is related to the formation and fission of higher order solitons in the microstructured fibers. As we mentioned in the section 2.2, in the anomalous dispersion region, higher order solitons are generated in the microstructured fiber due to the interplay between the SPM and GVD, where the soliton order is determined by equation 2.14. Without any perturbation, these higher order solitons will propagate in a periodic evolution pattern and supercontinuum generation would never occur. However, a small perturbation will affect a higher order (N>1) soliton's relative group velocities and, subsequently, trigger the soliton fission: a higher order soliton with soliton order N breaks up to N fundamental solitons. These small perturbations include higher order dispersion, self-steepening nonlinear effect and soliton self-frequency shift. As a result of soliton fission and soliton self-frequency shift, the fundamental solitons continuously shift toward the longer wavelength of the broadened spectrum, causing a considerable spectral expansion on the red side. The blue side the supercontinuum is developed due to the blueshifted nonsolitonic radiation (NSR) [3, 10, 53] or phase-matched radiation; that is, the blue dispersive wave component satisfying

the resonance condition gets amplified by the energy transferred from the phase-matching soliton under the influence of higher order dispersion [54]. Assuming the soliton frequency ω_s and the nonsolitonic radiation component ω_r, the phase matching condition can be written as [53],

$$\Delta\kappa = \beta(\omega_r) - \beta(\omega_s) - (\omega_r - \omega_s)/v_g - \gamma P_0 = 0\,, \tag{2.27}$$

where β is propagation constant, v_g is the group velocity, γ is the nonlinear parameter and P_0 is the input peak power. Consequently, an ultra broadband supercontinuum is generated as the fundamental solitons continuously shift to the red side and the blue phase-matching components are developed and amplified.

It is worth pointing out that supercontinuum is the outcome from interactions of the most complex nonlinear optical processes with fiber dispersion. Supercontinuum generation usually occurs within the first several millimeters of the propagation length, followed by the increasingly fine interference features from the interplay between the individual soliton and the related dispersive wave as supercontinuum continues to evolve along the microstructured fibers. It turns out to be true that any small input pulse power fluctuation can substantially change the features of this fine structure, as verified by both the simulation results and experimental evidences [9, 13]. The fine structure which tends to vary from shot to shot can be a huge problem for many applications. For example, stable spectral phases are required for supercontinuum pulse compression application. Researchers have put a lot of efforts in finding out the stability range for various applications. Consequently, different stability fiber lengths range from ~1cm to tens of centimeters corresponding to different input power levels have been found [15, 55]. Meanwhile, changing the microstructured fiber dispersion properties can evidently

minimize the instability of the supercontinuum. Detailed simulation results following this idea will be discussed in chapter 6.

When the central wavelength of the input pulse is in the normal dispersion region of the microstructured fiber, supercontinuum can also be generated. Before the spectral broadened pulse reaching the anomalous dispersion region, due to the high peak power of the input pulse, SPM nonlinear effect is mainly responsible for the pulse spectral broadening at this stage. Meanwhile, the peak intensity of the pulse is still intense because of the low fiber dispersion. After the spectrum broadening into the anomalous dispersion region, higher order solitons are generated and the mechanisms similar to what have been described above lead to the supercontinuum generation.

2.3.3 Applications of PCFs and Supercontinuum Generation

The diversity of new or improved performance, beyond what conventional fiber can offer, means that PCF is finding an increasing number of applications in ever-widening areas of science and technology [31]. Photonic crystal fibers have important applications in the optical telecommunications. The enhanced waveguide nonlinearities in the microstructured fibers potentially make the telecommunication optical functions to be achieved within a much shorter fiber length comparing to that of conventional fibers [56]. Microstructured fibers also find applications in fiber lasers and amplifiers. Large mode area single-mode microstructured fiber allows one to obtain a high power output with relatively low power density. This way nonlinear phenomena and fiber damage due to overheating can be avoided, making large core microstructured fibers predestinated for high power operations [57]. Photonic bandgap fibers can be used in the sensor technology [58]. They can also be used for atom and particle guidance, which has a potential application in biology, chemistry and atomic physics. Particle levitation in hollow-core

fiber over 150 mm distance with 80 mW laser power has been reported [59]. Furthermore, the core of the photonic bandgap fibers can be filled with a variety of gases to study gas-based nonlinear optics. In particular, stimulated Raman scattering in hydrogen-filled photonic bandgap fiber has been extensively studied [60]. On the other hand, photonic bandgap fibers filled with argon gas can be potentially used for high harmonic generation, a phenomenon occurs when the gas election experiencing the recombination process after being ionized by the ultrashort high-energy pulses [61].

Supercontinuum generation, the most fascinating outcome of the PCFs, has a far more important application scopes. First, it has become a nature candidate for telecommunication applications. To construct flexible and robust photonic networks, it is essential to control, manage and fully utilize the vast optical frequency resources available. Indeed, supercontinuum generation offers the possibility of generating over 1000 dense-wavelength-division-multiplexing (DWDM) channels using only one single light source [21] while maintaining its coherent characteristics. Supercontinuum generation also has application in medical imaging [62-64]. For optical coherence tomography (OCT), longitudinal resolution in a biological tissue is inversely proportional to the bandwidth of the light source. Supercontinuum generation with high spatial and spectral coherence has increased the OCT longitudinal resolution to a micron level (~1.3 μm , see Wang et al. [64]). The most important application of supercontinuum generation is in the field of optical metrology [65-67]. It makes the measurement of absolute optical frequency possible by establishing a direct link between the repetition rate of a mode-locked laser and optical frequencies. Using a carrier-envelope phase-locked laser, an optical clock with accuracy 1–2 orders of magnitude better than the

currently used cesium atom clocks is demonstrated [68-70]. This work led to 2005 Nobel prize for two of the pioneers of the field, John Hall of JILA at the University of Colorado and Ted Hänsch of the Max Planck Institute for Quantum Optics [8].

CHAPTER 3
OVERVIEW OF EXPERIMENTAL TECHNIQUES

To understand how ultrashort laser pulses interact with PCFs, it is important to understand the methods of generating, characterizing, and temporally tailoring ultrashort pulses. In this chapter, we will lay out the experimental tools used in our research. A brief introduction of ultrashort laser pulse and terminology will be given in section 3.1 and 3.2. We discuss the operating principles and performance of our home-build Ti:Sapphire laser oscillator and a commercial Coherent Mira 900 laser oscillator in section 3.3. A description and comparison of different ultrafast laser pulse characterization tools will be given in section 3.4. Finally, in section 3.5, we present the Fourier domain pulse shaping using the liquid crystal spatial light modulators.

3.1 Ultrashort Laser Pulses

Lasers are the basic building block of the technologies for the generation of short light pulses. Only four decades after the laser had been invented, the duration of the shortest produced pulse has been reduced nine orders of magnitude, going from the nanosecond (10^{-9} s) regime to the attosecond (10^{-18} s) regime [72]. One reason for generating ultrashort pulses is to challenge the physics limit: what is the shortest pulse mankind can generate? Another question may arise here: what kind of measurements can we make with these ultrashort laser pulses?

One important application domain of ultrashort laser pulses is the behavior analysis (return to equilibrium) of a sample perturbed by the laser pulses [73-75]. If some processes in the sample are very fast compared to the duration of the perturbation, these

processes will be hidden during the perturbation so that only those processes which are slower than the pulse duration will be observed. Therefore, it will be easier to understand the faster processes if one can use a shorter perturbation. The unique property of ultrashort laser pulses makes them ideally suited for not only the initial perturbation of sample but also subsequent probing of the sample.

On the other hand, ultrafast lasers can also be used to produce laser pulses with extremely high peak powers and power densities, which have applications such as multiphoton imaging [76, 77], generation of electromagnetic radiation at unusual wavelengths [78-80] and laser machining and ablation [81]. Meanwhile, the large peak intensities associated with ultrashort laser pulses make them well suited to various nonlinear wave-mixing processes, allowing the generation of new frequency components. Such processes include second-harmonic generation, sum-frequency generation, parametric oscillation and amplification, and continuum generation.

3.2 Laser Pulse Terminology

To better understand ultrafast laser system, ultrashort laser pulse characterization and shaping, we begin with some terminology [82].

3.2.1 Laser Pulse Time Bandwidth Product (TBP)

A continuous wave laser generates continuous wave (CW) that is an electromagnetic wave of constant amplitude and frequency; and in mathematical analysis, of infinite duration. The time representation of the field (real part) is an unlimited cosine function.

$$E(t) = E_0 e^{i\omega_0 t} \tag{3.1}$$

On the other hand, constructing a light pulse implies multiplying (3.1) by a bell-shaped function, e.g., a Gaussian function. Mode-locked lasers generate this kind of pulses. In general, a pulse can be represented as

$$E(t) = A(t)e^{i\omega_0 t}e^{i\phi(t)}, \tag{3.2}$$

where $A(t)$ is the bell shaped function and $\phi(t)$ is the pulse phase. The physical field is $\mathrm{Re}[E(t)]$. The general time and frequency Fourier transforms are

$$\begin{aligned} E(\omega) &= A(\omega)e^{i\phi(\omega)} = \int_{-\infty}^{+\infty} E(t)e^{i\omega t}dt \\ E(t) &= \frac{1}{2\pi}\int_{-\infty}^{+\infty} E(\omega)e^{-i\omega t}dt \end{aligned}, \tag{3.3}$$

where $E(\omega)$ is the pulse representation in the frequency domain.

In particular, a Gaussian pulse can be written as

$$E(t) = E_0 e^{-(t/\tau)^2}e^{i\omega_0 t} \tag{3.4}$$

A limited duration caused by the Gaussian envelope of the light pulse indicates a limited frequency bandwidth, which can be clearly seen after the Fourier transformation of the original temporal pulse (Eq. 3.4).

$$E(\omega) = \int_{-\infty}^{+\infty} E(t)e^{i\omega t}dt = \sqrt{\pi}E_0\tau \cdot e^{-\left[\frac{(\omega-\omega_0)\tau}{2}\right]^2} \tag{3.5}$$

The pulse duration and spectral width are defined as the full width half maximum (FWHM) of the pulse intensity ($I(t) \equiv |E(t)|^2$ and $I(\omega) \equiv |E(\omega)|^2$) in time domain and frequency domain, respectively. In the case of a Gaussian pulse (Eq. 3.4 and 3.5), the pulse duration and spectral width are

$$\begin{aligned} \Delta t &= \tau\sqrt{2\ln 2} \\ \Delta\omega &= \frac{2}{\tau}\sqrt{2\ln 2} \end{aligned}. \tag{3.6}$$

Note that time bandwidth product (TBP, $K = \Delta t \cdot \Delta f$) is a dimensionless number which depends on the shapes of the pulses, e.g., the shape of a Gaussian pulse is represented as function $e^{-(t/\tau)^2}$. Table 3.1 gives values of K for Gaussian shape and hyperbolic secant shape which are the most commonly used pulse envelopes.

Table 3.1: Time bandwidth products (K) for Gaussian and hyperbolic secant pulse shapes.

Shape	$E(t)$	$K = \Delta t \cdot \Delta f$
Gaussian function	$e^{-(t/\tau)^2}$	0.441
Hyperbolic secant function	$\frac{1}{\cosh(t/\tau)}$	0.315

3.2.2 Laser Pulse Phase and Chirp

The TBP value in table 3.1 can only be reached when the instantaneous angular frequency is constant and equals the central angular frequency ω_0, which can be seen from Eq. 3.4 and $\omega(t) = \omega_0$. The pulse is called a Fourier transform-limited pulse.

Now let's consider a more general case, that is, the instantaneous angular frequency is a function of time. Suppose the phase of the pulse obeys a quadratic law in time,

$$E(t) = A(t)e^{i\omega_0 t}e^{i\phi(t)} = A(t)e^{i\omega_0 t}e^{i\alpha t^2}, \tag{3.7}$$

then the instantaneous angular frequency varies linearly with time

$$\omega(t) = \omega_0 + \partial\phi/\partial t = \omega_0 + 2\alpha t . \tag{3.8}$$

Depending on the sign of α , the pulse is positive or negative "chirped", i.e., linear chirp. It is very clear from Fig. 3.1, i.e., chirped Gaussian pulses, that the instantaneous frequency is more red in the leading part of the pulse and more blue in the trailing part when a positive chirped pulse is presented.

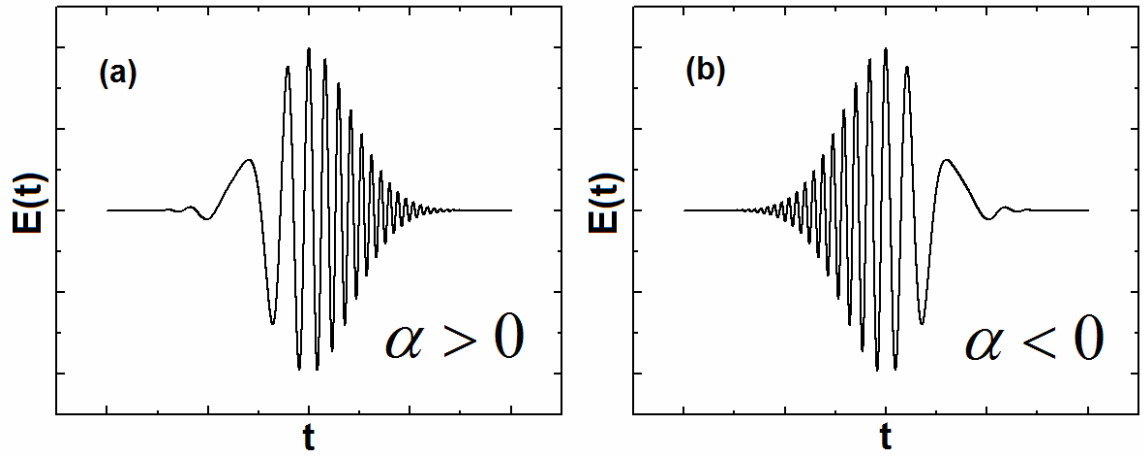

Figure 3.1: Illustration of Gaussian pulses with linear chirps. (a) A positive linear chirp. (b) A negative linear chirp.

The pulse duration and spectral width in the linearly chirped Gaussian pulse are

$$\begin{aligned} \Delta t &= \tau\sqrt{2\ln 2}\,, \\ \Delta\omega &= 2\sqrt{2\ln 2}\sqrt{\frac{1}{\tau^2}\left[1+\alpha\tau^2\right]}. \end{aligned} \tag{3.9}$$

The TBP will always be greater than the value listed in table 2.1. This discussion is also true if we start from the frequency domain with a chirped pulse. So the conclusion is that a Fourier-transform-limited pulse (the shortest pulse) is generated when the pulse with a fixed spectrum has no spectral phase.

Unfortunately, when ultrashort pulses propagate in an optical system, many optical components (lenses, gratings, crystals) are dispersive and can generate some kind of chirp (linear and/or higher order chirp) that causes pulse temporal broadening. It is common practice to expand the spectral phase in a Taylor Series as

$$\phi(\omega) = \phi^{(0)} + \phi^{(1)}(\omega-\omega_0) + \frac{\phi^{(2)}}{2}(\omega-\omega_0)^2 + \frac{\phi^{(3)}}{6}(\omega-\omega_0)^3 + \cdots, \tag{3.10}$$

where

$$\phi^{(i)} = \left(\frac{\partial^{(i)} \phi(\omega)}{\partial \omega^{(i)}} \right)_{\omega=\omega_0} . \tag{3.11}$$

The linear and quadratic chirp are represented as $\phi^{(2)}$ and $\phi^{(3)}$, respectively. A pulse compressor [83] (a pair of parallel diffraction gratings and a retro-reflector) can compensate most of the linear chirp, but can do nothing about the higher order chirps. To obtain the shortest pulse, the overall spectral phase (chirp) has to be measured and compensated. This will be one of the applications of pulse characterization and pulse shaping which will be discussed later in this chapter.

3.3 Femtosecond Lasers (Ti:Sapphire Lasers)

Lasers are the basic building blocks to generate short pulses. Ti:Sapphire femtosecond laser has been studied extensively because its high performance. In order to understand how laser pulse can be temporally tailored and interact with the fibers, it is important to understand how femtosecond laser pulses are generated in the Ti:Sapphire lasers. In this section we will describe the properties of the Ti:Sapphire crystal, followed by the mode-locking discussion. We will also lay out the schematics and performance parameters of the Ti:Sapphire lasers used in our experiments.

3.3.1 Ti:Sapphire Crystal

In the past decade, the most spectacular advances in laser physics and, particularly, in the field of ultrashort light pulse generation [84, 85] have been based on the development of titanium-doped aluminum oxide (Ti:Al_2O_3, Ti:Sapphire) laser. Ti:Sapphire laser has been investigated extensively and today it is the most widely used tunable solid-state laser. Ti:Sapphire possesses a favorable combination of properties which are up to now the best broadband laser materials. First, the active medium is solid-state, that means long operational time and laser compactness. Second, Sapphire has high

thermal conductivity, exceptional chemical inertness and mechanical resistance. Third, Ti:Sapphire crystal has the largest gain bandwidth and is therefore capable of producing the shortest pulse; it also provides the widest wavelength tunability [Fig. 3.2].

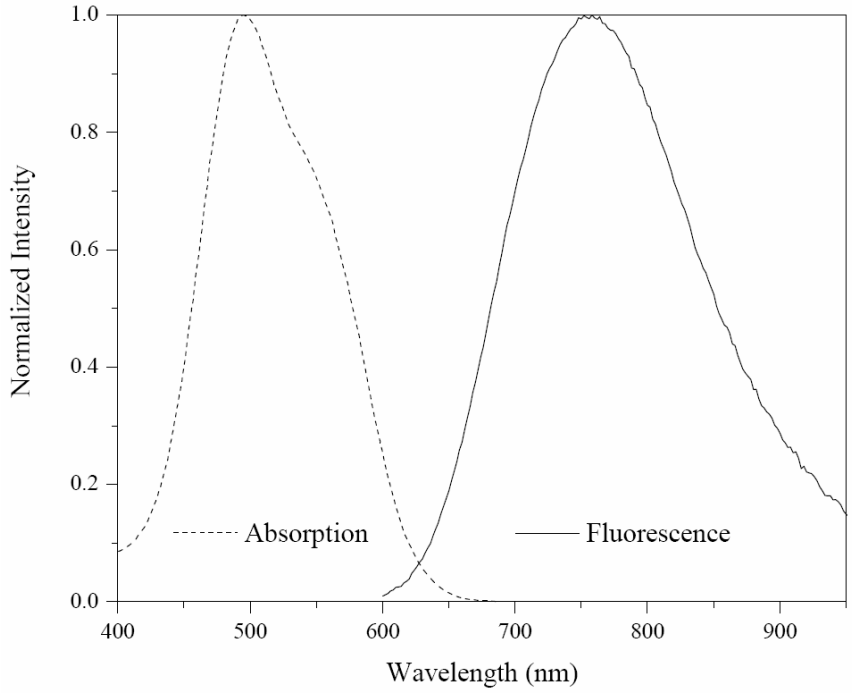

Figure 3.2: Normalized absorption and emission spectra of Ti:Sapphire for π polarized light. Refer to Rulliere [82].

From the fluorescence curve, the estimated the FWHM of the theoretical broadest spectrum is 190 nm, which corresponds to a 4.5 fs pulse if a Gaussian transform-limited pulse is assumed. In fact, custom build Ti:Sapphire laser that can generate 4.8 fs ultrashort pulse has been reported [86], merely two cycles of the optical field considering 800 nm center wavelength.

3.3.2 Kerr Lens Mode-Locking

A large number of mode-locking techniques have been developed to generate short pulse with Ti:Sapphire as a gain medium: active mode-locking, passive mode-locking and self-mode-locking. Self-mode-locking (or Kerr lens mode-locking) has proven to be

the best way to achieve the mode-locking. Self-locking of the modes utilizes the nonlinear properties of the amplifying medium to favor strong intensity maxima at the expense of weak ones.

The nonlinear effect called self-focusing is due to the fact that the refractive index of Ti:Sapphire is a function of input pulse intensity: $n = n_0 + n_2 I(r,t)$. Because of the non-uniform power density distribution in the cavity Gaussian beam $I(r,t)$, the refractive index changes across the beam profile and the phase delay experienced by the beam is greater in the center of the beam than at the edge for $n_2 > 0$ [Fig. 3.3]. Therefore,

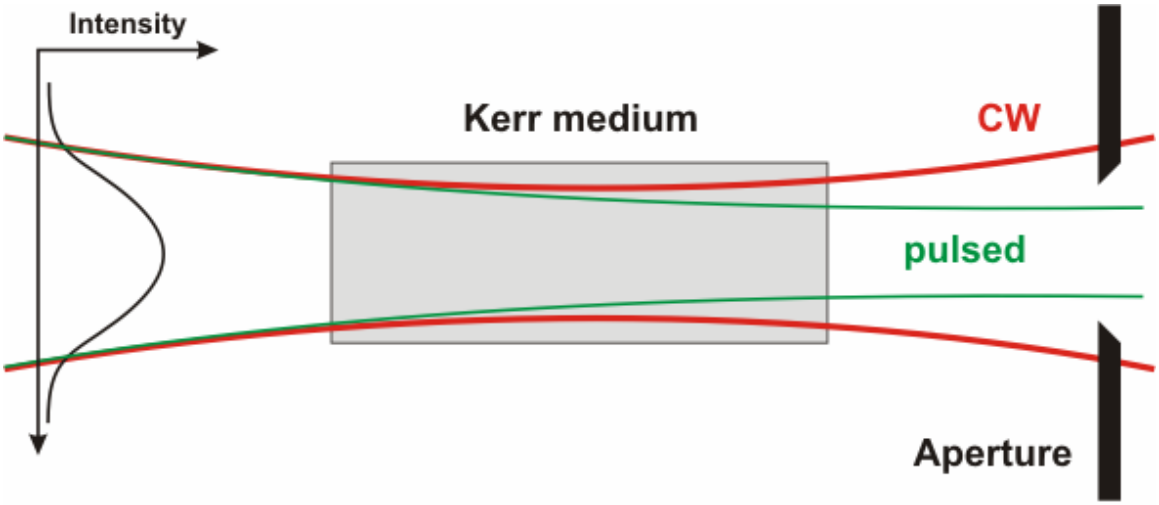

Figure 3.3: Kerr lens modelocking principle: self-focusing effect by the optical Kerr effect. An example of hard aperture refers to Wikipedia [87].

the Ti:Sapphire crystal works like a nonlinear lens (Kerr lens) for high intensity light, with the focusing effect increasing with optical intensity. In the laser cavity, short noise bursts of light (pulses), which have higher peak intensities, are focused more tightly and are transmitted through the aperture, whilst lower intensities experience greater losses. By aligning the cavity in a way such that the resonator is lossier for CW beam than for pulses, the pulsed regime is *favored* and the laser will turn to mode-locked regime. The

favoring of pulsed regime over CW regime can be achieved by the cavity design, but is often supported by a hard aperture (shown in Fig. 3.3), that can simply cut off part of the CW beam at the focal region of the pulsed beam.

3.3.3 Cavities of Ti:Sapphire Lasers

Depending on the experiment requirement and consideration, we use two different types of Ti:Sapphire oscillators in our experiments, all of which will be discussed in details in the rest of this section.

3.3.3.1 Home-build Ti:Sapphire oscillator

For most of our experiments, we use a home-built Ti:Sapphire oscillator. The design of the oscillator is shown schematically in Figure 3.4. The intracavity is defined by prism pairs and four mirrors, M1, M2, M3 and the output coupler M4. The Ti:Sapphire crystal is located at the common focal plane of two 10-cm spherical mirrors M2 and M3. The laser system is pumped by focusing a multi-line Argon-Ion CW laser (Coherent Innova 310). The output coupler M4 is an 85% wedged mirror. The intracavity prism pairs are the key components for self-mode-locking (Kerr lens mode-locking). Hard apertures are placed in front of the cavity mirror M1 and output coupler M4. In this oscillator, mode-locking is initiated by instantaneously moving the first intracavity prism P1 and M3. The dispersion caused by intracavity prism pairs and other optical component in the cavity (crystal and OC) is partially compensated with the external prism pairs, which is designated in the Figure 3.4 as the phase compensator. With 4.9 W pumping power, our home-build Ti:Sapphire oscillator generates 300-400 mW average pulse power. The repetition rate is 91 MHz and energy per pulse is around 3 nJ.

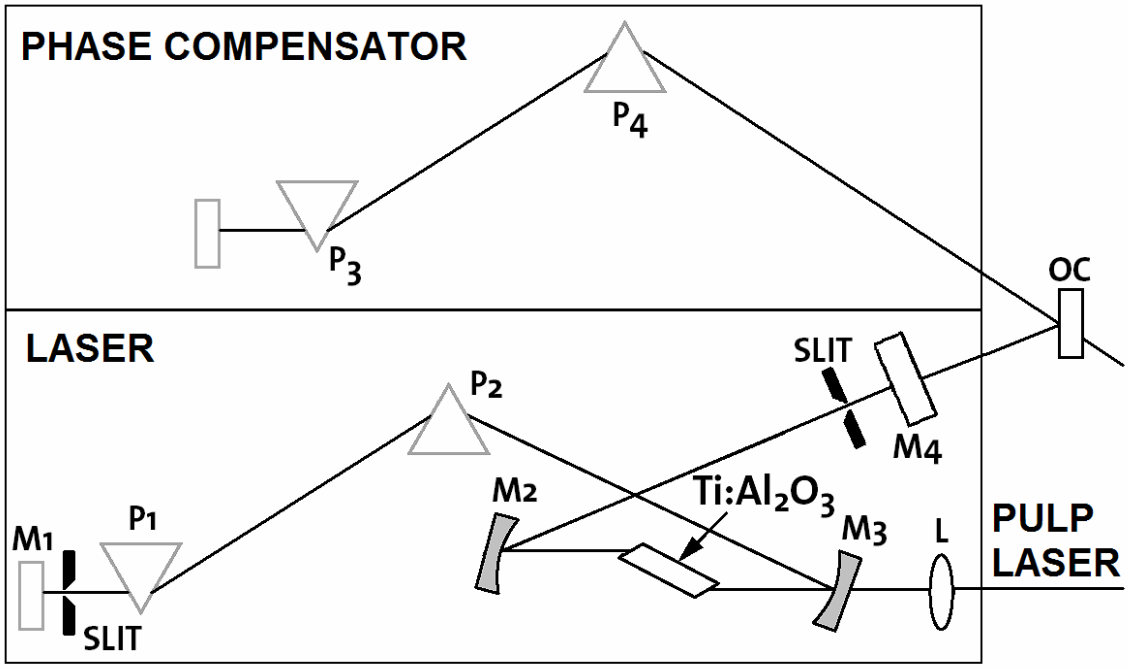

Figure 3.4: Schematic diagram of the Ti:Sapphire Laser and the external phase compensator. P: prism. OC: output coupler

The output spectrum is shown in Fig (b). It has a bandwidth of 65 nm and central wavelength of 805 nm. Fig (a) is the second order intensity autocorrelation, using a 100 μm KDP crystal. Assuming a Gaussian pulse shape, the measured FWHM of the laser pulse is ~18 fs.

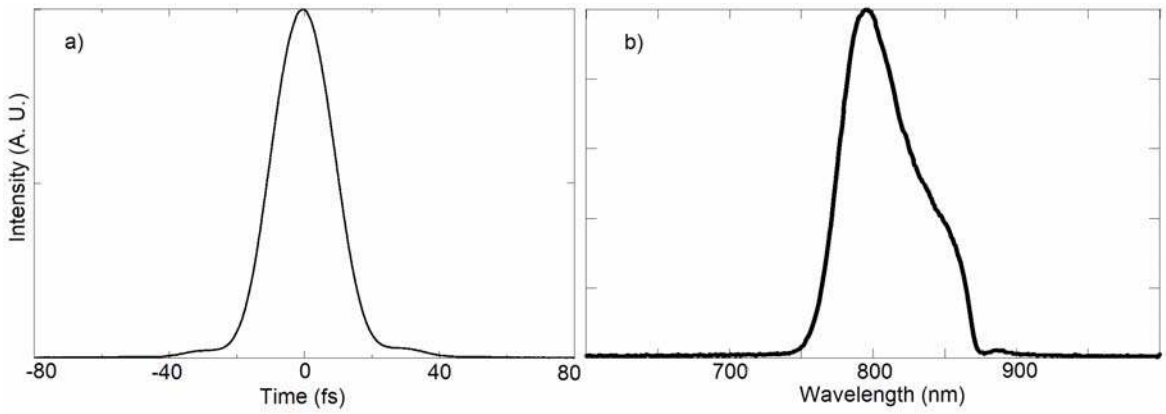

Figure 3.5: Second order intensity autocorrelation and spectrum of Ti:Sapphire laser pulse. (a) Temporal autocorrelation of the pulse. (b) Measured spectrum of the pulse.

3.3.3.2 Coherent Mira 900 system

For the experiment described in section 4.3, we use the commercial Coherent Mira 900 (Fig. 3.6) pumped by Ion CW Coherent Innova 400 laser. The Mira has a tunable wavelength range from 700 nm to 900 nm. From the schematics we can see there are several extra mirrors comparing with our oscillator. The only purpose is for the commercial compact design. Note that M8 and M9 are for alignment only and they are not in the oscillator cavity. However, Mira 900 does consist of a birefringent filter (BRF) which makes Mira 900 a central wavelength tunable laser. Such filters take advantage of the phase shifts between orthogonal polarizations to obtain narrow band outputs. Furthermore, the commercial design of a butterfly starter (not shown in the figure) between M3 and M4 makes mode-locking a breeze. The wavelength used in our experiment is 763 nm. With 8 W pumping power, the average output pulse power is about 450 mW. The repetition rate is 76 MHz and energy per pulse is around 6 nJ.

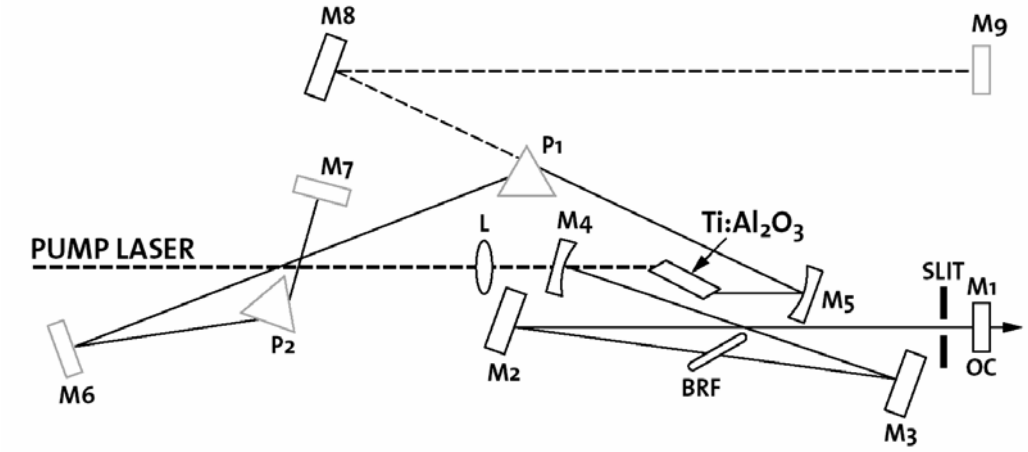

Figure 3.6: Schematic diagram of a Coherent Mira 900 Ti:Sapphire laser. Refer to Coherent Mira 900 [88].

The spectral bandwidth of Mira 900 output pulse is very narrow comparing to our home-build Ti:Sapphire oscillator due to the BRF, in this case, 4.2 nm [Fig. 3.7 (b)]. The

temporal pulse duration is measured by FROG (see next section for details). The calculated pulse duration for transform-limited Gaussian pulse with measured spectral intensity is 215 fs. The measured pulse duration is 225 fs [Fig. 3.7 (a)].

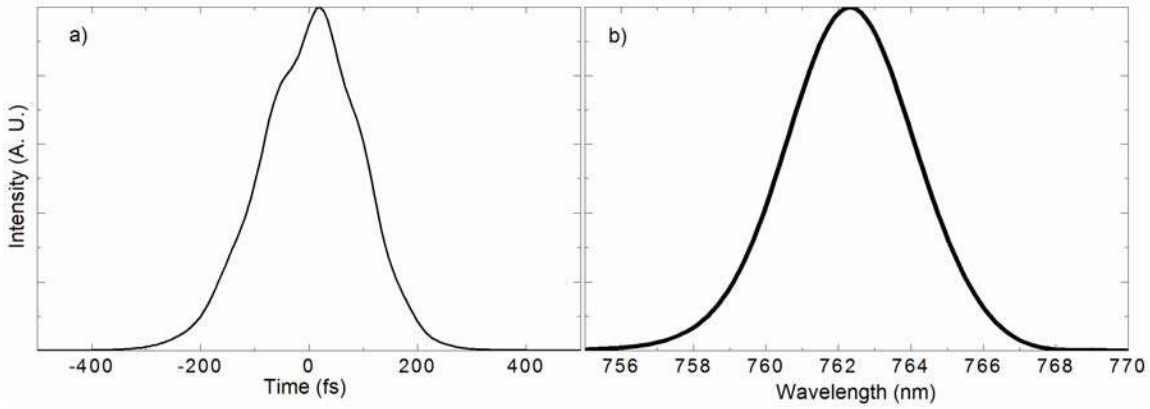

Figure 3.7: FROG measurement of a Coherent Mira 900 Ti:Sapphire laser pulse. a) Temporal intensity. b) Spectral intensity.

3.4 FROG and SPIDER

Ultrashort laser pulses are the shortest events mankind ever generated. Before ultrashort laser pulses are used in experiments, pulse diagnostics are necessary. Since the femtosecond time scale is beyond the range of the fastest electronics, the pulse measurement techniques have to be redesigned in order to fully characterize the amplitude and the phase of the electric field. Most techniques are based on the idea "measuring pulse using the pulse itself!" Section 3.4.1 will briefly describe the standard techniques that determine the temporal profile of the pulse, such as auto-correlation and cross-correlation. Other techniques, which are more sophisticated giving both information of frequency and time, such as FROG and SPIDER, will be presented in the section 3.4.2 and 3.4.3.

3.4.1 Auto-Correlation and Cross-Correlation

Maybe the most widely used technique for measuring femtosecond laser pulses is the second-order auto-correlation, which was first demonstrated in 1966 by Maier and co-workers [89]. This method takes advantage of the second harmonic generation in nonlinear crystals. In Figure 3.8 the basic principle of SHG auto-correlation is displayed. This is typically used to measure the time duration of femtosecond pulses.

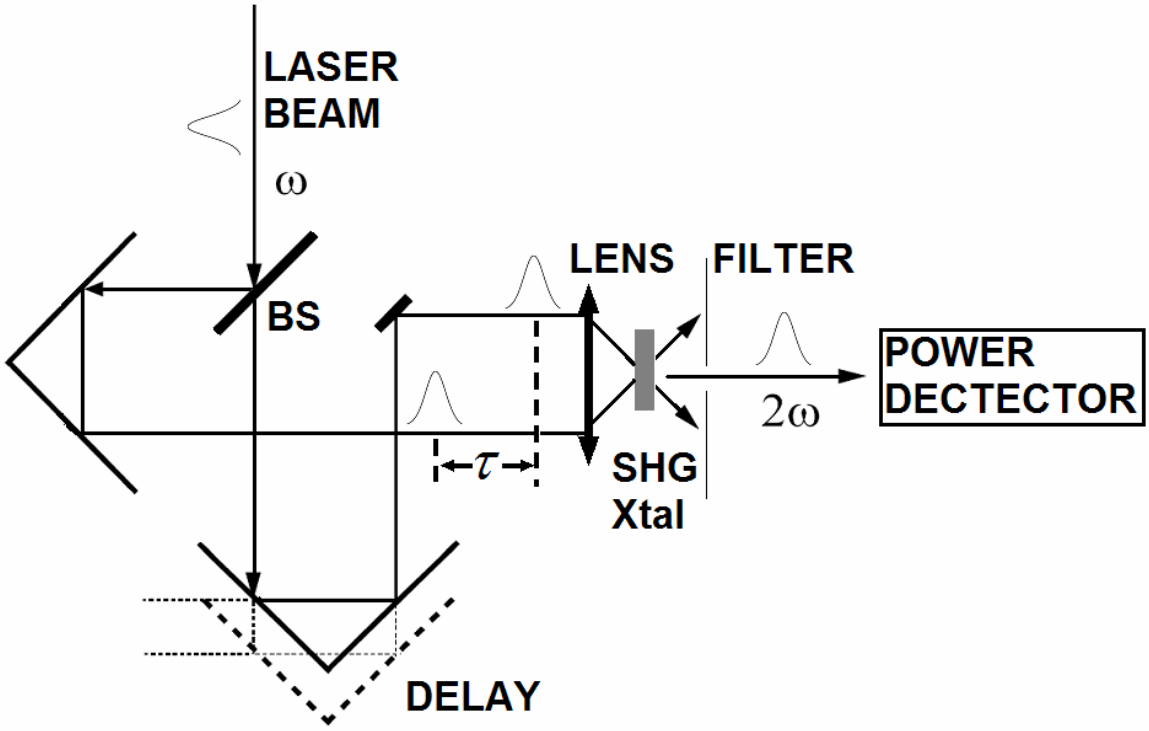

Figure 3.8: Schematic diagram of a SHG auto-correlator. BS: beam splitter. SHG Xtal: second harmonic generation crystal.

The incident laser pulse is split in two pulses by a 50/50 beam-splitter. Similar to a Michelson interferometer, the two pulses are reflected in each arm and subsequently focused onto a frequency-doubling crystal. The resulting second-harmonic-generation (SHG) auto-correlation trace is detected by a photo-multiplier as a function of the time delay τ between the two pulses. The SHG crystals can be type I phase-matching or type II, and the two pulses can recombine collinearly or non-collinearly in the frequency

doubling medium. Figure 3.8 is an example of non-collinear recombination of the two pulses. The SHGs of each individual pulses are filtered by a hard aperture and a BG-39 filter may also be used to eliminate the original laser pulse signal that pass through the SHG crystal.

If the two fields are of intensity $I(t)$ and $I(t-\Delta t)$, the auto-correlation of the two pulses is

$$I_{ac}(\Delta t) = \int_{-\infty}^{\infty} I(t)I(t-\Delta t)dt \tag{3.12}$$

As can be seen from the equation, the auto-correlation is always a symmetric function in time. Therefore, auto-correlation gives very little information about the shape of the pulse. The most widely used procedure to determine the pulse duration is to "pre-assume" a pulse shape (usually hyperbolic secant or a Gaussian shape, for chirp-free and linear chirped pulses) and to calculate the pulse duration from the known ratio between the FWHM of the auto-correlation and of the pulse. Thus the auto-correlation function depends on the assumed shape of the pulse. Table 3.2 lists the relevant parameters for various shapes.

Table 3.2: Relations between pulse duration and auto-correlation function duration for Gaussian and Hyperbolic secant function.

Shape	$I_{ac}(t)$	$TBP:K$	Pulse duration $\Delta t/\tau$
Gaussian function	$e^{-(\frac{-4\ln 2t^2}{\Delta t^2})}$	0.441	$\sqrt{2}$
Hyperbolic secant function	$Sech^2(\frac{1.76t}{\Delta t})$	0.315	1.5

In cross-correlation, the ultrashort pulse is not correlated with itself. The cross-correlation implies the use of a reference pulse of a known shape $I_r(t)$ in order to

determine the temporal profile of an unknown laser pulse $I_s(t)$. The intensity cross-correlation to be measured is

$$I_{cc}(\Delta t) = \int_{-\infty}^{\infty} I_s(t) I_r(t - \Delta t) dt \tag{3.13}$$

The convolution with the intensity of the reference pulse leads to a smooth cross-correlation shape.

The fundamental problem of auto-correlation and cross-correlation is that it does not uniquely determine the pulse characteristics. It cannot even accurately determine the pulse duration because a priori information about the pulse shape is required, which is sometimes impossible to obtain. Furthermore, a systematic analysis given in Chung et al. [90] shows that very similar autocorrelation traces and power spectra can be produced by pulses with drastic different shapes and durations. In fact, to fully characterize a pulse, including the intensity and phase in time domain or frequency domain, one needs a total number of 2N points. The correlation function only gives N points, meaning the pulse characterization for this technique is indeed quite under-determined.

Of course, to understand the pulse itself, which includes what time a color occurs in a pulse, or equivalently, pulse spectral phase, full pulse intensity and phase characterization techniques are required. The development of several such kinds of technique occurs in the early 1990s. Among which, SHG frequency-resolved optical gating (FROG) and spectral phase interferometry for direct electric-field reconstruction (SPIDER) are the most well-known techniques. Frequency resolved optical gating uses two dimensional representation of the one dimensional electric field, while SPIDER uses one dimensional spectral interferometry. All of which will be discussed in details in this section.

3.4.2 Frequency Resolved Optical Gating (FROG)

Frequency resolved optical gating (FROG) was first developed in 1993 [91, 92]. Frequency resolved optical gating is a method that can acquire both intensity and phase of a pulse without making prior assumptions about pulse shape. Frequency resolved optical gating is based on spectrally resolving autocorrelation function; therefore generating the spectrogram of the pulse to be measured (refer to Fig. 3.10 (a) as an example). A spectrogram, $S(\omega,\tau)$, is a two-dimensional representation of the pulse as a function of time delay and frequency (or wavelength),

$$S(\omega,\tau)=\left|\int_{-\infty}^{\infty}E_{sig}(t,\tau)e^{-i\omega t}dt\right|^2, \tag{3.14}$$

where $E_{sig}(t,\tau)$ is simply the autocorrelation signal and has several forms depending on different version of FROG techniques, e.g., self-diffraction (SD) FROG, polarization gating (PG) FROG, SHG FROG and third harmonic generation (THG) FROG. Among all these versions, only SHG FROG utilizes the second order nonlinearities while all the other versions rely on the third order nonlinearities to perform the autocorrelation. This makes SHG FROG one of the most widely used FROG techniques. For the SHG FROG, the $E_{sig}(t,\tau)$ is simply a second order autocorrelation function,

$$E_{SHG,sig}(t,\tau)=E(t)E(t-\tau). \tag{3.15}$$

Experimentally, a SHG FROG apparatus is an auto-correlator followed by a spectrometer. Therefore, instead of just measuring the intensity of the nonlinear optical signal generated by the two variably delayed pulses, the nonlinear optical signal $S(\omega,\tau)$ is spectrally resolved into a delay dependent spectrum, i.e., spectrogram. The resulting data is a two dimensional time-frequency representation of the pulse, that is, a 2D function of time

delay and optical frequency. The spectrogram obtained is referred to as the measured "FROG trace", as show in Fig 3.10 (a). In some cases, the shape of the FROG trace can be interpreted to give an overview of the shape of the pulse.

In order to "retrieve" the original pulse intensity and phase, a sophisticated iterative inversion algorithm needs to be applied to the 2D FROG trace. The two-dimensional phase retrieval algorithm has been well established in the field of image science. The electric field and phase of the pulse that created the FROG trace can indeed be uniquely determined from the FROG trace, e.g., Fig 3.10 (b) is an example of retrieved spectral intensity and phase of the pulse that created the FROG trace in Fig. 3.10 (a) (save a few trivial ambiguities). One reason that the FROG iterative retrieval algorithm converges well despite the absence of an absolute guarantee of convergence with the retrieval algorithm is that the FROG trace is "over-determined". The FROG trace, unlike the auto-correlation using N points to calculate the input pulse 2N-points field, has N^2 points. Because of this build-in data redundancy, FROG technique guarantees a solution for an experimental trace; in addition, it also gains the ability of retrieving from the FROG trace that has a large amount of random noise [93]. In the FROG retrieval algorithm, convergence is always determined by calculating the root mean square difference (FROG error) between the measured FROG trace and the trace computed from the retrieved pulse field. Indeed, FROG error gives an estimate on how reliable the retrieved spectral intensity and phase are.

Figure 3.9 is the schematic of our home-build FROG setup. We use this FROG for all our pulse characterization experiments. A 100 μm thick free-standing KDP crystal is

used for second harmonic generation. We use an image system after the crystal for imaging optimization purpose and providing a 10 times image magnification.

We used single shot and multi-shot FROG techniques in our research. A multi-shot FROG trace consists of a series of 1-D spectra taken by manually change the delay stage

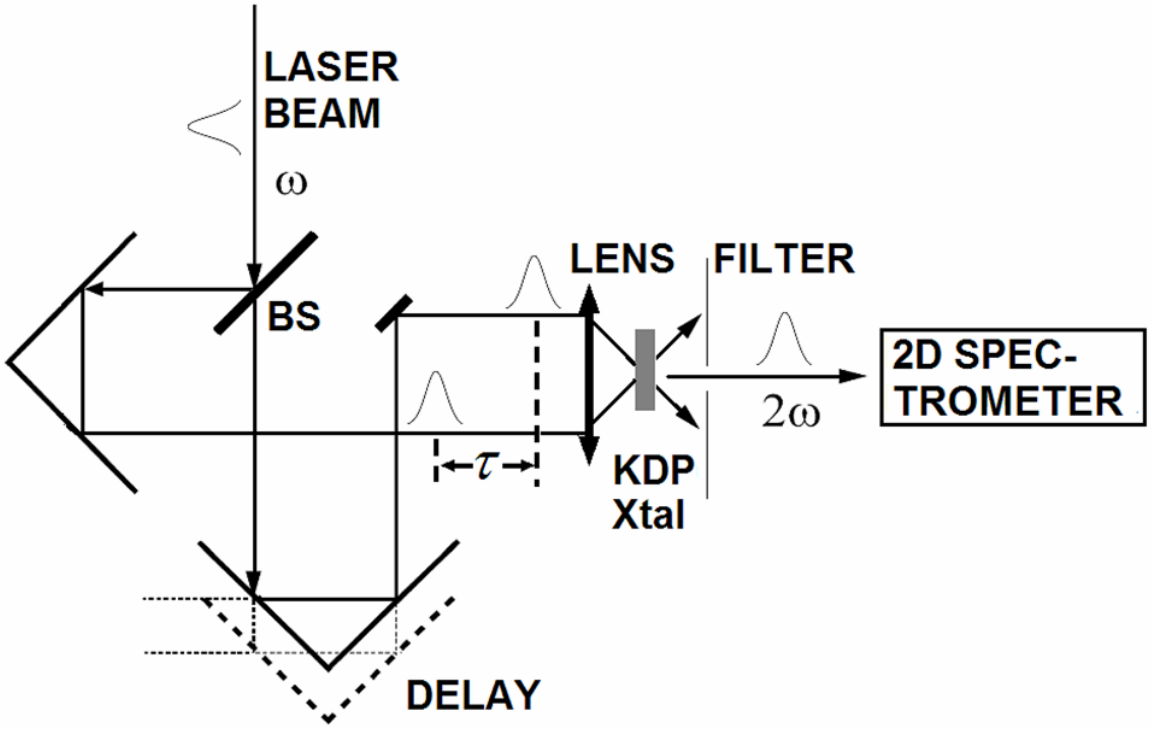

Figure 3.9: Schematic diagram of a SHG FROG apparatus. BS: beam splitter. Xtal: crystal.

position, whereas single-shot FROG trace itself is a 2-D image (delay vs. wavelength). Multi-shots FROG trace has a higher signal-to-noise ratio, but the whole acquisition time is much longer. To retrieve the FROG trace, we send the single-shot and multi-shot FROG trace to the retrieval algorithms (Femtosoft software). To get a reasonable FROG error, accurate delay axis and wavelength axis calibrations are required, as well as appropriate data correction procedures (background subtraction and flat-field correction). Fig. 3.10 is an example of using FROG technique in our example, with the original FROG trace shown in Fig. 3.10 (a) and retrieved spectral intensity and phase shown in

Fig. 3.10 (b). Note that the retrieved spectral phase shows an example of linear chirp (quadratic spectral phase) in the original pulse. The retrieved FROG error is 0.025 using FemtoSoft FROG V1.5.

FROG is a very useful technique, particularly as temporal and spectral information are simultaneously measured, yielding a phase reconstruction. The downside is that sometimes spatial chirp and pulse-front tilt can be an issue when reliable FROG traces are desired. A beam with spatial chirp has color varying spatially across the beam and it will tilt the FROG trice by a small angle. The pulse-front tilt means the pulse intensity front is not perpendicular to the pulse propagation vector and this effect will shift the zero delay line in the FROG trace. Furthermore, the FROG technique is not well suited for real time pulse monitoring and adaptive control experiments due to the time-consuming retrieval algorithms and occasionally expertise in the selection of reconstruction parameters. For other pulse characterization applications, FROG is an excellent choice.

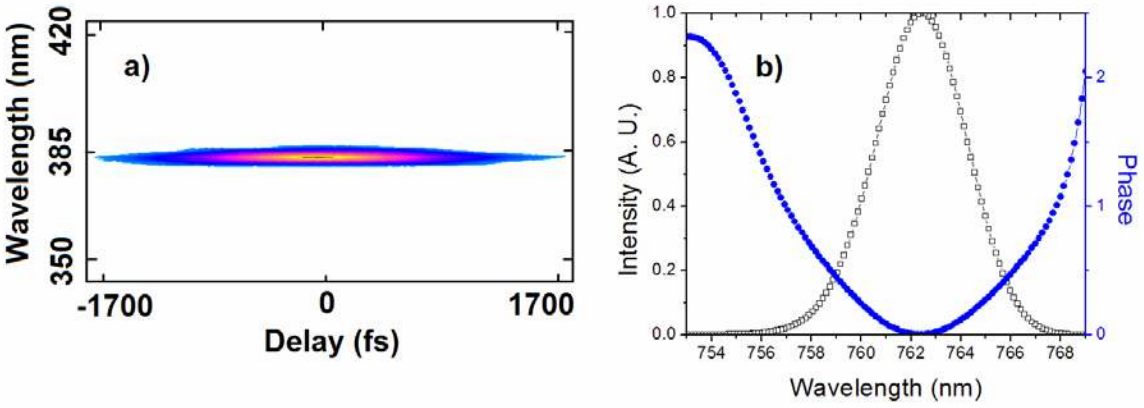

Figure 3.10: An example of experimental FROG trace and retrieved spectral intensity/phase profile correspond to the FROG trace. The spectral intensity is an example of Gaussian pulse and the spectral phase indicates a residual linear chirp for the original pulse.

3.4.3 Spectral Phase Interferometry for Direct electric-field Reconstruction (SPIDER)

The technique, spectral phase interferometry for direct electric-field reconstruction (SPIDER), is a specific implementation of spectral shearing interferometry [94, 95]. This interferometric technique is based on the measurement of the interference between two pulses with a certain delay in time. These two pulses are spectrally sheared, i.e., they are identical except for their central frequencies. The spectrum of this pulse pair is an interferogram signal [Fig. 3.11]

$$S(\omega) = I(\omega+\Omega) + I(\omega) + 2\sqrt{I(\omega+\Omega)I(\omega)}\cos[\phi(\omega+\Omega) - \phi(\omega) + \omega\tau] \quad (3.16)$$

where Ω is the spectral shear (the difference between the central frequencies of the pulse pair), τ is the time delay between the pulses, $I(\omega)$ and $\phi(\omega)$ are the pulse spectral intensity and phase.

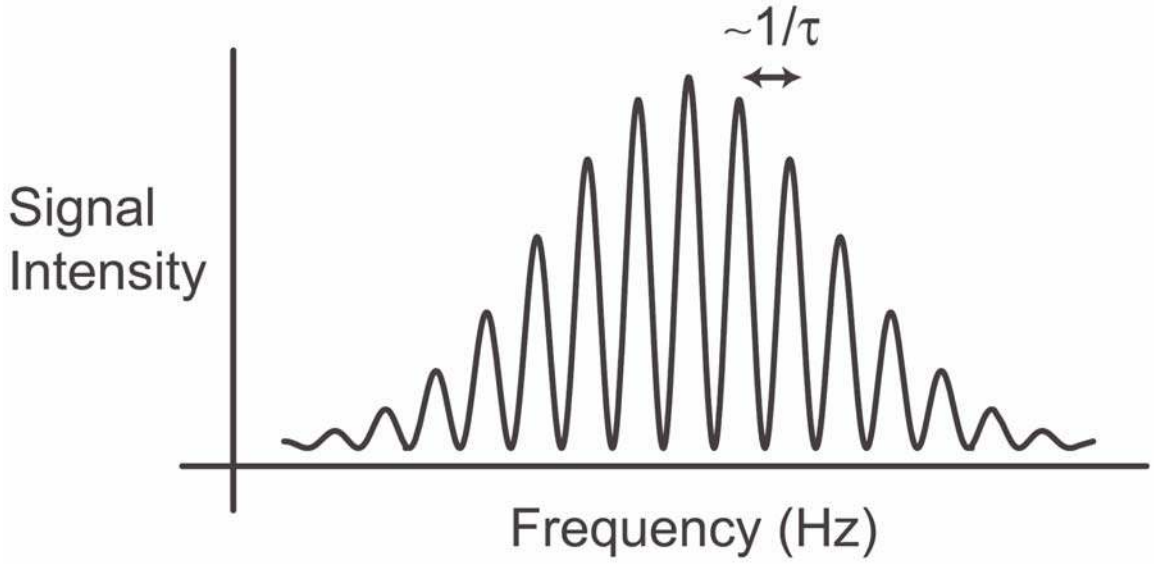

Figure 3.11: Plot of an ideal interferogram. The interferogram is of the form shown in Eq. (3.16). The nominal spacing between the fringes is 1/τ. Refer to Shuman et al. [96].

As mentioned in this section before, the full pulse characteristics in the frequency domain require determining both the $\sqrt{I(\omega)}$ and $\phi(\omega)$. The measurement of the electric

field is quite straightforward and the spectral phase can be extracted from the SPIDER interferogram. Evidently from the Eq. 3.16, the spectral shear Ω determines discrete spectral phase sampling resolution, as only the spectral phase at a series of spectral frequency separated by Ω can be determined. To utilize the SPIDER technique, the generation of spectrally sheared pulse pair is required. This is usually done [Fig. 3.12] by frequency mixing two pulse replicas, that is separated by delay time τ, with a chirped pulse in a nonlinear crystal. A pulse stretcher, e.g., a glass block in the Figure 3.12, is used to generate the chirped pulse. The chirped pulse needs to be much longer than the delay time τ to satisfy the condition that each pulse replica can frequency mix with different frequency in the chirped pulse in the crystal. As a result, the unconverted pulses are spectrally sheared. The resulting interferogram is resolved with a spectrometer. After the interferogram is sampled properly, the spectral phase information can be extracted from the data.

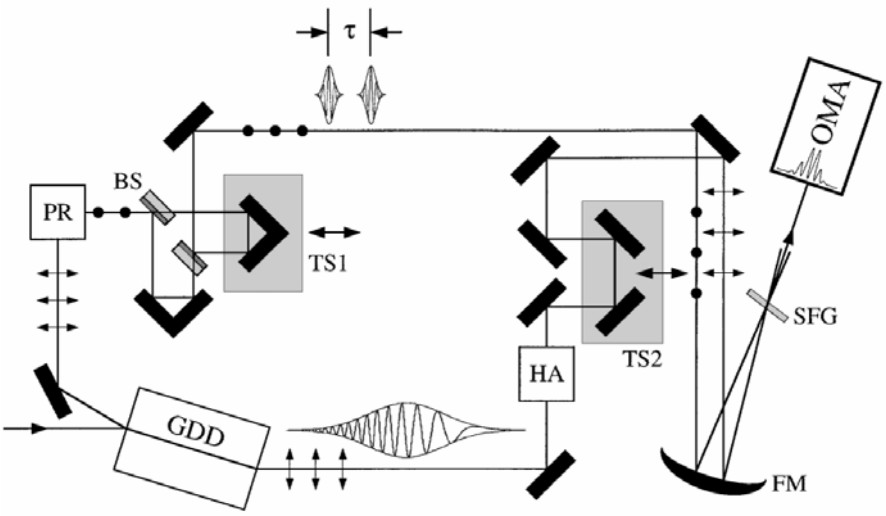

Figure 3.12: Schematic diagram of a SPIDER apparatus. BS: beam splitter. GDD: SF10 glass block. TS: translational stage for delay adjustment. FM: focusing mirror. OMA: optical multichannel analyzer. SFG: upconversion crystal (BBO). Refer to Gallmann et al. [107].

The SPIDER trace is one-dimensional, and the inversion is algebraic. The SPIDER pulse retrieval algorithm uses a direct inversion procedure [97], which is much faster comparing with the FROG's iterative algorithms. As a consequence, real-time measurements (with a 20-Hz refresh rate) from the output of a regeneratively amplified laser system have been obtained [96]. Meanwhile, combination with SPIDER and adaptive pulse control makes real-time ultrashort coherent control possible. However, SPIDER requires a different optical setup for measurement of different optical pulses, which limits its flexibility because prior knowledge of the pulse chirp is required. Furthermore, the accuracy of SPIDER is reliant solely on the initial calibration, which cannot be checked in the same way as FROG, in which marginals of the FROG trace can be used to highlight any calibration irregularities [98].

3.5 Pulse Shaping

Femtosecond pulse shaping [99] promises great advantages to the fields of fiber optics and photonics, ultrafast spectroscopy, optical communications and physical chemistry. Femtosecond pulse shaping also plays a major role in the field of coherent or quantum control [100], in which quantum mechanical wave packets or quantum state can be manipulated via the phase and intensity profiles of the input laser pulse. Changing the laser intensity temporal profiles can only be achieved by femtosecond pulse shaping. Meanwhile, several schemes have been proposed in which pulse shaping would favorably enhance laser-electron interactions. One application involves laser generation of large amplitude, relativistic plasma waves [101]. In recent years, the combination of the femtosecond pulse shaping with the adaptive control technique, i.e., adaptive pulse shaping, has led to several interesting demonstrations [102-104].

In this section we will lay out the schematics of pulse shaping techniques in frequency and time domain, the practical consideration for implementing pulse shaping technique, as well as configurations of the pulse shaper used in our experiments.

3.5.1 Femtosecond Pulse Shaping

Femtosecond pulse shaping has passive and active control methods. Passive methods use grating pairs or prism pairs to give a relatively fixed and limited control of the pulse, such as the pulse stretcher used in the SPIDER apparatus and the pulse compressor in CPA systems. Active control methods use programmable modulators, which perform a much powerful and robust control over pulse phase and/or amplitude. Active methods can be performed in two domain, frequency domain or direct in-time. Frequency domain femtosecond pulse shaping has been studied extensively and the technique is well-developed by now. The method is based on liquid crystal (LC) device or acoustic-optic modulator (AOM) placed in the Fourier plan of a grating based zero dispersion 4f-configuration (Figure 3.14) to experimentally control the spectral phase and/or intensity of the pulse. The different wavelengths are spatially separated and can then be addressed individually in this case. This turns out to be a great advantage in conjunction with genetic algorithm for adaptive pulse shaping, because the desired control pulse can have a rather random phase pattern. However, the setup requires careful realignment after changing the wavelength and its large size can be a limitation in some applications. The detailed description of the 4f Fourier domain pulse shaping using LC-SLM will be given later in this section.

Direct in-time femtosecond pulse shaping can be achieved using an acousto-optic programmable dispersive filter (AOPDF). Acousto-optic programmable dispersive filters are based on the propagation of light in an acousto-optic birefringent crystal [Fig. 3.13].

The interaction of an incident ordinary optical wave with a collinear acoustic wave leads to an extraordinary wave. The acoustic wave is modulated to achieve phase matching for the incident pulse to be scattered into the perpendicular polarization direction at different depth for different wavelength. Spectral phase and amplitude pulse shaping of a femtosecond optical pulse can then be achieved by controlling the frequency modulation and acoustic wave magnitude through the modulation of the RF voltage for the piezoelectric transducer. The optical output $E_{out}(\omega)$ can be related to the optical input $E_{in}(\omega)$ and electric driving signal $S(\omega)$ as [105]

$$E_{out}(\omega) \propto E_{in}(\omega) S(\alpha\omega), \tag{3.17}$$

with the scaling factor defined as

$$\alpha = \Delta n (V/c), \tag{3.18}$$

where Δn is the index difference between the ordinary optical wave and extraordinary wave and *V/c* is the ratio of speed of sound to the speed of light. $S(\omega)$ is numerically calculated and sent to the crystal.

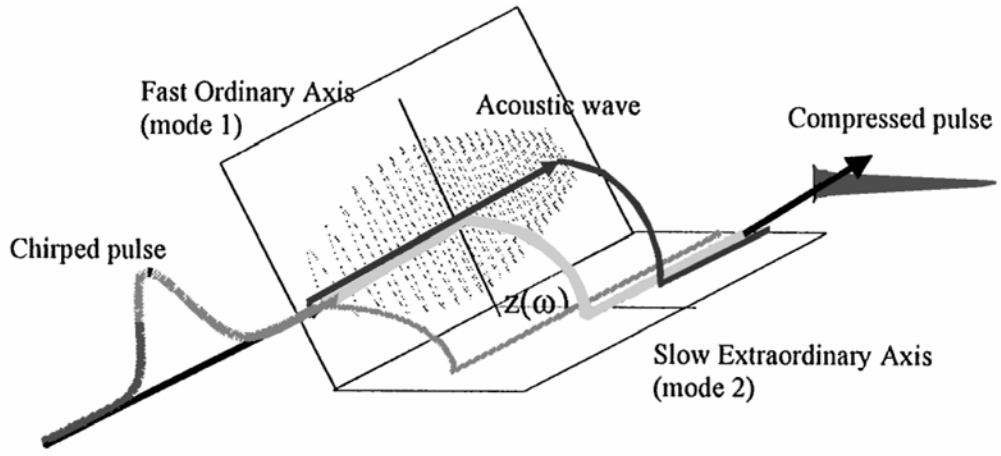

Figure 3.13: Principle of acousto-optic programmable dispersive filter (AOPDF). Compressed pulse is an example that AOPDF can be used as a pulse shaper to compensate the original chirped pulse phase. Refer to Verluise et al. [105].

The collinear acousto-optic interaction and the reduced size result in an easy-to-align device. Acousto-optic programmable dispersive filter have proven to be very useful to correct the time aberrations introduced in Chirped Pulse Amplifiers, for amplitude and phase control of ultrashort pulses [105], or even in characterization setups [106].

3.5.2 Fourier Domain Pulse Shaping Using Spatial Light Modulator

Spatial light modulator (SLM) has been widely used in the Fourier domain pulse shaping technique because of its programmable shaping ability of addressing both the phase and amplitude of each individual frequency component of the input pulse. Combining with the Genetic Algorithm's powerful abilities of efficiently searching the parameter space, adaptive pulse shaping using spatial light modulator has shown great potential to locate the right driving pulse for a specific application. In this section we will lay out the schematics of Fourier domain pulse shaping, followed by the discussion on how the SLM can be used to phase and amplitude control of the input pulse, as well as some experiment considerations.

3.5.2.1 Fourier domain pulse shaping

Fourier domain pulse shaping is the most successful and widely adopted pulse shaping method. Therefore, a setup consideration and design details will be discussed in this section. Figure 3.14 shows the basic Fourier domain pulse shaping apparatus, which consists of a pair of diffraction gratings and mirrors (or lenses), and a pulse shaping mask (LC-SLM). The individual frequency components contained within the incident ultrashort pulse are angularly dispersed by the first diffraction grating, and then focused to small diffraction limited spots at the back focal plane of the first mirror, where the frequency components are spatially separated along one dimension. Essentially the first mirror performs a Fourier transform which coverts the angular dispersion from the grating to a

spatial separation at the back focal plane. Spatially patterned amplitude and phase masks are placed in this plane in order to manipulate the spatially dispersed optical Fourier components. The second mirror and grating recombine all the frequencies into a single collimated beam.

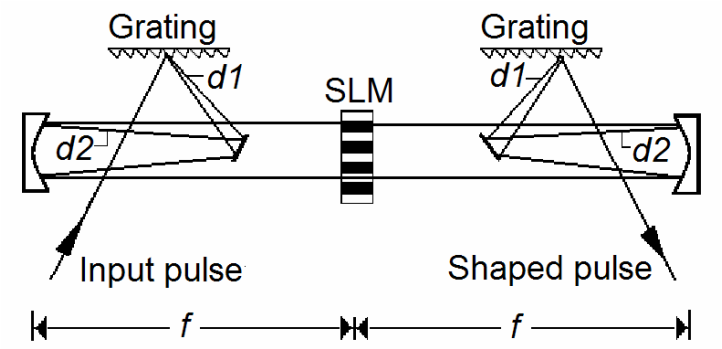

Figure 3.14: Schematic diagram of a Fourier domain pulse shaping apparatus using a LC-SLM. In this setup, d1+d2=f to maintain the 4f configuration. LC-SLM: Liquid Crystal Spatial Light Modulator.

In the 4f Fourier domain pulse shaper, the field immediately after the SLM mask M(x) is [99]

$$E_m(x,\omega) \propto E_{in}(\omega)\, e^{-(x-\alpha\omega)^2/w_0^2} M(x)\,, \tag{3.19}$$

where α is a frequency to space parameter written as

$$\alpha = \frac{2\pi c f}{\omega_0^2 d \cos(\theta_d)}, \tag{3.20}$$

and w_0 is the radius of the focused beam at the mask plan

$$w_0 = \frac{\cos(\theta_{in})}{\cos(\theta_d)}\left(\frac{f\lambda}{\pi w_{in}}\right). \tag{3.21}$$

In these equations, θ_{in} and θ_d are the incident angle and diffraction angle for the grating, d is the grating parameter, f is the focal length of the focusing mirror (or the lens), w_{in} is

the radius of the incident beam before the first grating, ω_0 is the central frequency and c is the speed of light.

For the discrete N pixel SLM device, the mask M(x) can be written as

$$M(x) = \left[H(x) \sum_{n=-N/2}^{n=N/2-1} \delta(x - nw_p) \right] \otimes rect(x / w_p), \tag{3.22}$$

where H(x) is the continuous mask that pre-defined for specific frequency filter, w_p is the physical width of each pixel of the SLM (see next section for details), the rectangular function is 1 for $|x| \le 1/2$ and 0 otherwise, $\otimes$ is for convolution.

Assuming a linear space to frequency mapping $x = \alpha(\omega - \omega_0)$, the final electric field after the shaper can be expressed as

$$e_{out}(t) \sim \left[e_{in}(t) \otimes \sum_{n=-N/2}^{n=N/2-1} H(t - n\frac{1}{\delta f}) \right] sinc(\pi t \delta f), \tag{3.23}$$

where H(t) is the Fourier transform of the function H(x), δf is the frequency bandwidth of each SLM pixel.

The setup of the Fourier domain pulse shaping requires that the output pulse should exactly reproduce the input pulse if no mask is presented in the back focal plan of the first mirror [99]. In another words, the grating and mirror configuration can not introduce extra dispersion. There are several considerations. First, the second grating has to be carefully placed so that the incident angle on the second grating equals the output angle of the first grating. Second, 4f configuration must be maintained, which means the grating pairs must locate in the outside mirror focal planes and two mirrors are separated

by 2f. Note that sometimes lenses are used in the pulse shaper; however, using mirrors instead of lenses can minimize the material dispersion.

3.5.2.2 Liquid crystal spatial light modulator (LC-SLM)

The pulse shaper in our experiments uses LC-SLM (CRI SLM128-NIR) as the pulse phase modulation component. The LC consists of long, thin, rod-like molecules which are aligned with their long axes along the y direction without the external electrical field (see Fig. 3.15). When the voltage V is applied on the LC cell in the z direction, electric dipoles are induced and the electric forces tilt the LC molecules along z direction; causing a change in the refractive index for pulse polarized in y direction, while the refractive index in the x direction remains constant [108]. Therefore, the polarization of the incoming electric field must be parallel to the orientation of the long axis (y axis) of the liquid crystal molecules for use of the cell as a phase modulator.

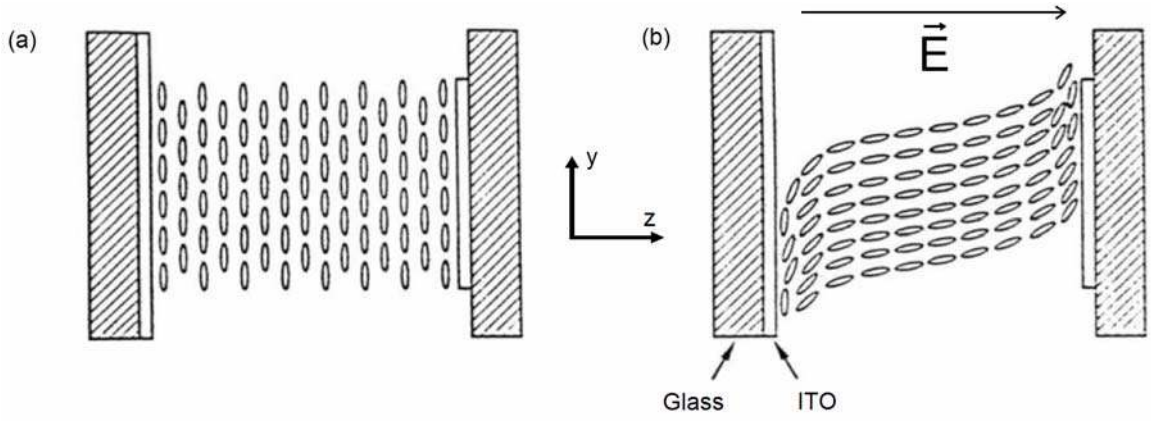

Figure 3.15: A sectional view of a liquid crystal layer between two glass plates. (a) No voltage applied. (b) Voltage is applied on the ITO electrodes in the z-direction. Refer to Weiner et al. [108].

The LC-SLM in our pulse shaper consists one LC layer, so it can only act as a pure phase modulator. However, SLM that consists two LC layers, in which their long axis are

in perpendicular directions, can be used as both a phase modulator and an amplitude modulator.

The LC-SLM used in our experiments has 128 pixels that are 2 mm high, 97 μm wide, 15 μm thick, and separated by 3 μm gaps [Fig. 3.16]. Therefore, the phase shift applied to pixel "i" by the change of its refractive index is equal to

$$\Delta\phi_i = \frac{2\pi\Delta n_i \cdot 15\mu m}{\lambda_i} \tag{3.24}$$

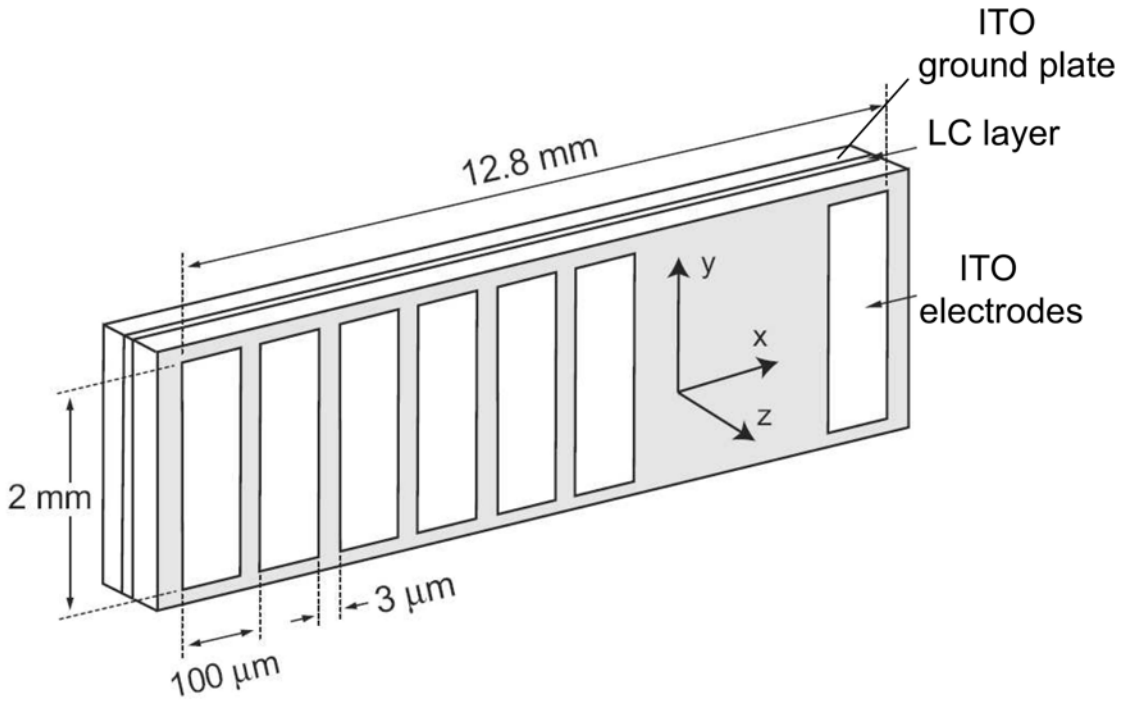

Figure 3.16: Illustration of LC-SLM array that consists of 128 LC pixels. The dimension and positions of the pixels are given as well. Refer to Weiner et al. [108].

3.5.2.3 Experimental considerations

For the most part, we perform frequency domain femtosecond pulse shaping using liquid crystal spatial light modulators in our research. Two identical gratings (1200 lines/mm) and spherical mirrors (f = 25 cm) are used in the setup. Depending on the experiments for different input central wavelength, the alignment is changed. If the

gratings and the SLM are designed for different pulse polarization directions, two half wave-plates have to be used before and after the SLM. The overall power convert efficiency is above 50% (comparing the pulse power launch into and after the pulse shaper). The SLM (CRI SLM128-NIR) positioned in the masking plane consists of 128 individually addressable elements 100 μm wide with a 3 μm gap between pixels. Configuration of the shaper, i.e. positions of optical components and input pulse angle, can be calculated by applying grating equation and geometrical optics. The goal is utilizing a large number of SLM pixels to achieve a high pulse shaping resolution.

Combining pulse shaper and open and/close close loop control (see chapter 4 for details) can yield great advantages in coherent pulse control over pulse interaction with PCFs. There are a few practical experimental considerations we need discuss before jumping into the next chapter.

1. High pulse shaping resolution

Using x as the coordinate in the transverse direction parallel to the front of the SLM, f for the focal length of the lens, θ_d for the diffraction angle and D for the grating line spacing, the pulse shaping resolution can be written as

$$d\lambda/dx = (D/f)\cos\theta_d . \tag{3.25}$$

With pulse bandwidth (baseline) and SLM pixel size (x direction) available, diffraction angle θ_d and incident angle θ_i for the first grating can be determined.

2. Liquid crystal voltage and phase shift calibration curve

A given phase shift caused by the refractive index shift on an individual SLM pixel is a function of both wavelength and LC voltage. Even for a fixed wavelength, the change

in refractive index shift and voltage response of the LC is not a linear function. So LC voltage and phase shift calibration curves are required.

Calibration curves can be established with the SLM placed between two crossed polarizers, each polarizer is placed 45 degrees to the long axis (y) of the LC molecules. Measuring the transmission coefficient as a function of driving voltage, for different wavelength and different SLM pixel (if necessary), and applying the equation $T = 0.5(1 - \cos\phi)$, LC voltage and phase shift calibration curves can be measured [Fig. 3.22]. For values that do not lie on one of the three curves, interpolation is used.

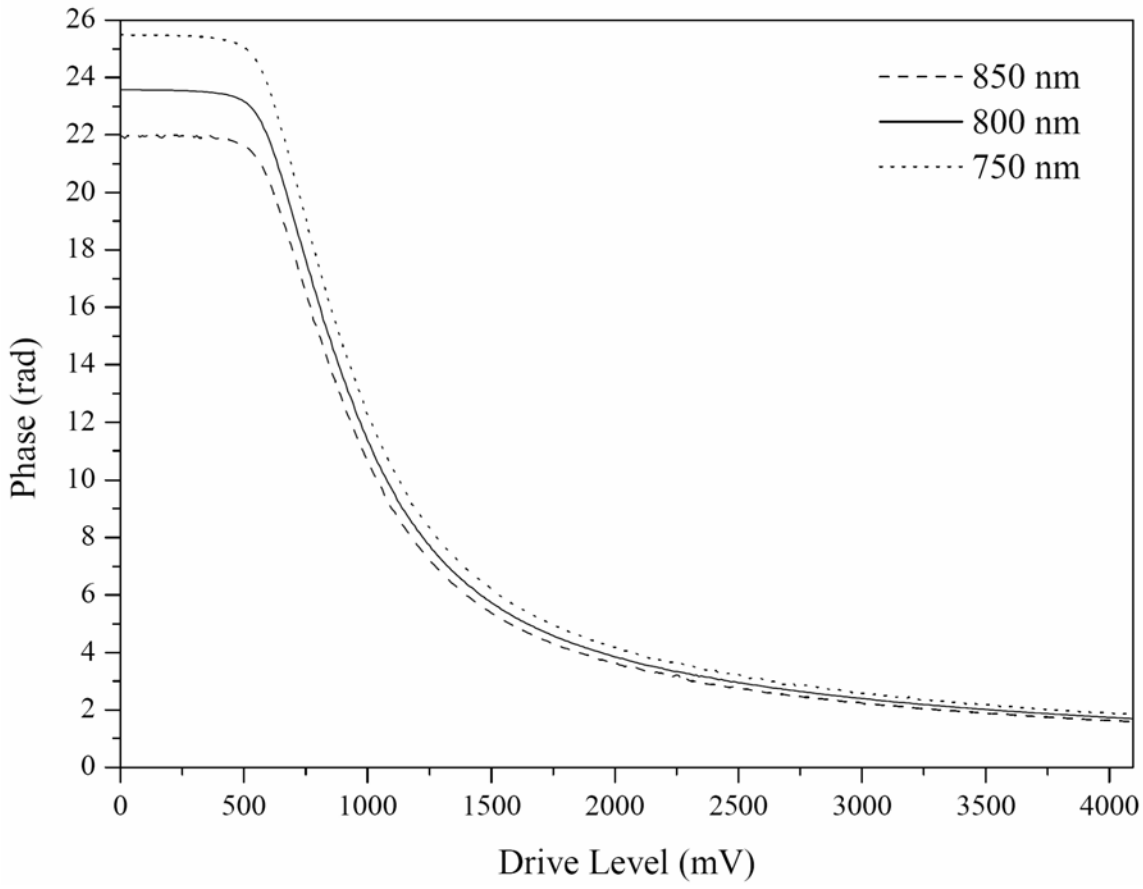

Figure 3.17: CRI SLM phase shifting curves as a function of drive voltage for750nm, 800nm and 850nm center wavelength. Linear interpolation can be applied to derive the phase shifting values for other wavelengths. Curves are measured by Anatoly Efimov.

3. SLM alignment

It is critical to perform transverse SLM alignment. Since phase shift is a function of driving voltage and wavelength, it is important to know the exact frequency component for each individual SLM pixel. Fortunately, this calibration is fast and easy. Applying a large phase jump to several SLM pixels across the SLM array, watching the spectrum change can easily determine the corresponding wavelengths. Note that this wavelength and SLM pixel number calibration should be a linear function, according to equation 3.25.

4. limitations of SLM

The most important limitation of SLM is the Nyquist limit. The Nyquist sampling theorem states that the phase difference between two adjacent SLM pixels should not be greater than π. Therefore, the phase jump across the SLM array should be limited within 128π. Else wise, it will cause an aliens problem.

The pixelation effect is due to the gaps between two neighboring pixels. The spectral components that pass through the gap, although a small portion, will not experience the refractive index change. If an exact pulse shape is desired, this effect is observable as small imperfections between the desired and the measured shape.

CHAPTER 4
CONTROL OF SUPERCONTINUUM GENERATION IN PCFS USING OPTIMALLY DESIGNED PULSE SHAPES

This chapter will focus on the control of the supercontinuum generation in microstructured fibers using femtosecond pulse shaping. Specifically, we will present results of our experiments on manipulating the bandwidth and shape of supercontinuum using optimally designed intensity profiles. In section 4.1, an overview of the two different types of control schemes will be presented, including both "open-loop" control and "closed-loop" control methods. In the ultrafast coherent control community, open-loop refers to control processes in which the optimal pulse shape for achieving a specific goal is determined by intuitive methods through careful consideration of the underlying physics. In closed-loop control, a learning algorithm is applied experimentally to synthesize the optimal pulse. We will discuss the considerations and setup of our open loop control experiment, as well as the NLSE simulation tools we used to model the experimental results in section 4.2. We investigate the effect of input pulse second order and third order spectral phase variations on the supercontinuum generation in section 4.3. In particular, effects of input pulse third order spectral phase on the supercontinuum with input pulse center frequency near the microstructured fiber zero dispersion (GVD) point are studied. Moreover, in section 4.4, we perform open loop control of pulse propagation self-steepening nonlinear effect in microstructured fiber using a pre-shaped "ramp" pulse to counteract the self-steepening. Simulation results based on the extended NLSE model corresponding to open loop control will also be presented and compared to experimental

results. A standard split-step Fourier algorithm [3] is used in the simulation model. Closed loop control experiments and results will be discussed in details in the next chapter.

4.1 Control of Supercontinuum Generation in PCFs

Continuum generation results from the nonlinear interactions between the input pulse and nonlinear media. Due to the intrinsic properties of nonlinear interactions, the resulting bandwidth of the continuum is much larger than that of the input pulse. Continuum generation has been studied over decades. Continuum generation of 400 nm bandwidth was first observed in the glass in 1970 [109]. Since then, the nonlinear media used for continuum generation has evolved from bulk glass and liquid to optical fiber. The low loss, tightly guided modes, and high nonlinearities of the optical fibers make them natural candidates for the supercontinuum generation. As such, optical fibers lead to a dramatic reduction in the pump power for the continuum generation. Various nonlinear effects such as SPM, SRS and FWM subsequently lead to the continuum generation in the optical fibers.

Due to its high material dispersion at Ti:Sapphire wavelengths, continuum generation in the optical fibers has been mainly in the telecommunication wavelength region (~1550 nm) before the invention of PCFs. In addition to their extremely small core sizes, PCFs revolutionized continuum generation by introducing a large amount of waveguide dispersion contribution, which can cancel the fiber material dispersion and yield zero dispersion for as low as 500 nm [48]. The advantages of PCFs manifest themselves through a continuum generation range from 400 nm to 1600 nm (supercontinuum) using only a Ti:Sapphire oscillator [6]. Since then, supercontinuum

generation has quickly found applications in various fields such as telecommunication, optical metrology and medical science.

In fact, the nonlinear mechanisms that lead to the supercontinuum generation in the PCFs are in no way different from that of continuum generation in conventional fibers. But in PCFs, the nonlinear interactions usually happen within the first several millimeters of the fiber length and in a much larger scale. A large amount of research in the area of supercontinuum generation in PCFs have been performed to explain the active roles of various nonlinear interactions that lead to the supercontinuum generation, including soliton generation and splitting, SPM, SRS, etc. Supercontinuum generates in PCFs as a result of high order soliton generation and splitting, followed by various other nonlinear interactions slight changing the supercontinuum envelope as propagating along the PCFs.

Supercontinuum generation in PCFS is nonlinear processes in the extreme. Large modulation structures are easily seen in the continuum envelope due to the soliton splitting. Meanwhile, sharp sub-nm continuum features vary drastically from shot to shot [9, 13], as both the experimental and simulation results show that supercontinuum generation is extremely sensitive to the input pulse power fluctuation. In figure 4.1, left figure shows the experimental supercontinuum fine structure variation from three different shot, measured by X-FROG. Simulation result shown in the right figure 4.1 also reveal that for 1% input pulse power fluctuation, although the continuum envelope does not show dramatic change, the fine structures of the supercontinuum change drastically. This drawback greatly affects some of the supercontinuum generation applications, such as pulse compression and high precision optical metrology. Various research activities have been carried out to study the stabilities of the supercontinuum generation. In general,

these research interests include variation of the input pulse properties, microstructured fiber propagation length effects [15] and tailorable dispersion properties. Our approach in Chapter 6 will focus on the simulation of utilizing dispersion flattened microstructured fiber to study the pulse compression application.

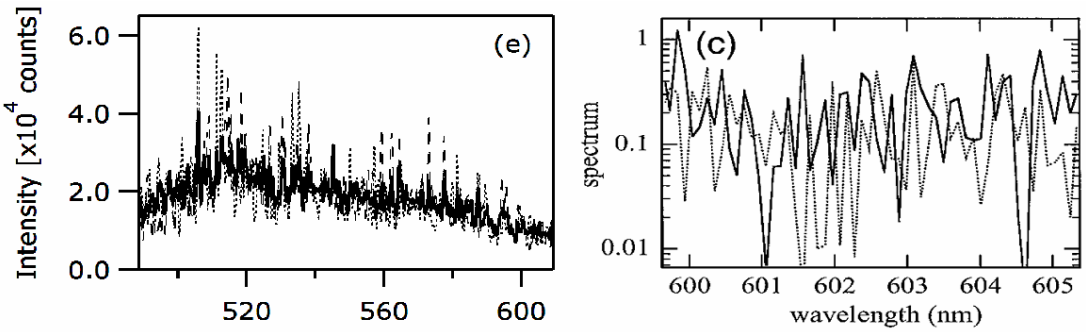

Figure 4.1: Sub-nm supercontinuum feature fluctuations as a result of input pulse power fluctuation. Left figure, experimental result of supercontinuum fine structure variation from three different shots, refers to Gu et al. [13]. Right figure, simulation of sub-nm supercontinuum feathers fluctuation as the input peak power varies by 1%, refers to Gaeta [9].

Controlling nonlinear optical processes in microstructured fiber is in general difficult, resulting from their intrinsic "nonlinear" responses to the input fields. Meanwhile, controlling the supercontinuum generation process in microstructured fibers is important for a number of applications. It allows us to extensively study various nonlinear processes and dispersion effects that lead directly to the fascinating supercontinuum generation, as well as gain the ability to generate the supercontinuum which properties are suited for one particular application.

It is evident that the supercontinuum generation and pulse nonlinear propagation in the microstructured fibers strongly depend on both the input pulse parameters and microstructured fiber properties. The "control knobs" for supercontinuum generation in the microstructured fiber can therefore be characterized as the following two categories. "Control knobs" related to the microstructured fiber properties include simple controls

such as fiber length and more advanced controls such as fiber dispersion and nonlinear properties. As mentioned in the chapter 2, fiber dispersion properties can be engineered by choosing the proper fiber parameters such as air hole size and pitch; meanwhile changing the core diameter can subsequently alter the nonlinear response of the microstructured fiber. The input pulse parameters, on the other hand, are much easier to handle and have a larger number of "control knobs". One can easily enumerate many input pulse parameters such as pulse power, wavelength, polarization or even the control of pulse chirp of some kind. Apolonski's results published in 2002 examined the influences of these control "knobs" on the supercontinuum generations [110].

More generally, Fourier domain pulse shaping [99], in which Fourier synthesis methods are used to generate nearly arbitrarily shaped ultrafast optical waveforms has been proven to be a powerful tool and have applications in many optical fields such as high power laser amplifiers, quantum control and optical communications. When coupled with adaptive or learning algorithms [111], Fourier domain pulse shaping has shown to be very effective in exercising control over nonlinear optical processes and producing a specific "target" nonlinear output state.

Two distinct control methods, open loop control and closed loop control, can be utilized to perform the Fourier domain pulse shaping. In general terms, open loop control is defined as the application of specific pulse or sequence of pulses and is carried out irrespective of the outcome of the experiment. In particular, for the pulse shaping technique, open loop control method utilizes knowledge of the underlying physics to intuit or derive a suitable control pulse. For example, the fundamental dark soliton was observed in optical fibers utilizing specially shaped and asymmetric input pulses, which

is in quantitative agreement with numerical solution to the nonlinear Schrödinger equation [112]. Open loop pulse shaping shows great advantage in the coherent control regime. Ultrafast coherent control of excitons in quantum wells use intuitively shaped pulse trains to investigate the generation process and intermediate virtual states in quantum structures [113]. Coherent control of Bloch oscillations using open loop pulse shaping provides a way to control the emitted THz radiation [114]. These are but a few of the recent applications of coherent control with shaped pulses. For pulse nonlinear propagation in the microstructured fiber, the chirp (or the spectral phase) of the input pulse can be altered with much higher resolution in the Fourier pulse shaping comparing to that of Apolonski where multiple pairs of chirp mirrors were used; therefore gaining better abilities on how the input pulse spectral phase can affect the supercontinuum generation. Meanwhile, using the phase sculpted "ramp" pulse to counteract self-steepening nonlinear effect allows us to suppress the blue-shifted continuum generation. Closed loop control, also referred as adaptive control, involves "feedback" through the repetitive application of optical waveforms synthesized using learning algorithms to ensure that the physical goals are met. Closed loop control coupled with Fourier domain pulse shaping have become a powerful means for optimizing a particular physical process. Closed loop control experiments and results will be discussed in details in the next chapter. To our knowledge, this dissertation and its related papers investigate for the first time how Fourier domain pulse shaping can be used to control the evolution the nonlinear pulse propagation in microstructured fibers.

4.2 Open Loop Control Experiment Setup and NLSE Simulation

We use two laser systems in the open loop control pulse shaping experiments, depending on the experiment of interest. The Mira 900 Ti:Sapphire laser system

generates pulses of 76 MHz repetition rate, with 6 nJ pulse energies, 200 fs pulse duration and pulse central wavelength is tunable from 700 nm to 900 nm. The bandwidth of the output pulse is ~5 nm, and the Mira 900 is used primarily to study the effect of third order input pulse phase on the supercontinuum generation when the input pulse's central wavelength is close to zero GVD point the microstructured fiber (~ 763 nm). For other open loop control experiments, we use a 82 MHz, 30 fs Ti:sapphire laser producing 3 nJ pulses that centered at 800 nm. The bandwidth of this laser system is ~65 nm, a much larger bandwidth comparing to that of Mira 900 as one can easily see by comparing the pulse durations of these two laser systems. The output pulse train is phase-only shaped (pulse shaper that only modulates the pulse spectral phase) by an all-reflective 4f Fourier domain pulse shaper using a 128 pixel programmable liquid crystal spatial light modulator (LC-SLM) as described in Chapter 3. The focal length of the mirror used in the pulse shaper is 25 cm. Because the two laser systems have different central wavelengths and bandwidths, two considerations are taking into account with the design of pulse shaper to get high pulse shaping resolutions. 300 lines/mm grating pairs are used for Ti:Sapphire laser with 65 nm bandwidth and 1500 lines/mm grating pairs are used for Mira 900 laser with 5 nm bandwidth; the grating line spacings correspond to 3.3 μm and 0.67 μm , respectively. Input pulse incident angles for pulse shapers can be easily calculated according to equation 3.16 to utilize large number SLM pixels and yield high pulse shaping resolutions. The power transmission through the pulse shaper is approximately ~40%. After the pulse shaper, the pulse is coupled into a piece of microstructured fiber using a 100x objective (Vickers w4017) of a numerical aperture 1.3. Meanwhile, the shaped pulse is characterized by the second harmonic generation

frequency resolved optical gating (SHG FROG) to verify the pulse temporal structure. Some dispersion is introduced by the glass in the objective; this is measured separately and compensated for in our experiments. The microstructured fiber consists of a 1.7 μm diameter silica core surrounded by an array of 1.3 μm diameter air holes in a hexagonal close-packed arrangement. The microstructured fiber has a zero GVD wavelength ~760 nm and the coupling efficiency using the objective is estimated to be 20%. The supercontinuum generated in the microstructured fiber is collimated using a 50x objective and the spectrum is recorded using a 0.25 m spectrometer with a CCD detector. An example of the supercontinuum generation in our experiment is show in figure 4.2. Figure 4.3 shows the schematics of open loop control experiment setup.

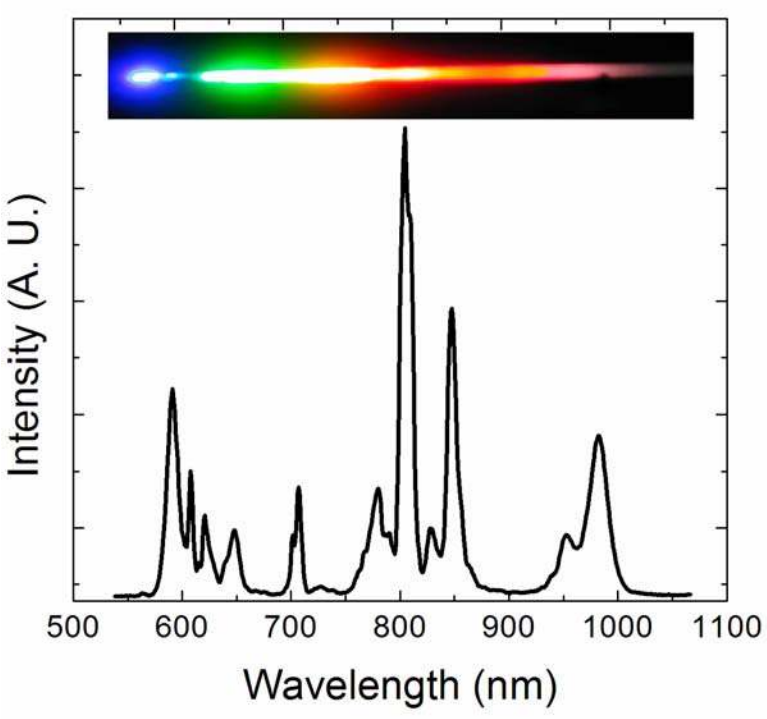

Figure 4.2: An example of supercontinuum generation in experiment. Inset: a dramatic picture of supercontinuum after a grating, taken by Anatoly.

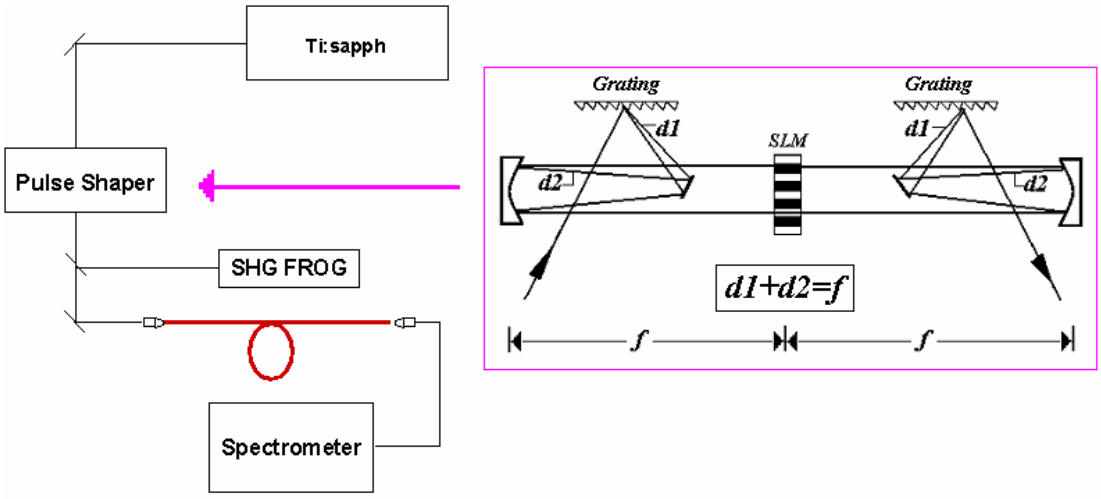

Figure 4.3: Schematic diagram of the open loop control experiment. SLM: Spatial light modulator. SHG FROG: Second harmonic generation frequency resolved optical gating.

We follow the experimental considerations discussed in section 3.5.2.3 to setup and characterize the pulse shaper. For pulse shapers corresponding to different input central wavelengths, we use LC voltage and phase shift calibration curves (Fig. 3.16) and linearly interpolate the values that do not lie on the curves. Meanwhile, we perform wavelength-to-pixel calibrations for the pulse shaper setups to verify the phase shaping resolutions. In both cases, ~100 pixels over the whole 128 pixels are used for the pulse shaping. In addition, both autocorrelation and FROG are used to verify the output pulse is the replica of the input pulse when imposing zero additional phases on the pulse shaper.

To modal our experiments, we use an extended nonlinear Schrödinger equation [3] (NLSE, described in details in Chapter 2) with a standard split-step Fourier algorithm to compute the propagation of shaped pulses in the microstructured fiber. The NLSE has been proven to be valid for femtosecond pulses in the limit that the optical frequency bandwidth approaching the central frequency of the pulse [3, 9, 115]. A higher order split step method [115] is used to insure the stability for high input peak powers. In the

simulation model, the time resolution is 0.5 fs, the total sampling points is 2^{14}=16384 and the propagation step size is chosen as 0.5 mm. The frequency resolution is therefore 111.1 GHz. The input temporal profile of the pulse for the NLSE is calculated from the inverse Fourier transform of the experimentally determined input pulse spectrum and spectral phase, in which the latter is specified from the additional phase induced by the pulse shaper in the condition that the phase of the original unshaped pulse has been well compensated (transform-limited pulse). For the fiber characteristics including the fiber dispersion parameters, we use the parameters taken from the literature for input pulse central wavelength of 770 nm [9]. Here is the list of fiber characteristics that we use in our simulations.

Table 4.1: List of the microstructured fiber parameters used in the NLSE simulation model.

Parameter (unit)	Value
n_2 (cm^2W^{-1})	2.0×10^{-16}
γ $(km^{-1}W^{-1})$	96.3
A_{eff} (μm^2)	1.63
β_2 (ps^2km^{-1})	-0.72
β_3 (ps^3km^{-1})	2.16×10^{-2}
β_4 (ps^4km^{-1})	1.296×10^{-5}

4.3 Influences of Quadratic and Cubic Spectral Phase on Propagation Dynamics

As the first example of open loop pulse shaping experiment, we examine the influences of quadratic and cubic spectral phase to the output supercontinuum generation when the input central wavelength is in the anomalous dispersion region of the

microstructured fiber. For the Ti:Sapphire 800 nm laser system used in this experiment, the output pulse peak power is 100 kW. Considering 40% power transmission through the pulse shaper and 20% fiber coupling efficiency, it corresponds to a nonlinear length of ~1 mm (defined in equation 3.25) calculating from the fiber parameters list in table 4.1), which is 10^3 times shorter than the dispersion length for this microstructured fiber. This ratio manifests itself through the drastic nonlinear effects in the microstructured fiber which consequently lead to the supercontinuum generation. The magnitudes of various nonlinear effects (i.e., supercontinuum bandwidth) taken place in the microstructured fiber critically depend on the input pulse peak power, which is determined by the input pulse spectral phase given a fixed spectrum. Figure 4.4 illustrates this point, in which simulation results using the experimentally determined Ti:Sapphire laser spectrum show pulse peak intensity variations as a function of pulse spectral phase. Note that the pulse spectral phase is determined by the following equation.

$$\phi(\omega) = \phi^{(1)}(\omega - \omega_0) + \frac{\phi^{(2)}}{2}(\omega - \omega_0)^2 + \frac{\phi^{(3)}}{6}(\omega - \omega_0)^3 + \cdots, \tag{4.1}$$

where ω_0 is the central angular frequency and the $\phi^{(i)}$ are the higher order phase terms defined in equation 3.11. Note that the linear phase shift does not affect the pulse peak intensity, therefore is not considered in the discussion. In Figure 4.4 (a) and (b), the pulse peak intensity drops continuously with the increases of both cubic and quadratic spectral phase. Since pulse peak intensity changes do not depend on the sign of the introduced spectral phases, only positive cubic and quadratic spectral phase are shown in the figures. It is quite obvious that the peak intensity dropping is much faster for the quadratic spectral phase coefficients than the cubic phase coefficients, as the dropping ratio is over 50% for the quadratic phase of 2000 fs^2 and less than 1% for the cubic phase of 2000 fs^3,

although it also applies for the phase changes according to equation 4.1. In addition, the temporal intensity profiles showing in figure 4.4 (c) illustrate this huge dropping ratio difference between the quadratic phase and cubic phase. Note that for both quadratic and cubic phase variation, acquiring maximum pulse peak intensity implies a zero spectral phase (transform-limited) for the input pulse.

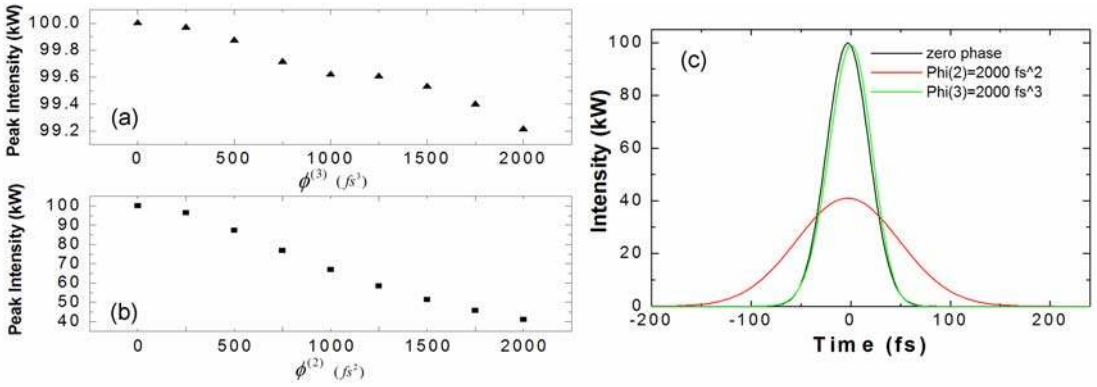

Figure 4.4: Simulation results of the pulse peak intensity as a function of pulse spectral phase. In (a) and (b), the pulse peak intensity verses pulse cubic and quadratic spectral phase, respectively. (c) Comparison of the pulse temporal intensity with transform-limited pulse, pulse with quadratic spectral phase of 2000 fs^2 and cubic spectral phase of 2000 fs^3.

Based on previous discussions, we investigate the influences of input pulse quadratic and cubic spectral phase on the supercontinuum generations. The experimental results showing in figure 4.5 nicely authenticate the theoretical explanations. The spectra of supercontinuum generation change dramatically upon variations of input pulse quadratic spectral phase. The bandwidth of the supercontinuum is greatly suppressed when introducing extra quadratic spectral phase, reducing from 450 nm for the transform-limited input pulse to 250 nm for the induced quadratic spectral phase of the largest magnitude. There are only slight (but experimentally measurable) influences of the cubic spectral phase on the supercontinuum generation. Corresponding to the pulse peak intensity variations for introduced pulse quadratic and cubic phase, the latter shows a

much smaller supercontinuum generation influences, although the maximum supercontinuum bandwidth is still generated by a transform-limited input pulse. There is also an added discovery when looking into the experimental data. We expect to see the

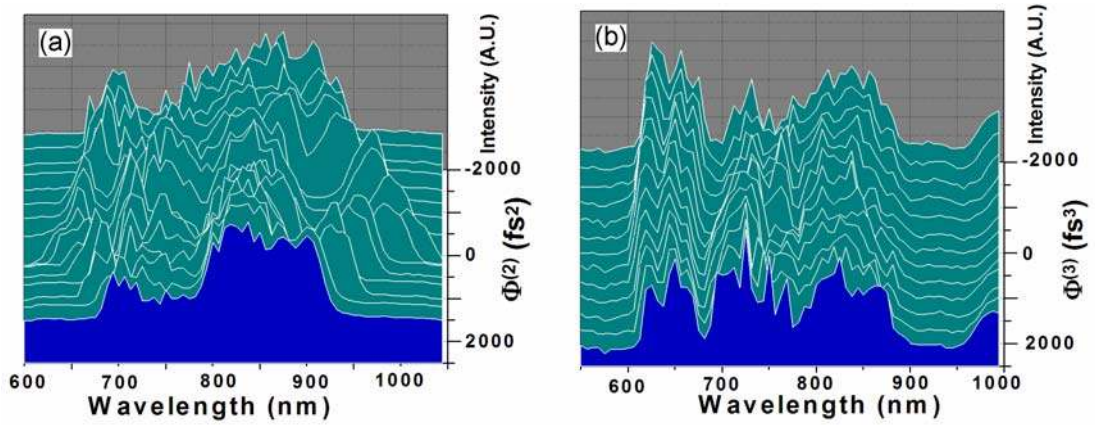

Figure 4.5: Experimental results of supercontinuum generation dependence on the input pulse quadratic and cubic spectral phase. In both (a) quadratic phase variation and (b) cubic phase variation, the supercontinuum obtains the broadest bandwidth for transform-limited input pulse.

soliton generation from the supercontinuum since the input central wavelength is in the anomalous dispersion region and soliton generation results from the interplay between the fiber anomalous dispersion and self-phase modulation effect. Both figures show the evidence of soliton generation, as evidenced by the spilling off of a large spectral component on the long wavelength side of the supercontinuum and its subsequent shift to the red side of the spectrum as the phase is minimized. The first interesting observation is that soliton generation disappears when large magnitudes of the spectral quadratic phase are presented; resulting from the steep peak intensity drop for the input pulse and that soliton order is proportional to the square root of input pulse peak power. Meanwhile, whereas the spectral quadratic phase acts as a coarse control knob for the positions of soliton generation, the spectral cubic phase shows the fine tunability. Therefore, it is understandable that the peak intensities of the input pulse actually perform the control

over soliton generation, as further illustrated by both the closed loop experimental and simulation results discussed in the next chapter.

To further investigate the influence of the input pulse spectral phase on the pulse propagation dynamics, we study the case that the input pulse frequency is near the zero GVD point of the microstructured fiber. It is known that finite bandwidth pulses centered at the zero dispersion wavelength experience both normal and anomalous dispersion. Near the zero GVD point of the microstructured fiber the dispersion length of the third order fiber dispersion (TOD), L_{3d}, is comparable to or even smaller than that of second order fiber dispersion (SOD) L_{2d}. Here $L_{i\_d} = \tau^i / |\beta_i|$ where τ is the input pulse duration and β_i is the ith order fiber dispersion parameter. Therefore TOD plays an important role for the fiber dispersion property as well as the interplay between the fiber dispersion and self-phase modulation nonlinear effect when L_{3d} is comparable to L_{2d}. In addition, for the input pulses presenting a cubic spectral phase, the intrinsic fiber TOD can compensate the cubic spectral phase and compress the input pulse, providing the sign of the cubic spectral phase is opposite to the sign of the intrinsic TOD; therefore enhancing the magnitude of nonlinear effects (i.e., SPM) by increasing the pulse peak power as pulse propagates along the fiber and generating a broader supercontinuum. When the signs of input pulse cubic spectral phase and fiber TOD are the same, nonlinear effects are suppressed due to the fact that the fiber TOD induces extra spectral phase and lower the pulse peak power along the propagation length.

The zero GVD point of the microstructured fiber listed in the table 4.1 is estimated to be ~760 nm. To make the input central wavelength close to the zero GVD point of the microstructured fiber, in the first set of experiments, we use our home-build Ti:Sapphire

oscillator and push the laser pulse central wavelength down to 770 nm. At this particular wavelength, $L_{3d} \approx L_{2d}$, as one can easily see by the calculation using the listed parameters. Upon changing only the cubic spectral phase of the input pulses, the supercontinuum maximum bandwidth should occur for a $|\beta_3| = |\phi^{(3)}| / L_{fiber}$, where β_3 is the fiber TOD parameter and $\phi^{(3)}$ corresponds to the input pulse cubic spectral phase. Note that in this equation the signs of β_3 and $\phi^{(3)}$ should be opposite, as only in this case the fiber TOD can interact with the propagating pulse to compensate the pulse intrinsic $\phi^{(3)}$. We use two pieces of microstructured fibers with different fiber length of 5 cm and 70 cm to study the influence of input pulse cubic spectral phase on supercontinuum generation bandwidth. As we can see from figure 4.6 (a), the experimental output spectra bandwidths from the 5 cm microstructured fiber show a dramatic asymmetry upon examining the sign change of the input pulse cubic spectral phases, indicating fiber TOD dispersion has a different effects on the positive and negative pulse cubic spectral phases. The maximum bandwidth occurs when the input pulse $\phi^{(3)}$ is -500 fs^3. This corresponds to the fiber TOD parameter β_3 of a value +0.01 ps^3/km, which is in reasonable agreement with the reported β_3 value above. According to the equation, for the 70 cm microstructured fiber, proportionally more $\phi^{(3)}$ is needed and the GVD broadening will play a larger role, thus the effects of pulse cubic phase should be minimal when imposing same amount of $\phi^{(3)}$ as for the short fiber, which can be seen in figure 4.6 (b).

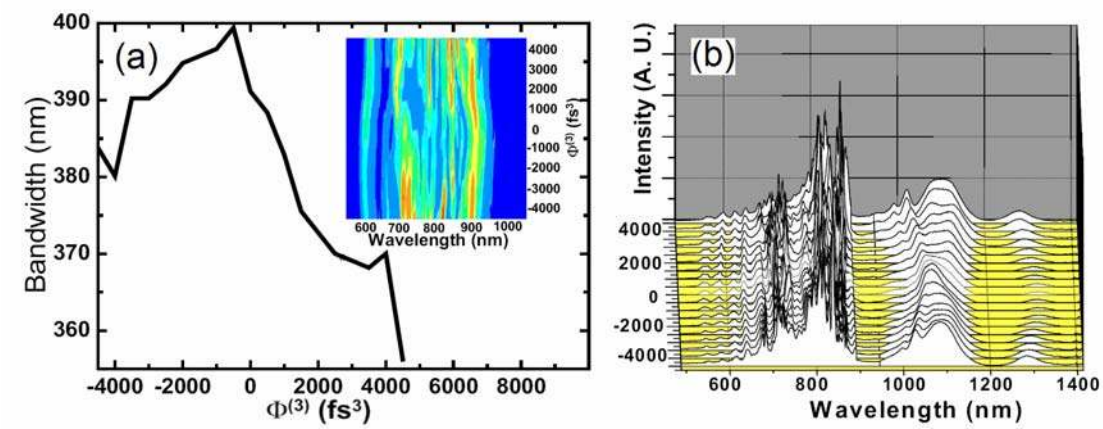

Figure 4.6: Experimental results of supercontinuum generation bandwidth from 5 cm and 70 cm microstructured fibers as a function of input pulse cubic spectral phase. (a) Bandwidth changes of SC generation from 5 cm MSF with variation of input pulse $\Phi^{(3)}$. Inset: output spectra from a 5 cm MSF with variation of input pulse $\Phi^{(3)}$. (b) Bandwidth of SC generation from 70 cm MSF with variation of input pulse $\Phi^{(3)}$.

In order to further exam this effect and move closer to the zero GVD point of the microstructured fiber, we use the Mira 900 wavelength-tunable laser oscillator. It has a wavelength-tunable range of 700 nm to 900 nm. The drawback is that the bandwidth of the Mira 900 laser pulse (5 nm) is rather small compare to the home-build Ti:Sapphire laser. Therefore, to see an enhanced effect of the fiber TOD comparing to the first set of experiments, the central wavelength of the Mira system has to be tuned very closely to the absolute zero GVD point of the fiber. However, the fiber parameters provided in table 4.1 are only estimated values at this precision level, and the pulse shaper also needs to be adjusted each time when the tuned central wavelength is changed. In order to find the absolute zero GVD point of the fiber, we first bypassed the pulse shaper and projected the laser beam directly into the microstructured fiber and find that output spectra have the maximum bandwidth at 763 nm. Since input pulses have a small bandwidth and experience the minimal GVD at zero GVD point, thus generating maximum bandwidth supercontinuum at this wavelength, 763 nm is the zero GVD point of the fiber. Based on

the previous discussion, we investigate the influence of input pulse cubic spectral phase on the supercontinuum generations at this particular wavelength. Both the experimental and simulation results are shown in figure 4.7 (a) and (b), respectively; the red curves are the output supercontinuum spectra for transform-limited input pulses. Since we use 45 cm of microstructured fiber, in order to see the optimal supercontinuum generation, the amount of input pulse cubic spectral phase is changed proportionally. In figure 4.7 (a),

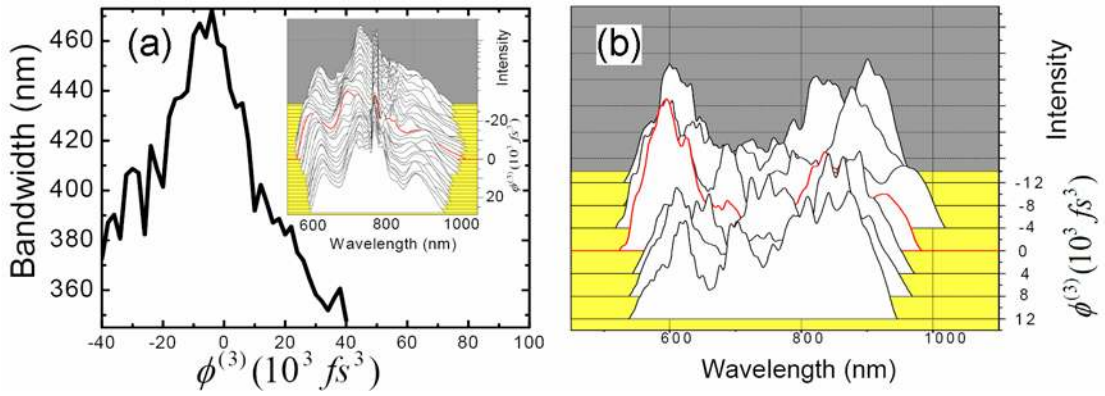

Figure 4.7: Experimental and simulation results of supercontinuum generation bandwidth from a 45 cm microstructured fiber as a function of input pulse cubic spectral phase. The input pulse central wavelength is at the zero GVD point of the fiber. (a) Experimental results of bandwidth changes of SC generation with variation of input pulse $\Phi^{(3)}$. Inset: experimental output spectra. (b) Simulation result of bandwidth changes of SC generation with variation of input pulse $\Phi^{(3)}$.

the experimental results show a considerable improvement compare to that of the 770 nm input central wavelength, as the maximum bandwidth expansion for the supercontinuum generation is nearly doubled. It is also evident from the inset of the figure 4.7 (a) that the bandwidths of the output spectra increase upon inducing proper amount of negative cubic spectral phase, while decreasing continuously for positive cubic spectral phase variations. The modulation in the bandwidth verses input cubic spectral phase curve is due to the laser power fluctuation. The simulation results (figure 4.7 (b)) show a good agreement with the experimental results. The maximum bandwidth of the supercontinuum spectrum

occurs for the same amount of input pulse cubic spectral phase change as the experimental results and the red sides of supercontinuum generation shows the exact same tendency as the experimental results.

Finally, before concluding this section, we discuss more about the phase compensation to generate a transform-limited input pulse. A transform-limited input pulse is the prerequisite to investigate the influence of input pulse spectral phase on the supercontinuum generations. Depending on different experimental conditions, i.e., different input laser systems and pulse shaper setups, one can use autocorrelation or SHG FROG to verify if the input pulse is indeed a transform-limited pulse. As discussed in the last chapter, autocorrelations can be used to properly adjust pulse shaper configuration and perform a preparatory exam on the transform-limited property of the pulse. We use autocorrelation to fine-tune the pulse shaper setups for both laser systems. However, when utilizing Mira 900 laser system, the back reflection of the input laser pulse on the microstructured fiber coupling surface travels back to the laser cavity, as a result of a good cleaving and flatness of the fiber tip. Therefore, the laser mode-locking conditions are disturbed and can not maintain a proper working condition. For the home-build laser system, a pinhole is pre-placed and the back reflection intensity is decreased, therefore the laser mode-locking disturbance is not observed. We choose to use a Faraday isolator to cut off the feedback to the laser, in this case, the unwanted back reflection. A Faraday isolator, by its definition, uses Faraday Effect to transmit the polarised light in only one direction. Using the Faraday isolator, however, will induce a considerable amount of quadratic spectral phase to the input pulse. In order to compensate this extra quadratic phase, we use SHG FROG to characterize the pulse after the Faraday isolator and acquire

the phase information. With the pulse shaper introducing opposite measured phase on the pulse and therefore compensating the residual quadratic phase, we use the SHG FROG again to verify the transform-limited pulse generation. The FROG retrieved spectral intensities and phases before and after the phase compensation are shown in figure 4.8 (a) and (b), respectively. Obviously, the extra phase induced by the Faraday isolator is successfully compensated. The pulse shaper is also used to compensate the phase induced by the coupling objective for all the experiments.

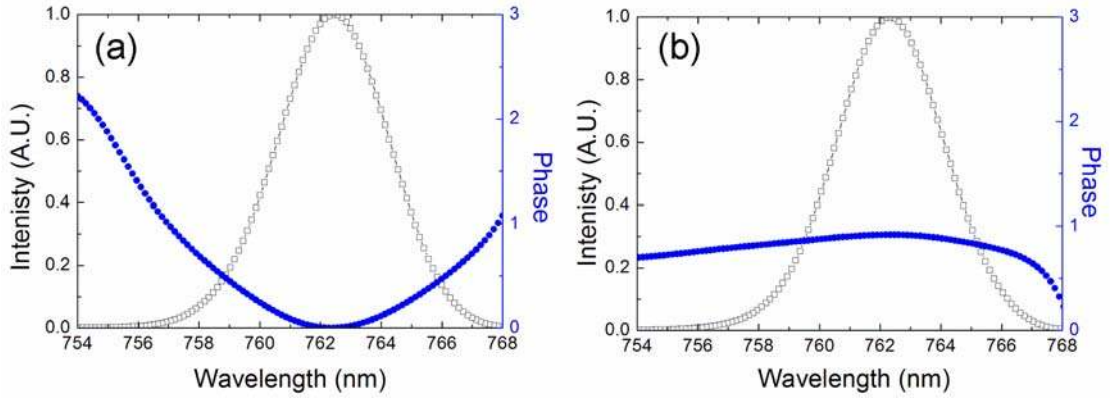

Figure 4.8: SHG FROG measurements of the spectral intensities and spectral phases of the pulses before and after the phase compensation using a pulse shaper. The spectral intensities and phases are shown in white curves and blue curves, respectively. (a) Before the phase compensation, there is a large amount of spectral phase showing in the blue curve. (b) After the phase compensation, a minimal spectral phase indicates a transform-limited pulse.

To conclude this section, we have presented an experimental and theoretical investigation of open loop pulse shaping control of influences of the input pulse quadratic and cubic phase on the supercontinuum generations. When the input pulse is in the anomalous dispersion region of the microstructured fiber, for both input pulse quadratic and cubic spectral phase variations, the transform-limited input pulse generates the supercontinuum with the largest bandwidth. Meanwhile, the input pulse peak power can be used to tune the central wavelength of the generated soliton in this wavelength range.

In addition, the influence of input pulse cubic spectral phase on the supercontinuum generation is investigated when the input pulse central frequency is close to the zero GVD point of the microstructured. Pulse compression due to the interaction between the TOD of the microstructured and input pulse cubic spectral phase with the opposite sign is concluded with the observed supercontinuum bandwidths variation.

4.4 Open Loop Control of Self-Steepening Nonlinear Effect

In this section we present both the experimental and simulation results to show that the self-steepening nonlinear effect in the microstructured fiber can be controlled using pre-shaped temporal ramp pulse. Self-steepening nonlinear effect results from the intensity dependence of the group velocity for the propagating pulse in a way that the high power peak experiences a temporal delay relative to the lower intensity wings. While pulse propagating along the fiber, as shown in figure 2.2 (a), the high intensity

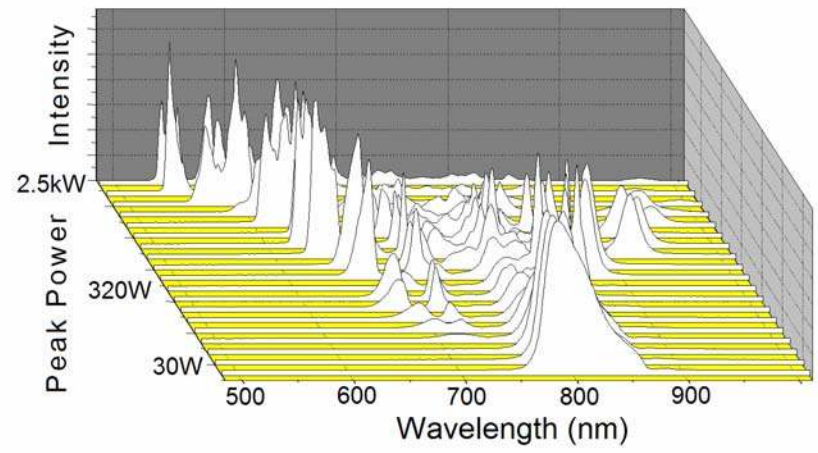

Figure 4.9: Spectral blueshifted asymmetry due to self-steepening. The output spectra are plotted as a function of input pulse peak power.

peak shifts towards the pulse trailing edge, leading to a steepening of the pulse followed by the formation of an optical shock front. An asymmetric blue-shifted spectral

broadening occurs in the frequency domain as the result of interaction between self-phase modulation and self-steepening. As an example, we show the spectral blueshifted asymmetry due to self-steepening nonlinear in figure 4.9, where a dramatically increasing blueshifted asymmetry is shown as the 13 fs input pulse peak intensity shift from 30 W to 2.5 kW.

The parameter governing the self-steepening effect is $s \equiv 1/(\omega_0 \tau_0)$, where ω_0 is the input pulse central angular frequency and τ_0 is the input pulse duration. The distance at which the shock is formed and significant spectral asymmetries can be observed is $z_s = 0.39(L_{NL}/s)$ [3], which is approximately 15 cm for our experimental conditions. For the 70 cm microstructured fiber, both the experimental and simulation results show that the transform-limited pulse experiences severe self-steepening effect and there are large blue-shifted spectral broadenings in the output spectra, as shown in the black curves in figure 4.11 (a) and (b).

To suppress the self-steepening nonlinear effect, it is intuitive to pre-shape the input pulse in such a way that the steepness lies on the leading edge of the input pulse. As this pre-shaped pulse propagates along the microstructured fiber, the forward "ramp" pulse become more symmetric to the pulse center due to the self-steepening effect; therefore, as a result, the blue-shifted spectral broadening asymmetry is suppressed. The input forward "ramp" pulse is synthesized using the phase-only pulse shaper with phase masks synthesized using the Gerchberg-Sexton algorithm [116] and verified by the SHG FROG measurement. Figure 4.10 shows the FROG measurement results, where (a) and (b) are the experimental FROG trace and reconstructed FROG trace, respectively. The FROG error is 0.002, indicating a reliable reconstruction result. The retrieved temporal

intensity and phase of the input forward “ramp” pulse are shown in Figure 4.10 (c). For comparative purposes, we also generate input pulse with backward “ramp”. Note that for both “ramp” pulses and input unshaped transform-limited pulse, the pulse shapes and durations are different. When using pulses shaped via the Gerchberg-Sexton algorithm, the peak intensity of the unshaped transform-limited pulse is attenuated to the same level as that of the “ramp” pulses since supercontinuum generation depends critically on the input pulse peak intensities.

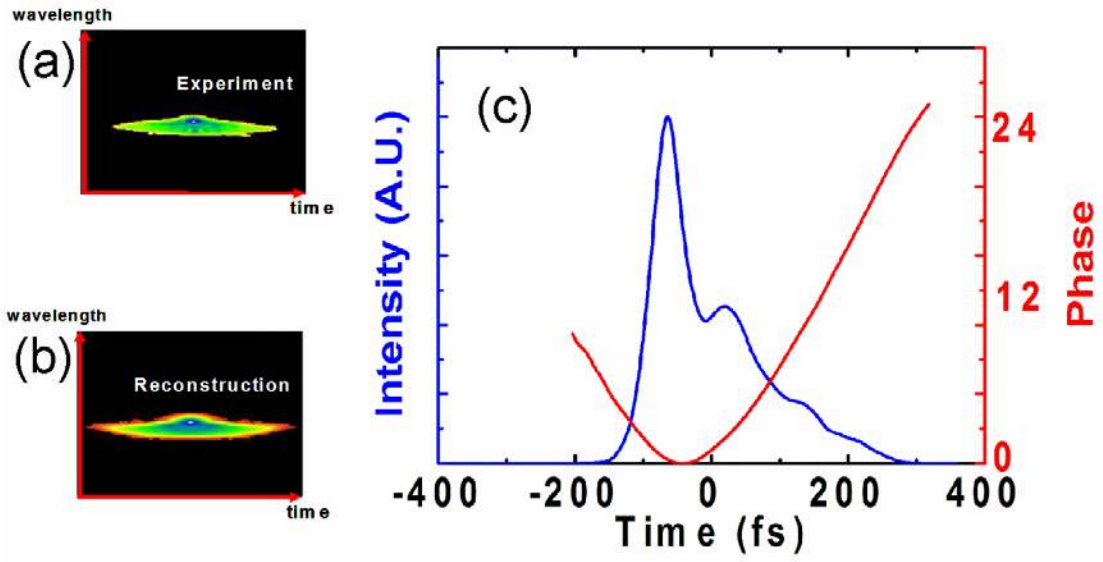

Figure 4.10: SHG FROG measurement results of phase sculpted forward “ramp” pulse generation. (a) and (b), the experimentally measured FROG trace and reconstructed FROG trace, respectively. (c), measured temporal intensity and phase of the forward “ramp” pulse. SHG FROG, second harmonic generation frequency resolved optical gating.

We use the pre-shaped forward “ramp” pulse to suppress the self-steepening and blue shifted spectral broadening effect. The experimentally generated output spectrum from the microstructured fiber corresponding to this pulse is shown as the red curve in figure 4.11 (a). It is evident that the supercontinuum generated by the forward “ramp” pulse is smoother and shows less broadening toward the blue side than that by the

transform-limited symmetric input pulse (output spectrum shown as the black curve in figure 4.11 (a)). Upon recording the phase for generating the forward "ramp" pulse and use it as the input for the NLSE model, we simulate the supercontinuum generation corresponding to this input forward "ramp" pulse. The simulation result shown as the red curve in figure 4.11 (b) is in good agreement with the experimental output spectrum, with a modulation depth of the red and blue-shifted components nearly identical to that observed in the experiment. Meanwhile, simulation results also verify that a smoother output spectrum is generated with more uniform broadening towards both red and blue sides. Note that when the input pulse has the same polarity (backward) "ramp" as the self-steepening formed optical shock, the output spectrum exhibits a similar character to that of the transform-limited pulse, with deep spectral modulation and asymmetric broadening

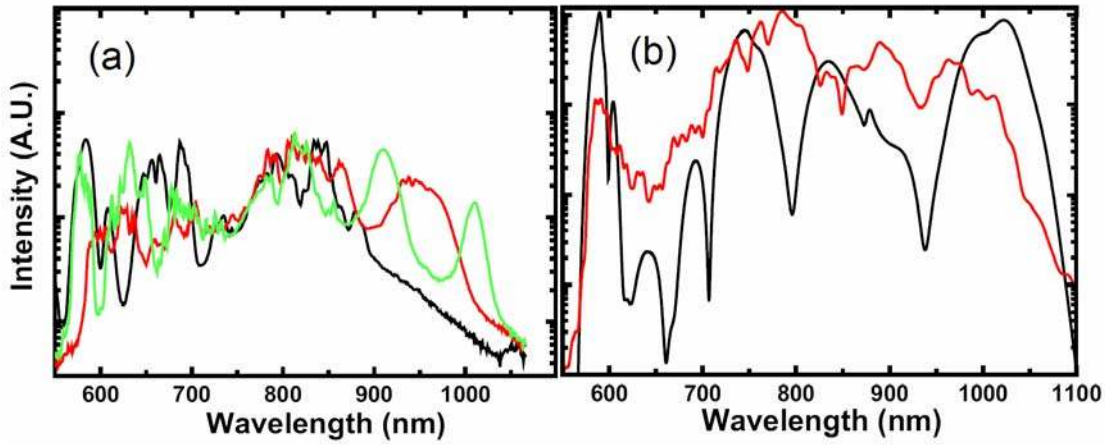

Figure 4.11: Experimental and simulation results of suppression of self-steepening effect using pre-shaped forward ramp pulse. (a) The experimentally observed output spectrum from a 70 cm MSF obtained with a transform-limited pulse (black curve), and forward (red curve) and backward (green curve) "ramp" pulses. (b) NSLE simulation of the supercontinuum from a transform-limited pulse (black curve) and the shaped forward "ramp" pulse (red curve).

toward the blue (shown as the green curve in figure 4.11 (a)). Therefore it is evident that the forward "ramp" pulse shape (not the longer pulse duration) actually performs the suppression of the self-steepening and generates smoother spectral output. Our simulations of the evolutions of the pulse temporal intensity while pulse propagating in the microstructured fiber for the forward and backward "ramp" pulses corroborate this conclusion. The temporal output for the forward "ramp" pulse (figure 4.12 (a)) shows a less structured envelope and trailing edge when compared with the temporal output for the backward "ramp" pulse (figure 4.12 (b)). In addition, the evolutions of the pulse propagation in the fiber for these two input "ramp" pulse indicate the self-steepening nonlinear effect is indeed compressed by introducing the forward "ramp" pulse.

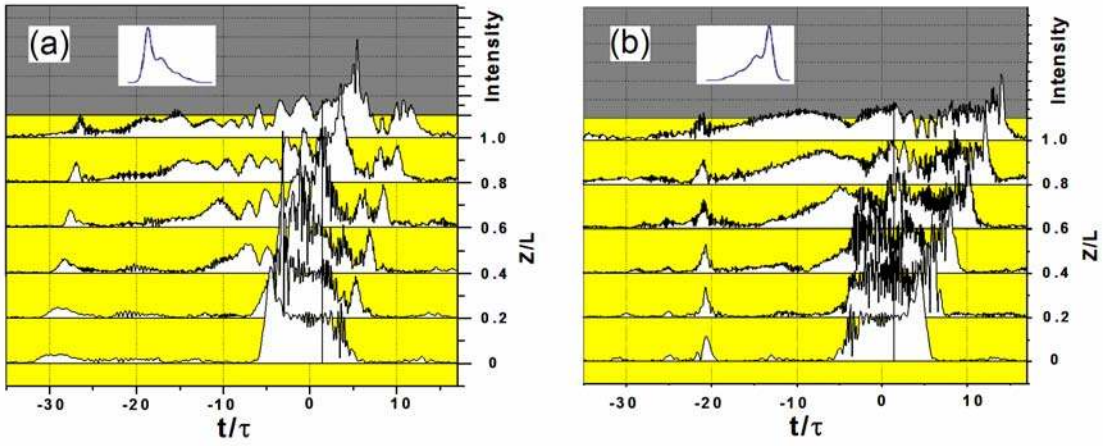

Figure 4.12: Simulation results of the evolutions of the pulse temporal intensities as a function of propagation length in the microstructured fiber for the forward and backward "ramp" pulse. The time scale and propagation length is normalized to the input pulse duration and fiber length, respectively. The insets in the figures are the demonstration of the input "ramp" pulses for clarification purpose. (a) Evolution of the pulse temporal intensities as propagating in the fiber for forward "ramp" pulse. (b) Evolution of the pulse temporal intensities as propagating in the fiber for backward "ramp" pulse.

As a conclusion for this section, we successfully counteract the self-steepening nonlinear effect by intuitively introducing a forward "ramp" pulse. Both the experimental

and simulation result corroborate this conclusion. Therefore the blue-shifted spectral broadening asymmetry due to the self-steepening is also suppressed.

CHAPTER 5
CLOSED LOOP CONTROL OF THE SUPERCONTINUUM GENERATION IN PCFS VIA ADAPTIVE PULSE SHAPING

We have investigated open loop control of the supercontinuum generation in microstructured fibers in the previous chapter. Here we present the results of the closed loop control (adaptive pulse shaping) of supercontinuum generation. In section 5.1, we cover the aspects of closed loop control and give a brief introduction of genetic algorithms, as well as the experimental details of our adaptive pulse shaping method. In section 5.2, an investigation of adaptive pulse shaping enhancement of the supercontinuum spectral broadening will be presented. In addition, we will present the adaptive pulse shaping results of controlling soliton self-frequency shift in section 5.3. In particular, both the magnitude of soliton self-frequency shift and duration of the generated soliton can be fine-tuned within a specified range. Simulation results based on the NLSE elucidating the mechanisms of the optimizations will be discussed in details in both sections.

5.1 Closed Loop Control and Genetic Algorithms

Closed loop control (or adaptive control) methods comprise the other major branch of the control methods [111]. Unlike the open loop control methods, which use as a prerequisite the underlying knowledge to derive proper control pulse, closed loop control methods use system feedback coupled to learning algorithms to efficiently search all the possible control pulses. The process of searching the proper control schematics stops, automatically or manually, when a certain set conditions are met. In controls terminology,

the entire possible set of pulses being searched is called the “parameter space”, while the criterion (or criteria) which account for the control goals (the set of physical parameters to be optimized) is called the “cost function”. The pulse parameters that can be optimized in closed loop control experiments using phase-only shaping include pulse phase (and hence temporal shape), energy, duration, number of pulses, etc... Particularly for the closed loop control of supercontinuum generation in the microstructured fiber, we are going to lay out the results of optimizing the supercontinuum bandwidth and controlling soliton self-frequency shift in this chapter.

A Labview-based data acquisition program based on learning algorithm (genetic algorithm) is build to coordinate the closed loop control schematics and efficiently search the parameter space. The interface is designed so that the evolution of the cost function can be monitored during the optimization process. One can easily tell if the cost function design is appropriate depending on the convergence of the evolution. Besides, the setup of the parameter space, such as the number of the parents and mutation rate (definition see below), can be easily readjust using this interface. More importantly, this Labview-based program allows us to synthesize all the data acquisitions and analysis together; therefore the genetic algorithm can run without any interruption.

Because of the unique properties of closed loop control compared to that of open loop control, there are several general considerations that need to be discussed. Obviously, the intrinsic dynamics of the closed loop control determines that it is a time consuming process compared to the open loop control, due to the potentially large parameter space and the initial conditions, namely that there is no “best” pulse to begin with. Given the advances in the microprocessor technology, closed loop control simulated in a computer

can be extremely fast. However, when implementing the closed loop control in the experimental conditions, the total processing time to find a proper control input is extremely variable, ranging from minutes to days depending on the time for the process loop of individual application. This leads to a prerequisite for the control system that it has to maintain a stable working condition in order for closed loop control schematics to work. Of course with the advances in adaptive control technology, indirect adaptive control or self-tuning adaptive control [117] can implement the predictable system variation into the closed loop control methods. But for the system that cannot maintain a stable working condition or the system variation is unpredictable in a timely manner, closed loop control methods are not well suited. Another important fact for the closed loop control is that the designs of the parameter space and cost function greatly determine if the searching process will be convergent and if, by any means it is convergent, an efficient searching is presented for the loop processes. This brings up the next topic of the closed loop control methods, the selection of a suitable learning algorithm: the genetic algorithm.

A genetic algorithm (GA) is a global optimization technique that mimics paradigms of biological evolution to efficiently search multi-dimensional complex parameter space [118]. The GA starts with a genome (or chromosome) and creates a population of chromosomes (parents). Using genetic operators such as crossover and mutation, new individuals (children) are generated in the parameter space from the original parents and serve as the “trials” in the control schematics. The generated results correspond to each individual child are evaluated by the cost function which calculates the cost value for every trial. Depending on how “good” each individual child is, that is, judging from the

cost values, the GA picks the best children with the number same as the original population of the parents. That finishes the first loop. The best children chosen in this loop will serve as the parents for subsequent genetic operators in the next loop. Genetic operators serve as the functionalities to generate children from the parents. There are many genetic operators available depending on different genome configurations (for example, binary or decimal). The most widely used fundamental genetic operators are "cross-over" and "mutation". The cross-over operates on selected genes from parent chromosomes and creates new offspring. Taking binary chromosome as an example (see table 5.1, cross-over operator), the simplest way to perform cross-over is to randomly choose two chromosomes and cross-over point first, followed by a concatenation of everything before the cross-over point from the first chromosome and everything after the cross-over point from the second chromosome; therefore two offspring are generated after one cross-over operation. More complicated cross-over operator involves two or more randomly selected cross-over points. Choosing cross-over operator configured for

Table 5.1: Illustration of the cross-over operator and mutation operator (binary chromosome).

Cross-over Operator		Mutation Operator	
Chromosome 1	11011 | 00101110110	Offspring 1	1101111000011010
Chromosome 2	00011 | 11000011010	Offspring 2	0001100101110110
Offspring 1	11011 | 11000011010	Child 1	1111111000011010
Offspring 2	00011 | 00101110110	Child 2	0001000101111110

specific closed loop control can improve the performance of the genetic algorithm. The mutation operates on the offspring to generated children. The simplest mutation operator just randomly changes one or more digits of the offspring, as illustrated in table 5.1. Mutation is extremely important for the genetic algorithm because it prevents the

searching algorithm from falling into a local optimum of the parameter space. Meanwhile, GA parameters such as the cross-over rate and mutation rate can greatly affect the efficiency of the searching processes.

The integration of closed loop control using the GA and Fourier domain pulse shaping (namely, adaptive pulse shaping) yields great advantages in the control of various nonlinear processes. Adaptive pulse shaping is very important in the pulse compression application [102, 109] and amplified femtosecond pulse laser [103, 120]. Adaptive can also be used to generate arbitrary femtosecond pulse shape [121]. Some other specific examples of adaptive pulse shaping include enhancement and tuning of the high order harmonics [122], nonlinear broadening [123] and soliton self-frequency shift in conventional fibers [124].

Considering the fact that supercontinuum generation is a nonlinear effect in the extreme, that is, starting with SPM and high order soliton generation and followed by various nonlinear effects that are in a tangled state interacting with each other, control of supercontinuum generation in microstructured fiber is in general difficult. In many cases the optimal driving pulse to achieve desired supercontinuum feathers cannot be generated by intuition, thus open loop control methods are not suitable for these instances. Adaptive pulse shaping technique is then the natural approach when the driving pulses for achieving particular control goals cannot be easily derived. With the proper design of the parameter spaces and cost functions, adaptive pulse shaping using the GA can efficiently derive the desired driving pulse. Since the derivation process is automatically controlled by the GA and the control program, sometimes it is not very clear how the derived driving pulse can achieve a specific control goal in physics. However, one of the primary

goals of the GA control is to learn something about the system from the optimization. After recording each step in an optimization process for the adaptive pulse shaping technique, in particular, the phase patterns that generate the best driving pulses in each loop, one can study these driving pulses as well as use the NLSE simulation model to investigate underlying physics. Our experimental and simulation results discussed in the next several sections enumerate this approach. For the closed loop optimization of the supercontinuum bandwidth, after careful investigations of the driving pulse spectral phase evolution, we conclude that the optimization process generates the right input pulse spectral phase to compensate the fiber dispersion effect; therefore generating a broader supercontinuum. For the adaptive control of soliton self-frequency shift, by feeding the experimentally determined input driving pulse spectral phase into the NLSE simulation model and studding the soliton generation process, we conclude that the pulse shaper acts as a sensitive amplitude filter to generate the accurate input pulse peak power; therefore performing a control of both the magnitude of the soliton self-frequency shift and soliton duration.

Based on this brief introduction of closed loop control and the GA, it is easy to deduce and understand how pulse shaper can be used in the closed loop control to manipulate the pulse nonlinear propagation in the microstructured fibers. The adaptive pulse shaping schematic is shown in figure 5.1. For each loop, there are many groups of phase generated in the parameter space by genetic operators. Population size, which is defined as total chromosomes numbers for each generation, is another parameter for GA. If there are too few chromosomes, the GA has few possibilities for performing the cross-over operation and only a limited parameter space is explored. If the population size is

too large, the GA slows down. Choosing an appropriate population size depending on different types of phase parameterization is critical to the search algorithm. We used 7-bit phase parameterization for the adaptive control experiment, which corresponds to 128 possible pulse phases for each generation. All these groups of phases are sent to the pulse shaper to generate driving pulses with different intensity temporal profiles. Supercontinua generated by the microstructured fiber are collected by spectrometer for each driving pulse and analyzed by the GA. The GA uses user-defined cost function to evaluate the continua and locate the phase groups that attached to the optimal driving pulses. These phase groups are then sent to the next loop and serve as the parents for next generation.

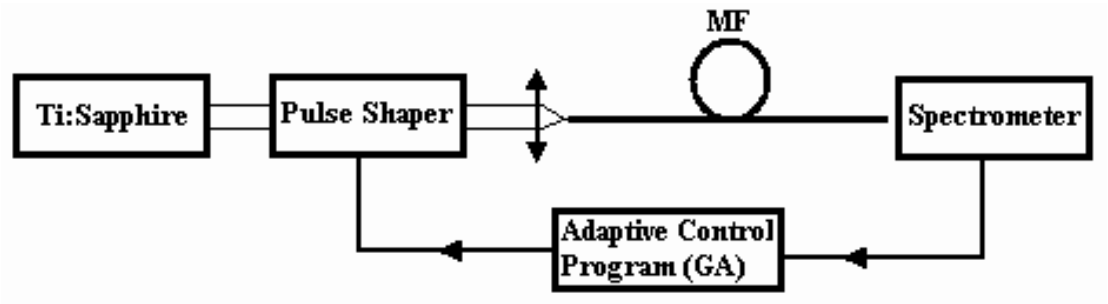

Figure 5.1: Schematic diagram of the closed loop control (adaptive pulse shaping) experiment. MF: Microstructured fiber. GA: Genetic algorithm.

In the closed loop control experiments discussed in this chapter, we use the Ti:Sapphire laser system that generates 800 nm, 3 nJ and 30 fs laser pulses as the input for the adaptive pulse shaping experiment. A 70 cm microstructured fiber is used for the supercontinuum generation experiment.

5.2 Enhancement of Spectral Broadening via Adaptive Pulse Shaping

The supercontinuum bandwidth is very important for many applications. For example, supercontinuum generation in the microstructured fiber has applications in the optical imaging [62-64], where its longitudinal resolution in a biological tissue is inversely proportional to the bandwidth of the light source. Submicron axial resolution in

the optical coherent tomography has been achieved utilizing the extreme wide bandwidth of the supercontinuum [125]. High precision optical metrology requires the bandwidth of the supercontinuum large enough (over one octave) in order to measure the absolute frequencies of the comb structures [67]. Laser based precision spectroscopy based on the optical frequency comb technique promises to revolutionize high precision spectroscopy and is one of the subjects of Nobel Prize in Physics in 2005 [8]. Supercontinuum generation yields great advantage in measure the absolute frequencies of the optical frequency comb, where the frequency displacement can be determined by measuring the beat signal between the high frequency and frequency doubled low frequency component [8]. In addition, the telecommunication applications require a supercontinuum coherent source with a large bandwidth to generate over 1000 dense-wavelength-division-multiplexing (DWDM) channels [21].

We investigate how closed loop control using adaptive pulse shaping can be used to increase the bandwidth of the supercontinuum generations in microstructured fibers. In this adaptive pulse shaping experiment, Taylor series coefficients of the input pulse spectral phase up to the 5th order:

$$\phi(\omega) = \phi^{(1)}(\omega-\omega_0) + \frac{\phi^{(2)}}{2}(\omega-\omega_0)^2 + \frac{\phi^{(3)}}{6}(\omega-\omega_0)^3 + \frac{\phi^{(4)}}{24}(\omega-\omega_0)^4 + \frac{\phi^{(5)}}{120}(\omega-\omega_0)^5 \quad (5.1)$$

are selected as the parameter space for the GA, with 7-bit (2^7=128) parameterization for each coefficient in the Taylor series expansions. Since the control goal is to maximize the bandwidth of the supercontinuum, the cost function is calculated as the integration of the spectral intensity in both ends of the supercontinuum generation. Assuming a transform-limited input pulse, the blue end and red end of the supercontinuum are in the range of

500-570 nm and 950-1020 nm, respectively. Therefore, the cost function is defined as the integrated spectrum in these regions:

$$J = \int_{500nm}^{570nm} I(\lambda)d\lambda + \int_{950nm}^{1020nm} I(\lambda)d\lambda \tag{5.2}$$

The optimization process starts with a transform-limited input pulse as the driving pulse (genome); this ensures that any improvement from this start point will be a nontrivial optimization, i.e., any change of the input pulse that generates a broader supercontinuum is more complicated than that of the transform-limited pulse. Figure 5.2 (a) shows the evolution of the cost function value (achievement) during the optimization. It is evident that the spectral density in the target spectral ranges of the supercontinuum is increased, as the achievement is nearly doubled during the optimization processes. After

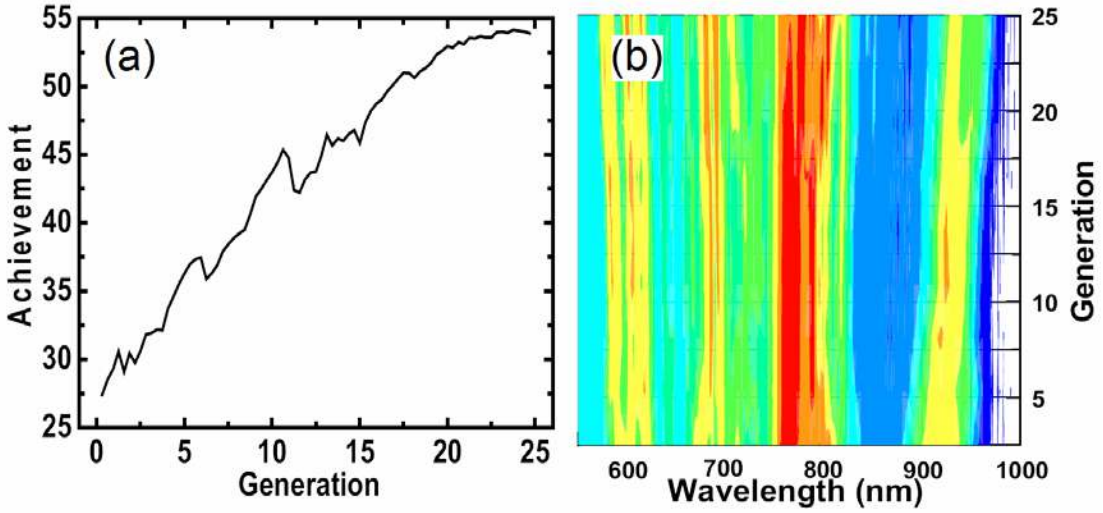

Figure 5.2: Experimental results of closed loop control of optimization of supercontinuum generation bandwidth. (a) The improved achievement (cost function value) as a function of generation index. (b) The experimentally observed evolution of the output spectrum, showing increased bandwidth as the optimization progresses.

approximately 20 generations, the optimization begins to stagnate. The evolution of the supercontinuum spectrum is shown in figure 5.2 (b), with over 10% increase of the output spectra bandwidth during the optimizations.

Since the optimization starts from a transform-limited driving pulse, any improvement of the supercontinuum generation bandwidth should correspond to a true enhancement of the nonlinear interactions in the microstructured fiber caused by changing the input driving pulse properties. After the optimization, the supercontinuum generation bandwidth increases by 10% and the cost function value that designates the integrated spectral intensity in the selected optimization bands increases by a factor of 2.

As noted above, it is important to examine the evolution and resulting optimized driving pulse to try to clarify *how* the adaptive pulse shaping using GA educes the optimized input driving pulse that enhances the nonlinear interactions in the microstructured fiber. Upon recording the driving pulse spectral phases of which yield the maximum cost value (supercontinuum bandwidth) in each generation, we are able to exam the evolution of spectral phase pattern and clarify the mechanism leading to the optimization process. As we can see from figure 5.3, the phase pattern evolves visibly during the first two generations, accompanied by only slight changes for the rest optimization processes. In the open loop control experiment discussed in the previous chapter, we observed broadening of the output spectrum when introducing a negative input pulse cubic spectral phase that later being compensated by the TOD of the microstructured fiber. As the result of the open loop control experiment, the input pulse experiences compression when start propagating along the fiber; therefore generating a broader supercontinuum comparing to the input pulse without addition spectral cubic phase. Following this elucidation, we conclude that during the optimization GA is able to generate the driving pulse with the optimized spectral phase that interacts with the all orders of fiber dispersion. The optimal driving pulse experiences compression when

starting propagating along the fiber; therefore generating higher peak intensity and increasing the magnitude of the following nonlinear interactions. As a result, the achievement increases by a factor of 2. This conclusion is consistent with evolution of the recorded input pulse spectral phase pattern. The visible change of the pulse spectral phase pattern at the beginning of the optimization corresponds to the generation of the second order spectral phase in order for the input pulse to compress as a result of interaction with the second order dispersion of the microstructrued fiber. Further in the optimization process, the higher order dispersions of the fiber are compensated because of the continuously broadened supercontinuum generation accompanied with only slight variations of the input pulse spectral phase pattern.

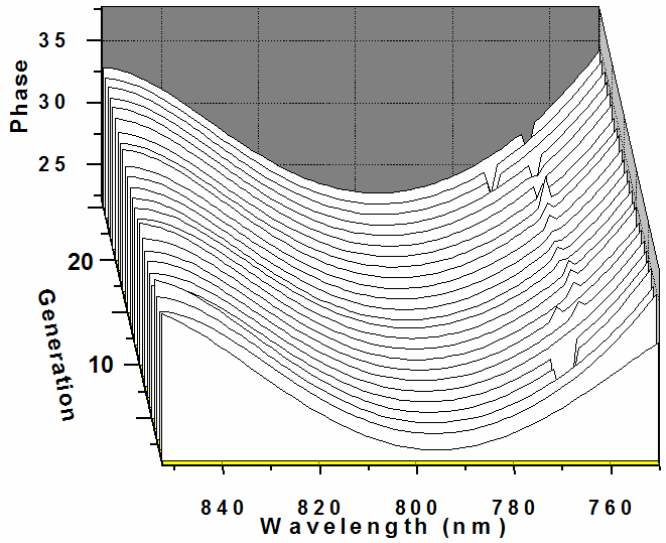

Figure 5.3: Evolutions of phase pattern for adaptive pulse shaping experiment of supercontinuum bandwidth enhancement.

Finally, we use this adaptive pulse shaping experiment as an example to illustrate several considerations relevant to the adaptive control method. We have found that the design of the parameter space in the implementation of the GA greatly influences the performance of the adaptive pulse shaping, in particular, the speed and efficacy of the

convergence. In fact, we first select the intuitive parameter space for the adaptive pulse shaping experiment, namely a random parameter space, i.e., starting from a random phase value for the input driving pulse at every SLM pixel in the pulse shaper. However, this intuitive parameter space was found to be ineffective. Even with a sufficient large number of genomes (parents) and individuals (children), supercontinuum generation is rather inefficient due to the randomization of the parameter space. For the entire optimization process for a reasonable period of time (for example, several hours), the output continuum is even narrower than that for the transform limited input pulse due to the randomized phase parameter space. Therefore we select a parameter space that utilizing the Taylor expansion coefficients of the input pulse spectral phase and successfully perform the adaptive pulse shaping experiment of the supercontinuum broadening. In this case, the optimization process starts from a near transform limited pulse which insures that any improvement will be a nontrivial case comparing to the starting point. The other consideration of the adaptive control schematics is the system stability during the optimization process, i.e., the stability of the laser system used in the experiment. For example, the temperature fluctuation and other perturbations can break the laser mode-locking schematics during the optimization process and laser beam-pointing instability [126] can substantially change the pulse peak intensities that coupled into the front end of the microstructured fibers. In order to by pass these instabilities and "virtually" maintain the stable system conditions, we record all the parameters for each loop, including all the data (parents, children and cost values) in the GA. After the system is back online and working in a stable condition, the adaptive pulse shaping can be

resumed by recollection of all the recorded parameters in the GA. This allows us to carry out our experiments over times ranging from one to ten hours or more.

5.3 Adaptive Control of Soliton Self-Frequency Shift

Soliton generation is the result of interplay between the SPM nonlinear effect and anomalous dispersion. Soliton self-frequency shifts (SSFS) following the soliton fission is also responsible for the initiation of the supercontinuum generation [10, 11]. Besides, much research has been done on the SSFS in the microstructured fiber in the past few years. Specific examples include investigations of SSFS effect in the PCFs [127, 128], SSFS cancellation in the PCFs [129], SSFS effect in dispersion engineered fiber [18] and 10 GHz soliton pulse generator using SSFS in PCFs [130]. Recent work done by Efimov et al. show that it is possible to stabilize the soliton propagation in the conventional fiber using adaptive pulse shaping [124].

As another example of closed loop control experiment, we investigate how the adaptive pulse shaping can be used to control the soliton self-frequency shift, in particular, simultaneously control the magnitude of the self-frequency shift and the duration of the shifted soliton. To our knowledge, this is the first time that adaptive pulse shaping is used for controlling SSFS in the microstructured fiber.

A randomized parameter space is used, i.e., each of the 128 elements in the pulse shaper SLM is allowed to vary in the range $0-2\pi$ with 8 bit resolution. The cost value is defined as a comparison value in the frequency domain between the experimental generated soliton and the target Gaussian-shaped soliton of specified width at a particular wavelength,

$$J = W_\lambda \exp\left[-\left(\frac{\lambda - \lambda_{target}}{\sigma_\lambda}\right)^2\right] + \frac{W_{\Delta\lambda}}{1+\left(\frac{\Delta\lambda - \Delta\lambda_{target}}{\sigma_{\Delta\lambda}}\right)^2} \tag{5.3}$$

where the value of J represents the cost value. In this equation, the first part of the right hand side stands for the wavelength comparison contribution and the second part stands for the soliton width comparison contribution. The σ terms in each denominator determine the fitting tolerance to a target soliton and the W coefficient provides weights for each of the target criteria. λ_{target} and $\Delta\lambda_{target}$ represents the target soliton position and target soliton width, respectively. λ and $\Delta\lambda$ represents the soliton position and width for experimentally generated soliton. Note that the generated soliton central wavelength corresponds to the control of the magnitude of soliton self-frequency and the soliton width in the frequency domain corresponds to the duration of the shifted soliton in the time domain.

Figure 5.4 (a) and (b) shows the output spectra with experimentally generated target solitons specified at different wavelengths and with different soliton widths, respectively. In figure 5.4 (a), three soliton are generated with a fixed width of 15 nm at three wavelengths, 900 nm, 925 nm and 950 nm. In each soliton generation case, the wavelength difference between the generated soliton and target soliton is less than 1 nm, indicating essentially 100% achievement. In addition, blueshifted nonsolitonic components that satisfy the phase-matching condition are observed in the output spectra. The second set of closed loop control experimental results shown in figure 5.4 (b) demonstrate that solitons can be generated at a fixed central wavelength of 925 nm with different soliton widths range from 15nm to 54 nm. Note that in the widest soliton generation case (green curve in figure 5.4 (b)), the spectral signature indicates that a

higher order soliton is undergoing a fission process into two fundamental solitons. To determine the region of central wavelength and width that the randomized parameter space can successfully access in the adaptive pulse shaping experiment, we performed a series control experiments for the soliton generations with different target parameters, i.e., different combinations of soliton widths and soliton central positions. In the experimentally determined control range, a fundamental soliton can be generated and tuned continuously from 900 nm to 950 nm with a bandwidth range of 10 nm to 40 nm. The bandwidth range of the generated soliton corresponds to soliton durations ranging from 22 fs to 90 fs. The adaptive pulse shaping is unable to achieve the targeted states outside of these ranges.

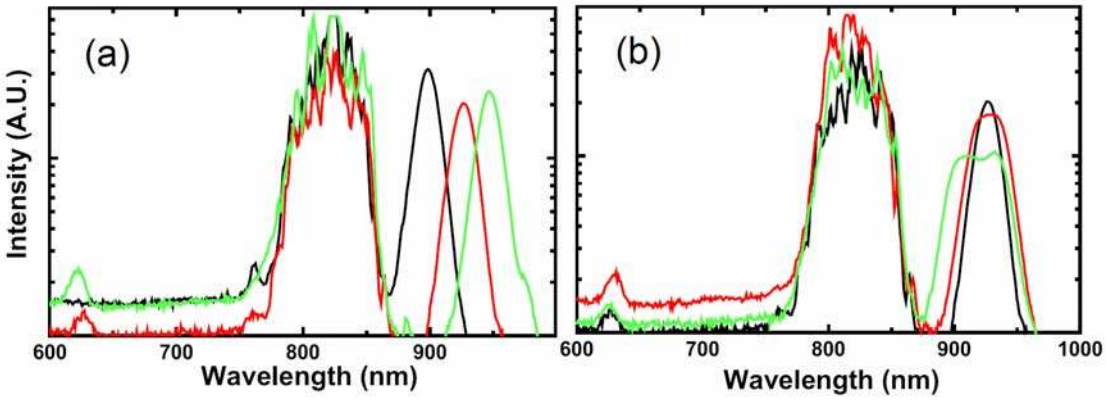

Figure 5.4: Experimental results of closed loop control of soliton self-frequency shift. (a) Three soliton generations with different central wavelengths and a fixed width. (b) Three soliton generations with a fixed central wavelength and different widths.

The experiment discussed in this section is an excellent demonstration on how the adaptive pulse shaping with the GA can be used to control the extremely complex nonlinear interactions in the microstructured fibers; in particular, the GA is able to synthesize the input driving pulse by efficiently searching a randomized parameter space and perform the control of soliton self-frequency shift. Again, we examine the inevitable

question for the closed loop control experiment: what is the physics behind the optimization and why the optimization works? Note that we use a randomized parameter space in this adaptive pulse shaping experiment, the intrinsic "random" property practically makes the interpolation of the driving pulse functionality much more difficult.

To answer the previous question, we carefully exam the driving pulse that target the soliton self-frequency shift with 15 nm width at 925 nm central wavelength (output spectrum shown in red curve in figure 5.4 (a)). The experimentally determined driving pulse in frequency domain and time domain are shown in figure 5.5 (a) and (b), respectively, with the intensity profiles shown in red curves and phase profiles shown in blue curves. Unsurprisingly, the spectral phase of the input driving pulse that is responsible for optimized soliton generation is quite complex (blue curve, figure 5.5 (a)),

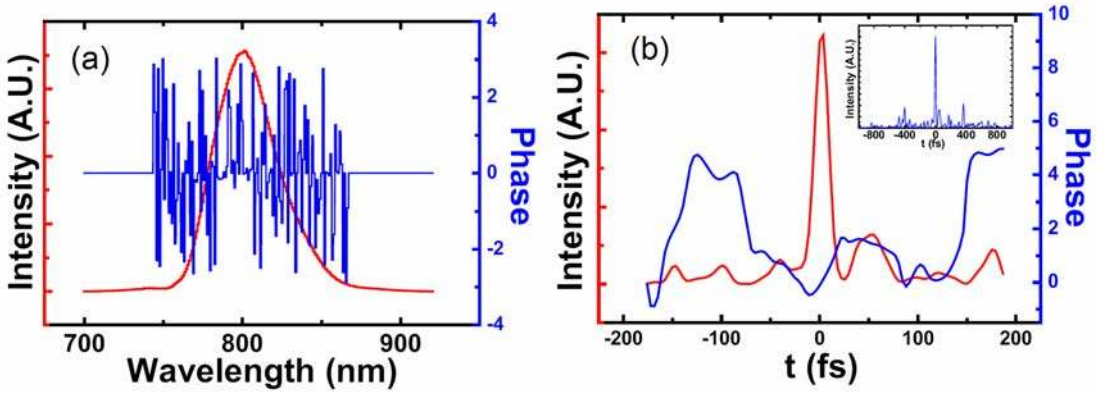

Figure 5.5: An example of the experimentally determined input driving pulse in the frequency domain and time domain. The driving pulse is for soliton generation at 925 nm with a 15 nm bandwidth. (a) The spectral intensity and phase of the driving pulse. (b) The temporal intensity and phase of the driving pulse. Inset: temporal intensity on a larger time scale.

as evidenced by the lack of smoothness and series of discrete phase jump from pixel to pixel. The resulted temporal intensity and phase of the driving pulse are shown in figure 5.5 (b). The temporal intensity structures resemble a "noise burst", with an ultrashort coherent feather embedding in a longer series of pulses with much lower random

intensities and irregular temporal spacing. The temporal intensity is shown in a larger time scale in the inset figure. It is evident that the pulse energy is distributed over a much larger time scale compare to that of a transform-limited pulse, with the main portion of the pulse energy lies in the central ultrashort coherent feather. Therefore the peak intensity of the coherent feature is lower than that of the transform-limited pulse. Interestingly, the pulse shaper which is designed for phase shaping only acts as a highly sensitive amplitude filter in this experiment, which is not quite surprising since a straight-forward inverse Fourier transform from the frequency domain with randomized spectral phase structures can evidently yield variation of the pulse peak intensity in the time domain. Recall the open loop control experiments we discussed in the previous chapter that demonstrate the pulse peak intensity variation due to the modifications of the input pulse spectral phase can evidently perform a control of the soliton self-frequency shift magnitude. Especially for the case of the modifications of the input pulse cubic spectral phase, where in that experiment the magnitude of the cubic spectral phase variation only change the pulse peak intensity by a relative small amount (figure 4.2 (a)), we observe the sensitive control over the central wavelengths of soliton generation (figure 4.3 (b)). Based on this observation and previous discussion on the input driving pulse central coherent feature, we simulate the soliton generation positions as a function of pulse input peak pulse with other customized and fixed input pulse parameters. As shown in figure 5.6 (a), the central wavelengths of the simulated soliton generations shift towards long wavelength side of the output spectra continuously with the increase of the input pulse peak intensity. As for this specific configuration, the soliton position shifts from 920 nm to 945 nm when the input pulse peak intensity change from 8 kW to 30 kW.

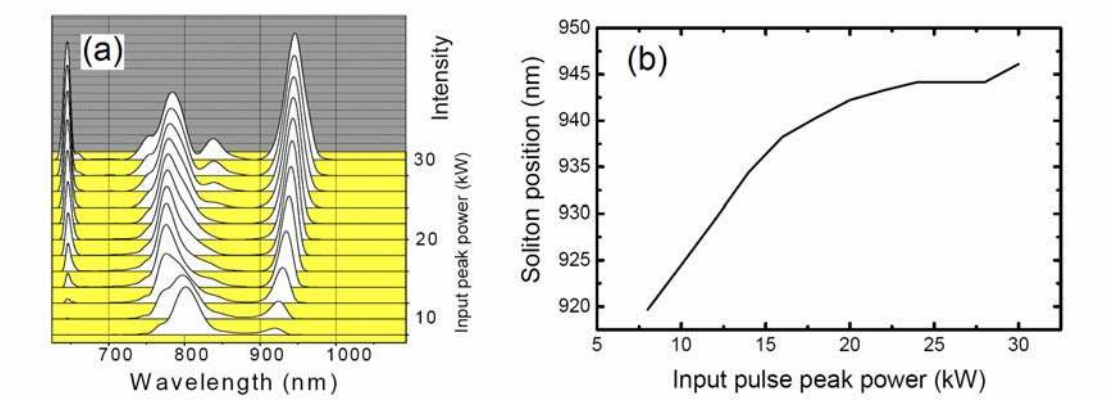

Figure 5.6: Simulation results of soliton central wavelength as a function of input pulse peak intensity. (a) Output spectra as a function of input pulse peak intensity. (b) Specified soliton generation at different central wavelengths with input pulse peak intensity variations.

Therefore, we conclude for the mechanism of the optimized driving pulse generating a target soliton that satisfies two criteria that the phase-only pulse shaper acts as a very sensitive amplitude filter by introducing a rather "random" spectral phase pattern and the driving pulse with precisely tuned peak intensity performs the control over the soliton self-frequency shift.

Using the experimentally determined driving pulse temporal intensity and phase, we simulate the soliton self-frequency shift with the extended NLSE model. Once again, as shown in figure 5.7, the simulation result (red curve) faithfully reproduces the experimental result (blue curve), although the simulated soliton shifts slightly to the red side. Upon examination of the pulse propagation in the microstructured fiber using the simulation model, the spectral feather begins to show modulation structures after propagating 20 cm of fiber length, as the similar modulation pattern can be seen from the 800 nm spectral peak for the simulation result in figure 5.7. The soliton separates from the 800 nm spectral peak around 35 cm of propagation length and almost reach the final target position at 55 cm. In the time domain, the soliton self-frequency shift is illustrated

by the temporal broadening of the central coherent feather accompanied by the coherent beating between the target soliton and its phase-matching nonsolitonic component.

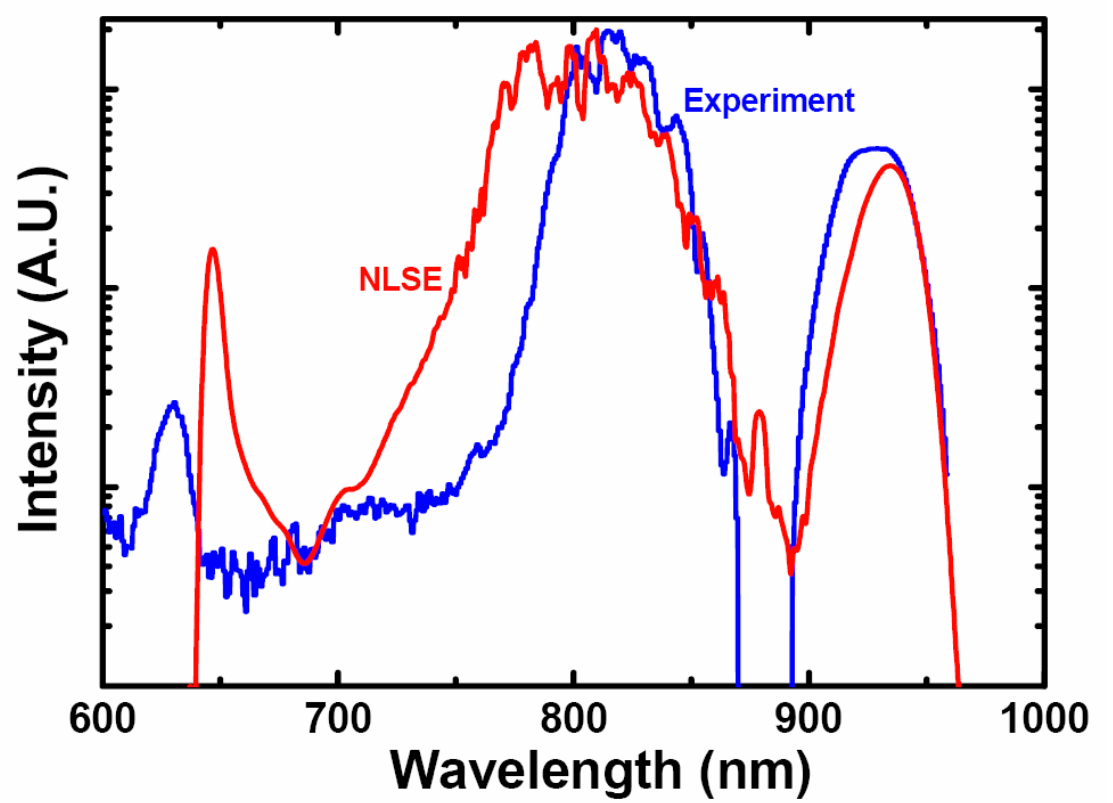

Figure 5.7: Spectra comparison of experimentally optimized soliton generation and simulated soliton using experimentally determined driving input pulse.

In this adaptive control experiment, the positions and durations of the experimentally generated solitons can be fine-tuned within the specified range. Considering the control of the input driving pulse features in the time domain, the pulse shaper acts as a sensitive amplitude filter to precisely control the intensity of central coherent spike and the energy distribution between this main peak and the random "noise" on each side. The driving pulse spectral phase, however, is rather a "random" pattern at a glance. To gain the insight on how sensitive the amplitude filter is, that is, to which degree the "random" spectral phase perform the control of target soliton generation, we intentionally scramble the "random" phase. By altering 10% of the spectral phase

pixels a π phase jump, there is a measurable shift of 30 nm for the target soliton generation, as evidently shown in figure 5.8. Therefore, the stability of the soliton self-frequency shift to the driving pulse is somewhat fragile.

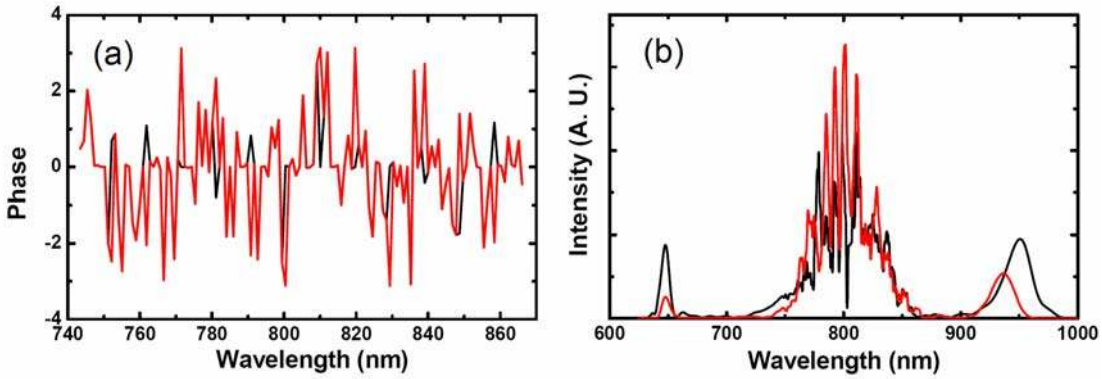

Figure 5.8: Simulation results of the sensitivity of soliton generation to the input driving pulse fluctuation. (a) Driving pulse phase pattern before (red curve) and after (black curve) 10% π phase jump. (b) The simulated output spectra for the soliton generations corresponding to the phase pattern shown in (a), red and black curves, respectively.

In the simulation processes of soliton self-frequency shift, we come across a very interesting observation. The simulated soliton generation position is also dependent on the microstructured fiber dispersion parameters. As shown in figure 5.9, changing the fiber TOD parameter β_3 only influences the position of the blue phase-matching nonsolitonic component, whereas changing the second order dispersion β_2 and the fourth order dispersion β_4 affect both the soliton position and the phase-matching component. By comparing the experimentally generated soliton position with these simulation results, we are able to independently determine the dispersive properties of the microstructured fiber. We find out that the best agreement with the experimental results occur for $\beta_2 = -4.579\, ps^2/km$, $\beta_3 = -1.725\times10^{-2}\, ps^3/km$ and $\beta_4 = 3.178\times10^{-4}\, ps^4/km$, which

is in reasonable agreement with the literature values listed in table 4.1 considering the current 800 nm input central wavelength.

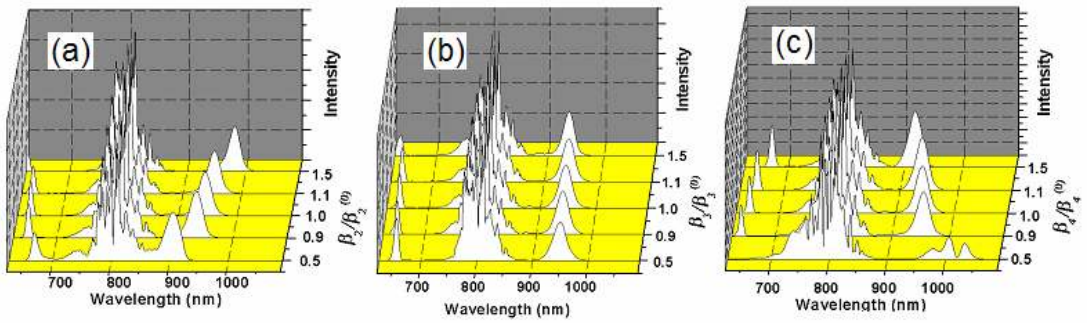

Figure 5.9: Simulation investigation of the sensitivity of soliton self-frequency shift to the fiber dispersion properties. (a), (b) and (c) are for fiber second, third and fourth order dispersion, respectively. Note that $\beta_i^{(0)}$ (i=2,3,4) stands for the original fiber dispersion parameter.

To conclude, we have successfully controlled the magnitude of the soliton self-frequency shift (central wavelength) and the duration of the shifted soliton (width) using adaptive pulse shaping. Both soliton generation parameters can be tuned within the specified control ranges. After carefully examining the optimized driving pulse profiles and using the NLSE simulation model to simulate the target soliton generations, we find the underlying mechanism responsible for the optimization of the soliton self-frequency shift. The phase-only pulse shaper is acting as a sensitive amplitude filter for the driving pulse by introducing an optimized "random" spectral phase pattern. The target soliton generation is the result of the precisely controlled temporal central coherent feather of the optimized driving pulse.

Finally, we use this adaptive pulse shaping experiment as an example to illustrate another aspect of closed loop control methods, that is, the design considerations of the cost function to achieve multiple control goals. In fact, the success of this adaptive pulse shaping experiment is closely related to the design of the cost function. As one can see

from equation 5.2, in order to simultaneously control the central wavelength and the duration of the shifted soliton width, we implement several ingenuities in the design of the cost function. The weight parameter for each of the target criteria can yield the preference of one control goal over the other. The configurations of tolerance parameter advance the searching standard by tightly control one or both target criteria. Meanwhile, the design of the individual functions, i.e., reciprocal function and exponential function, yields another advantage on the searching efficiency. The cost function design critically determines the performance of the closed loop control experiment. In order to gain the ability of achieving multiple control goals using only one cost function, considering the example discussed above will be very helpful.

CHAPTER 6
ROUTES TO PULSE COMPRESSION USING DISPERSION-FLATTENED MICROSTRUCTURED FIBER: SIMULATIONS USING THE NONLINEAR SCHRODINGER EQUATION

6.1 Motivation and Overview of Pulse Compression

As we have shown in the previous chapters, control of supercontinuum generation is possible using shaped optical pulses. Up until this point, we have considered "control knobs" available through shaping of the input pulse. Here, we consider how the dispersive properties of the fiber can be manipulated to control the output spectrum. In particular, our goal in this chapter is to investigate how the exact character of the dispersion in PCFs can be used to produce smooth supercontinuum spectra for pulse compression.

Pulse compression can broadly be described in two stages: first, the creation of sufficient bandwidth is performed through the pulse generation and any subsequent nonlinear interactions which further broaden the spectrum. Second, the residual higher order phase is removed via pulse compression techniques. Given a coherent frequency spectrum with some residual spectral phase, pulse compression can be considered theoretically through one simple Fourier transformation: given a fixed spectral shape, the pulse duration is the temporally shortest only if the pulse is transform-limited (no frequency chirp). In fact, the simulation results described in figure 4.3 in chapter 4 have illustrated this point by showing a larger pulse spectral phase subsequently leads to a lower temporal pulse peak intensity, which is equivalent to a longer pulse duration given fixed pulse energy. Meanwhile, compression of a pulse with broader bandwidth is

equivalent to generating a shorter pulse, which results directly from the time-bandwidth product constant described in chapter 2. After broadband coherent pulses are generated, pulse compression is commonly carried out by accurate measurements of pulse frequency chirps (dispersion), followed by proper dispersion compensation via a grating pair, chirped mirrors, or other means.

Optical fibers, by confining high intensity laser pulses in a small core area and subsequent nonlinear interactions, have become a natural candidate to generate broadband coherent pulses. Continuum generations in conventional fibers have been studied over three decades. Single-mode conventional fibers have relative low nonlinearities and high dispersions in the near infrared and visible wavelength region. Although a record of 6 femtoseconds is generated using a single-mode conventional fiber, a copper-vapor laser-pumped amplifier was used and the nonlinear broadening mechanism was dominated by the self-phase modulation, limiting the amount of spectral bandwidth [131]. Later on, hollow cylindrical fibers made of fused silica and filled with high pressure noble gases are used to perform pulse spectral broadening [132, 133]. The advantages of higher input pulse threshold intensity (for certain noble gases) and controllability of nonlinear strength for different gas type and pressure made them particularly interesting for compression of high energy laser pulses. As results, compressed pulses of 3.8 fs and 3.4 fs have been generated with two cascaded hollow fibers and a single argon-filled hollow fiber with 15 μJ and 94 μJ input pulse energy [119, 16]. However, all these demonstrations for the hollow fibers require amplified laser input pulses and self-phase modulation is mainly responsible for pulse nonlinear broadening. With the advent of photonic crystal fibers (particularly microstructured fibers),

ultrabroadband supercontinuum generation can be easily achieved in the laboratory by Ti:Sapphire femtosecond laser pulses with only nJ pulse energy. The extremely high nonlinearities of microstructured fibers lead to spatially coherent and over-an-octave-spanning supercontinuum with pulses without any pre-amplifications [6]. Such an enormous bandwidth of the supercontinuum generation can potentially lead to single-cycle pulse generation. Meanwhile, hollow PCFs (with air cores) can self-compress extremely high intensity (above 100 MW) femtosecond laser pulses due to the waveguide contribution [134].

One of the most important requisites for the pulse compression is an accurate measurement of the pulse spectral phase. The spectral phase of a broadband pulse can be measured using the FROG and SPIDER pulse characterization techniques described in chapter 2. Meanwhile, pulse compression also requires proper phase compensation. Various phase compensation techniques have been developed, such as prism-pair used in our home-build Ti:Sapphire laser system, grating-pair that usually being used in chirped pulse amplifier system, and dielectric chirped mirrors [135, 136]. However, these techniques provide limited phase compensation abilities and mainly can only compensate linear pulse chirp. Also, different dispersion compensation usually requires carefully realignment. For very broadband pulses, phase compensation can be carried out by Fourier domain pulse shaping, e.g., programmable pulse shaper using LC-SLM. An overview of Fourier domain pulse shaping is given in chapter 2.

Recently, researchers have shown great interest in pulse compression based on the supercontinuum generations in microstructured fibers because the coherent bandwidth exceed 1000 nm. However, what seems like a simple idea in principle turns out to be an

extremely nontrivial problem in reality. In 2002, both the simulation results for the supercontinuum generation based on the extended nonlinear Schrödinger equation model and experimental measurements of the retrieved continuum spectral fine structure and spectral phase using XFROG (cross FROG) show that supercontinuum sub-nm fine structures are extremely sensitive to the input pulse power fluctuations [9, 13]. Simulations show that even with 0.1% input pulse power variation, fine structures of the supercontinuum generation change dramatically. Simultaneously, Dudley's simulation results utilize a coherent function to quantitatively study the supercontinuum coherence variations as a function of fiber propagation lengths, input pulse durations and input pulse wavelengths [137]. Later on, simulation results specifically targeting the supercontinuum compressibility show that there exists an optimum compressed distance at which compressed pulses with negligible fluctuation and time shift can be obtained [15]. The propagation fiber length for optimum supercontinuum compression is a few centimeters. Finally, Dudley and Coen considered generalized fundamental limits of pulse compression to few-cycle region based on supercontinuum generation in microstructured fibers [14]. Unsurprisingly, almost all the research results discussing the supercontinuum compressibility are based on the simulation results, which mainly based on the nonlinear Schrödinger equations model in either frequency or time domain. It is now a consensus that the main nonlinear spectral broadening for the supercontinuum generation is happening during the first few centimeters or even millimeters of the microstructured fiber length. After that point, pulse peak power drops quite a lot and the fiber dispersion effects begin to dominate the propagation dynamics. As a result, sub-nm modulation structures show up in the continuum intensity envelope and subsequently are very

sensitive to the input pulse noise. Meanwhile, pulse compressibility for supercontinuum generation is preferable of short input pulse duration and supercontinuum generations are more stable when the input pulse center frequency is in the microstructured fiber normal dispersion region. Evidently all the pulse compression experiments based on the supercontinuum generation use short femtosecond input pulse and microstructured fiber lengths are usually several millimeters. For example, 6.8 fs pulse duration is achieved by compressing supercontinuum generated in 3 mm of microstructured with Ti:Sapphire laser 12 fs input pulses [138]. In addition, 5.5 fs compression pulse is generated using 15 fs Ti:Sapphire laser and 5 mm microstructured fiber [17]. Although the nonlinear mechanism responsible for the supercontinuum generation in these two experiments is still mainly self-phase modulation, broad band continua are generated using only nJ low pulse energy from Ti:Sapphire lasers; this is evidently benefiting from the high nonlinearities of the microstructured fibers. Recently, when launching the input pulse in the anomalous dispersion region of the microstructured fiber (zero GVD wavelength 744 nm), sub-5-fs pulse compression is achieved using a 12 fs Ti:Sapphire laser centered at 800 nm [139]. Finally, it is worth mentioning that the nonlinearity itself in the photonic nanowire generated from the microstructured fiber also gives another way to directly perform the pulse compression. This is based on the soliton effects discussed in chapter 2 that higher order solitons tends to self-compress within the soliton period. By carefully design the fiber length that corresponds to the soliton self-compress distance, 6.8 fs compressed pulse is directly generated from the photonic nanowire with 70 fs input pulse [140]. Despite all the instabilities related to the supercontinuum generation in the microstructured fiber, the pulse compression application results are quite inspiring.

In fact, all the pulse compression experiments use adaptive pulse shaping based on the Fourier domain pulse shaping and SPIDER pulse characterization. Adaptive pulse shaping using the feedback of the supercontinuum spectral phase from the SPIDER measurement can counteract the possible continuum instabilities. Adaptive pulse compression has been studied extensively and interesting readers can refer to Yelin et al. [102] for details.

In contrast to the methods described above, we consider another way to generate clean, broad spectra from PCFs. The tailorable dispersion properties of the microstructured fiber provide an additional way to stabilize the supercontinuum spectral phase. The instabilities of the supercontinuum generation are partly caused by the high dispersion presented by the microstructured fiber regarding the whole supercontinuum spectral bandwidth. Although the zero GVD wavelength can be engineered from 500 nm to above 1500 nm, the net GVD can dramatically increase to several hundred ps/(nm km) for wavelength shift of 100 nm from the zero GVD point (high dispersion slope). However, by carefully choosing the structure parameters of fiber, e.g., core size and air-holes pitch, dispersion-flattened microstructrued fibers can be manufactured that have minimal dispersions over several hundred nm spectral range. In this chapter, we present the pulse compression simulation results based on the supercontinuum generation from dispersion flattened microstructured fibers using the nonlinear Schrödinger equation model.

6.2 Simulation of Pulse Compression Using Dispersion Flattened Microstructured Fiber

In this section we will discuss the schematics of pulse compression simulation using continuum generation of the dispersion-flattened microstructured fibers.

6.2.1 Dispersion Flattened Microstructured Fibers

Dispersion properties of microstructured fibers can be tailored by choosing proper air-holes sizes and filling fractions in the silica glasses [141]. Dispersion flattened microstructured fibers (DFMFs) [18] have applications in telecommunication systems, in which a uniform fiber respond in the different wavelength channels is essential to the wavelength-division multiplexing (WDM) system. DFMFs are also very important for any system supporting ultrashort soliton pulse propagation, since the residue third order dispersion can potentially destroy the soliton transmission features.

The idea of dispersion flattened photonic crystal fiber was first demonstrated in 1999 by Ferrando et al. [142], in which a full vector biorthonormal-basis modal method was used to calculate the waveguide dispersion with different core size to pitch ratio (a/Λ) and air filling fractions. As a result of compensation of the material dispersion from the waveguide contribution of the photonic crystal fiber, a near-zero flat chromatic dispersion (total fiber dispersion) is achieved for a wide spectral range (~200 nm) centered at 1050 nm. The material dispersion for the fused silica has a zero group-velocity-dispersion wavelength at 1.3 μm (see material dispersion curve in figure 2.1), the design of DFMF requires that not only the material dispersion is compensated at one specific wavelength, i.e., dispersion shifted microstructured fiber, but also a total (or near total) compensations of the material dispersion for a wide spectral range around that specific wavelength. DMFMs are mainly used for two wavelength ranges: the telecommunication window around 1.55 μm and the Ti:Sapphire laser wavelength range around 800 nm. Due to a high material dispersion slope around the zero GVD wavelength (1.3 μm) for fused silica, the demonstrations of the DFMF around the telecommunication

window are rather convenient. Many designs of the DFMFs [143-146] have been proposed during the past few years in the telecommunication window based on full-vector waveguide simulation methods, such as full-vector finite element method (FEM), finite difference method and biorthogonal modal method. Meanwhile, the precise controls of the microstructured fiber fabrication allow building the DFMFs at 1.55 μm according to the design parameters [147, 18, 148]. Reeves, et al., also clearly showed soliton effects to the supercontinuum generations [18]. Although the theory and fabrication of the DFMFs in the telecommunication window are well established by now, the development at the Ti:Sapphire laser wavelength is somehow limited by the relative high material dispersion for the fused silica. However, simulations have shown that it is possible to generated DFMF centered at 800 nm with a flat dispersion range over 200 nm [149]; similar simulation results have led to the fabrication of DFMFs at 1.5 μm . Meanwhile, microstructured fiber design using a genetic algorithm exhibits itself as an effective way to search all the combinations of fiber configurations to generate user-defined chromatic dispersion properties [150]. Therefore, the research of DFMF at 800 nm is still very promising.

6.2.2 Simulations of Pulse Compression

Simulations of pulse compression using the supercontinuum generations from dispersion flattened microstructured fibers involve the following steps, i.e., see figure 6.1 for details. First, continua are generated in DFMFs with specific dispersion curves using 30 fs transform-limited input pulses based on the nonlinear Schrödinger equation model. Second, the spectral phases of the generated supercontinua are numerically extracted and the required negative compensation phases are calculated. Finally, the negative

compensation phases are applied to the simulated pulse shaper compressor and the compressed pulse are generated with applying the original supercontinua with the net minimal spectral phase.

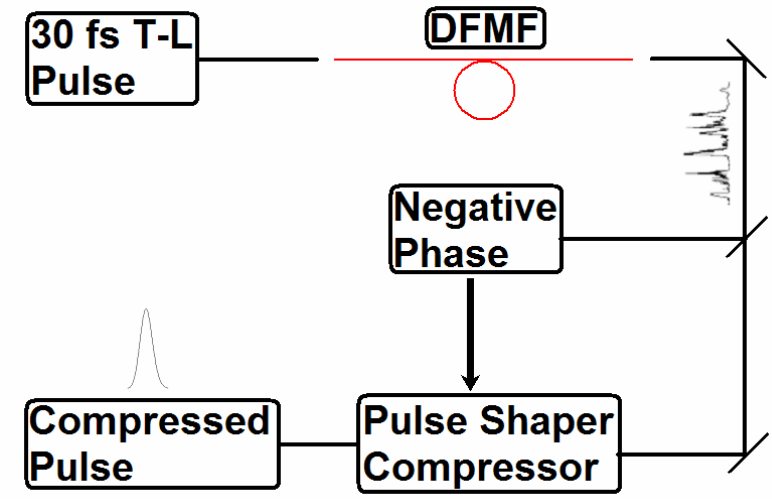

Figure 6.1: Schematics of pulse compression simulation using supercontinuum generation and dispersion flattened microstructured fiber. T-L pulse: transform-limited pulse. DFMF: dispersion flattened microstructured fiber.

To study the pulse compression using the simulated supercontinuum generations and DFMFs, we investigate several parameters. First and most importantly, pulse compression and supercontinuum generations depend critically on the microstructured fiber length and dispersion properties, e.g., different DFMFs centered either near the telecommunication window or Ti:Sapphire laser wavelength with different flattened dispersion curves. Second is the practical phase compensation effects associated experimental pulse shaper compressor using LC-SLM. The phase compensation resolution effects discussed in chapter 3 with different LC-SLM pixel numbers are simulated and discussed in this chapter. Meanwhile, pulse compression results using an ideal phase compensator, i.e., perfect phase compensation without the pixel effects, are also presented for comparison purposes. Also, input pulse properties such as the input

pulse peak power can dramatically affect the compression results. This effect is also discussed in our simulations.

6.3 Supercontinuum Pulse Compression at 800 nm

In this section we will focus on the simulations of supercontinuum pulse compression using DFMF for the Ti:Sapphire laser wavelength at 800 nm. We will first discuss the dispersion curve and parameters for the DFMF used in the simulations, followed by the investigations of fidelities of supercontinuum pulse compression. Finally, we present the pulse compression results for different input pulse power and propagation lengths.

6.3.1 Supercontinuum Generation Using DFMF at 800 nm

Since the fabrication of DFMFs at this wavelength have not been fully developed yet, we use a DFMF dispersion curve in Reeves et al. [18] and shift the center wavelength to 800 nm to study the possibilities of supercontinuum pulse compression at Ti:Sapphire laser wavelength.

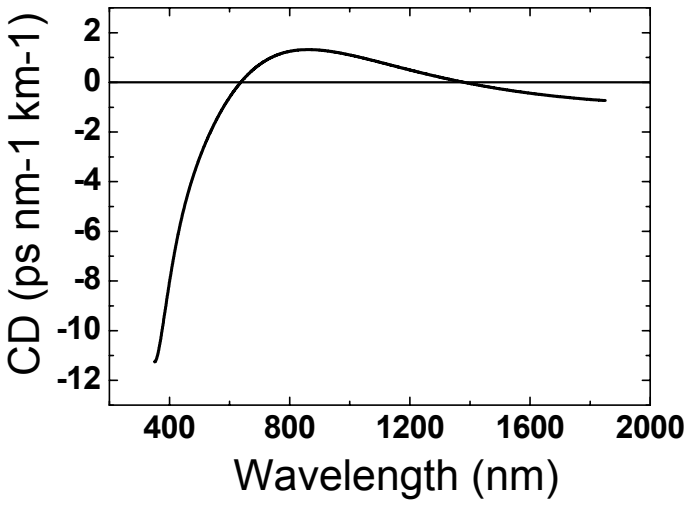

Figure 6.2: Dispersion profile for the DFMF around Ti:Sapphire laser wavelength at 800 nm. CD: chromatic dispersion.

Table 6.1: List of DFMF parameters in the NLSE simulation model at 800 nm.

Parameter (unit)	Values
n_2 (cm^2W^{-1})	2.2×10^{-16}
γ $(km^{-1}W^{-1})$	15.7
A_{eff} (μm^2)	11
β_2 (ps^2km^{-1})	-0.424
β_3 (ps^3km^{-1})	6.38×10^{-4}
β_4 (ps^4km^{-1})	6.86×10^{-7}
β_5 (ps^5km^{-1})	-3.03×10^{-9}
β_6 (ps^6km^{-1})	5.01×10^{-12}
β_7 (ps^7km^{-1})	-3.50×10^{-15}

The dispersion profile in figure 6.2 has a very wide range of flattened dispersion. In order to accurately describe the flattened dispersion in the nonlinear Schrödinger equation model, we use the dispersion coefficients up to the 7^{th} order defined in equation 2.12 and the values of these coefficients are listed in table 6.1, along with other fiber parameters. The time resolution is chosen as 0.5 fs and the sample number is 2^{14}=16384, which leads to a frequency resolution of 122 MHz.

Figure 6.3 is an example of output supercontinuum and spectral phase which is generated from 30 fs transform-limited pulses with peak power of 10 kW propagating through 9 cm of DFMF with dispersion profile shown in figure 6.2. There are several interesting features from the generated continuum. First, the spectral envelope shows a main signature of self-phase modulation nonlinear effect. It is understood that the

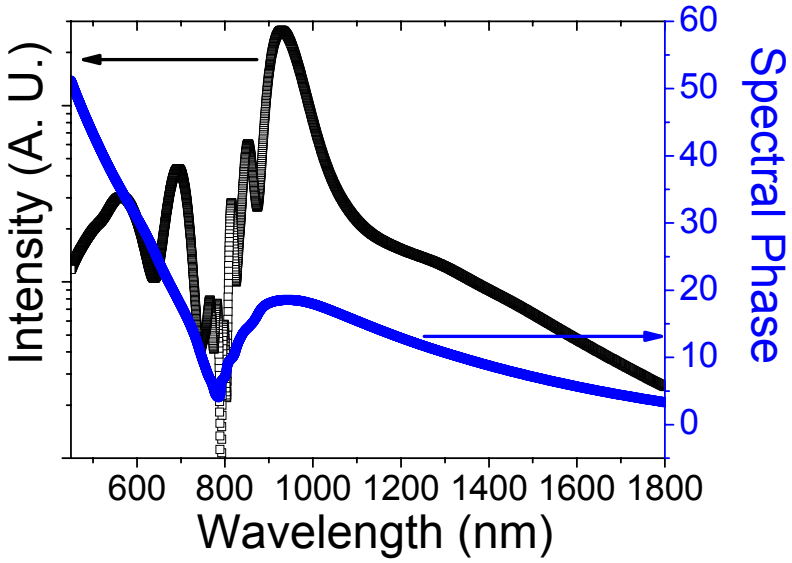

Figure 6.3: Supercontinuum output and spectral phase with 30 fs 10 kW T-L input pulse propagating through 9 cm DFMF. Smooth phase profile is generated with phase range within 60 rad.

superbroadband continuum generation is a result of higher soliton generation, followed by the soliton splitting to the longer wavelength and the blueshifted nonsolitonic radiation expanding to the shorter wavelength. The soliton is generated by the interplay between the self-phase modulation and fiber anomalous dispersion. In fact in the DFMF, the minimal flat dispersion prevents the higher order soliton generation. Therefore, as a result, continuum generation is dominant by the self-phase modulation and self-steepening nonlinear effects. Due to the minimal flat fiber dispersion, the spectral phase associate with the continuum generation is rather smooth in the entire spectral range except a relative small dip at the input wavelength 800 nm. The total spectral phase that needs to be compensated later by the simulated LC-SLM based pulse shaper is within 60 rad. The Nyquist limit discussed in chapter 3 requires that the phase difference between two adjacent SLM pixel to be less than π. Considering the current commercial availabilities

of 128 and 640 pixels SLM, it should be possible to compensate the phase range in figure 6.3; it also gives us more freedom to investigate the possible pulse compressibilities with higher input powers and longer DFMF propagating lengths. Note that because of the low responsivity for normal silicon based detector below 450 nm, the supercontinuum generated below this wavelength is cut off for future pulse compression.

6.3.2 Validation of Fidelity of Supercontinuum Pulse Compression

One of the most important prerequisite of performing pulse compression is the stability of the spectral phase. From the previous figure we see a smooth supercontinuum spectral phase generation for the entire spectrum and the phase range is well within the compensation range of the SLM. But if the spectral phase changes dramatically due to input pulse power fluctuation, and, since the system response time for phase retrieval/compensation is much longer than the corresponding phase change (governed by the pulse repetition rate, the compressed pulse using the phase compensation before the

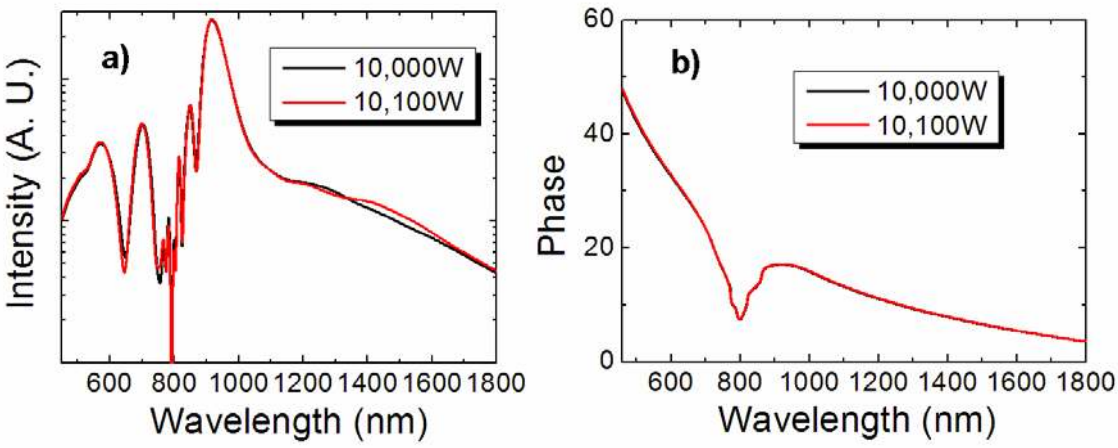

Figure 6.4: Simulation of output supercontinuum spectral intensity and phase variations with 1% input pulse noise. (a) is the intensity variation and (b) is the phase variation. Minimal variations for the spectrum and phase are shown in the figure.

phase change may be completely off the target. In order to preliminarily study this effect, we intentionally vary the input pulse peak power by 1%, a 10 times larger input pulse noise level compare to the level used in the previous research paper (0.1%, see Gaeta [9]). Figure 6.4 presents the simulation results of continuum generations upon 1% input pulse peak power fluctuation with the same input pulse and fiber parameters used in figure 6.3. Although there is a minimal spectral intensity changing with the input noise level, the corresponding fluctuations in spectral phase above 600 nm are unobservable.

The compressed pulse quality (or pulse compressibility) is closely related to the spectral coherence of the generated supercontinuum. The coherence function is defined as [17],

$$\left|g_{12}^{(1)}(\lambda)\right| = \left|\frac{\left\langle E_1^*(\lambda)E_2(\lambda)\right\rangle}{\sqrt{\left\langle\left|E_1(\lambda)\right|^2\right\rangle\left\langle\left|E_2(\lambda)\right|^2\right\rangle}}\right| \tag{6.1}$$

where the angle brackets denote an ensemble average over independently generated supercontinuum pairs $[E_1(\lambda), E_2(\lambda)]$. The coherence values have been widely accepted as a criterion to access the possible compressibilities for the supercontinuum generation [137, 14, 17] and a median coherence of 0.7 can be used as an indicator of good compressibility. Figure 6.5 (b) shows 100 run simulations of supercontinuum generation when the input pulse power has 5% RMS fluctuation, with all the other pulse and fiber parameters fixed. The black continuum curve in the figure shows the averaged supercontinuum spectrum. The calculated coherence values as a function of wavelength are shown in figure 6.5 (a). There is a good coherence over a wide spectrum range except at the input pulse wavelength 800 nm and below 600 nm. It is worth mentioning that the 5% RMS input power noise is equivalent to the random input power fluctuation range

from 90% to 110%. In practical, this is based on the low frequency classical noise that may present over the relative long phase retrieval time (several seconds for a single SPIDER measurement). This noise level is far above the typical Ti:Sapphire laser pulse shot-to-shot noise level which is only on the order of 0.1% [9]. In general, the coherence results showed in figure 6.5 (a) validate that the supercontinuum pulse compression gives a good fidelity using the DFMF approach.

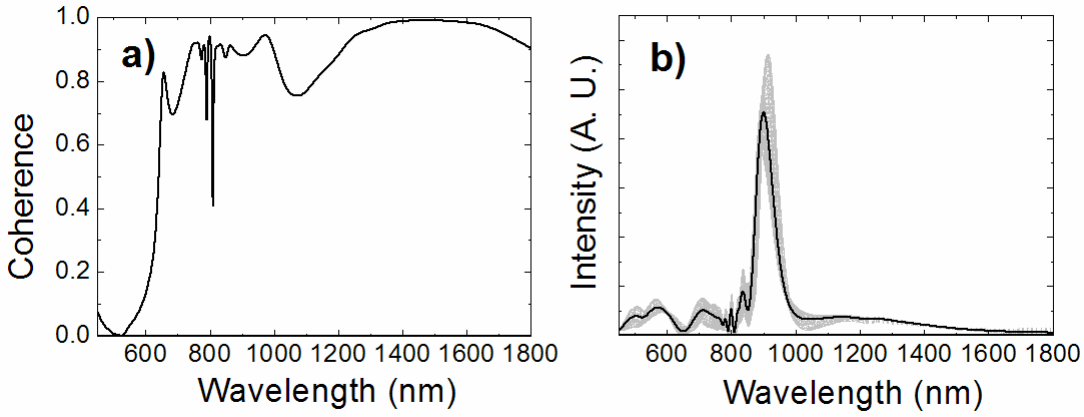

Figure 6.5: Calculated coherence as a function of wavelength from the electric field of continuum generation for 5% RMS input pulse power noise in 100 runs. (a) Coherence curve for the entire continuum spectrum. (b) Output spectrum with 5% input power noise for 100 run supercontinuum generations.

To further illustrate that using the DFMF can greatly *improve* the fidelity of supercontinuum pulse compression, we compare the simulations of generated continuum spectral intensity/phase using DFMF and a regular microstructured fiber, e.g., the microstructured fiber used in the open- and closed-loop control experiments in the previous two chapters. The simulation results are shown in figure 6.6. All the input pulse parameters are the same for the simulation comparison and the peak intensity of the input pulse is 8 kW. The same propagation length of 11 cm is used for both fibers. Figure (a) is a comparison of generated continuum spectra for DFMF and the regular

microstructured fiber; figure (b) shows the spectral phases. The differences in both figures for the continuum spectra and phases are quite obvious. The supercontinuum generated using the DFMF is much broader and smoother comparing to that of the regular microstructured fiber, indicating a much shorter compressed pulse providing successful phase compensations. The continuum spectral phase for the DFMF is rather smooth for the entire spectral range, especially for the spectral range above 900 nm. Meanwhile, the high modulations showed in the continuum envelope for the regular microstructured fiber exhibit themselves as abrupt phase jumps for the entire spectral range. Although the spectral continuum features are mainly in the range from 600 nm to 1000 nm and the spectral phase is relatively flat in the middle, the phase jumps on the edges of the window can not be well compensated by the SLMs. As a result, the supercontinuum generated by DFMF shows an enhanced pulse compressibility comparing to that of regular microstructured fiber.

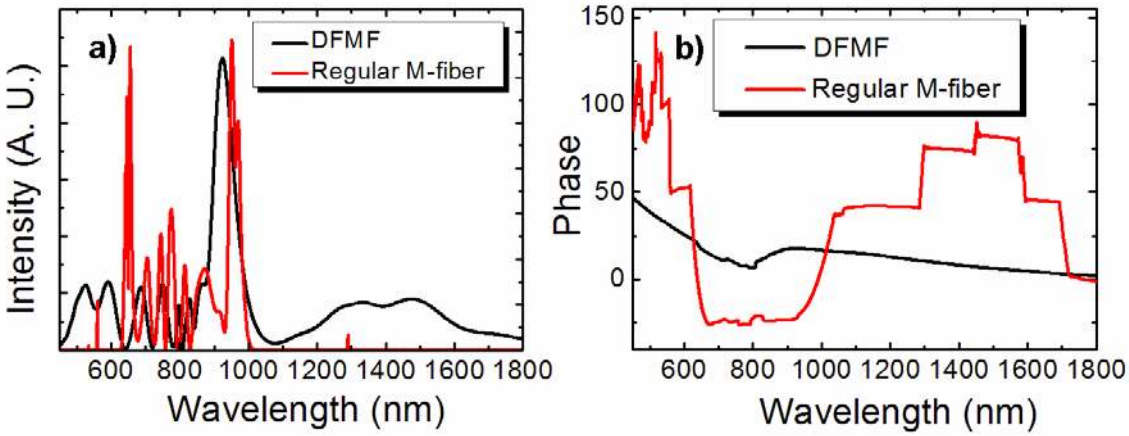

Figure 6.6: Simulated continuum generation for DFMF fiber and a regular microstructured fiber. (a), comparison of output spectra. (b), comparison of spectral phases. A much broader continuum spectrum and smooth phase for the DFMF are the direct proof of the enhanced pulse compressibility.

To generalize this section, there are several considerations for the supercontinuum pulse compression based on the phase compensation. First and most importantly, a stable continuum spectral phase that is not very sensitive to the input pulse noise is a prerequisite. For the purposes of characterizing the simulation result, using the coherence curve corresponds to an ensemble of continuum generation results for different input pulse noises level is a very convenient way to gain insight of the qualities of compressed pulses. In fact, the 5% RMS input pulse noise level used in this section is quite large compare to the normal laser shot-to-shot noise level. To our knowledge, only in Schenkel et al. [17] that the authors use this 5% RMS noise level to determine the supercontinuum compressibility, while shot-to-shot noise level (<1%) is used by all the other simulation papers. Second, even with a good coherence results, the supercontinuum pulse compression is also affected by the smoothness and the range of the continuum spectral phase. This is because of the limited phase compensation abilities of the SLM based pulse compressor. In fact, the phase compensation abilities determined by the Nyquist limit for the SLM with different pixel numbers are actually overstatements from our experiences. Therefore, smooth continuum spectral phase with small range, (e.g., less than several hundred for the entire compensation range for 640-pixel SLM), are also very important for experimentally performing the supercontinuum pulse compression. We are going to discuss this effect later in this chapter.

6.3.3 Supercontinuum Pulse Compression Results at 800 nm

Compression of the supercontinuum pulse using DFMF require phase compensations of generated supercontinua, which are simulated by adding calculated negative phase to the original continua, i.e., simulated pulse compressor. To investigate the pixel effects related to the practical SLM based pulse shaper, pulse compression

results correspond to different SLM pixel numbers are simulated. For comparison purposes, compression results using an ideal phase compensator with infinite SLM pixel number are also presented. Figure 6.7 is an example of pulse temporal intensity profiles before and after pulse compression. The simulation results correspond to 8 kW input pulse propagating through 10 cm DFMF. Compressed pulses using phase compensators with different SLM pixel numbers (128, 640) and an ideal compensator are shown in figure 6.7 (b). The phase compensation is performed as the following steps. First, the supercontinuum spectral phase for the designated compensation range is sliced into a number of regions depending on the simulated SLM pixel numbers. The average phase values in each region are calculated and treated as the values for SLM phase compensation. Each calculated average phase value is subtracted from the original spectral phase point in the regions and the net results are the compensated spectral phases. Finally, an inverse Fourier transformation is performed to generate the compressed pulses.

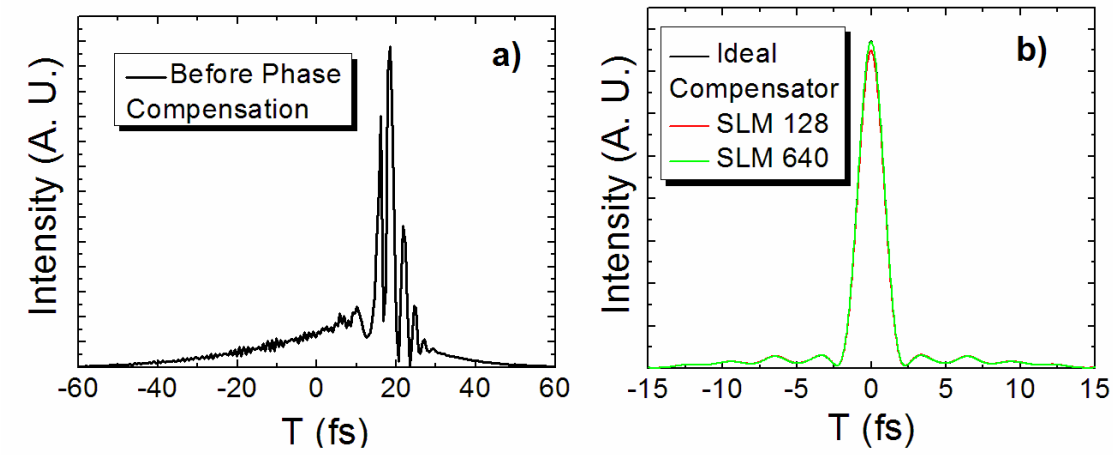

Figure 6.7: Simulated supercontinuum pulse compression for DFMF fiber. a), supercontinuum temporal pulse before phase compensation. b), compressed pulses using SLMs with different pixel numbers and an ideal phase compensator.

For experimental considerations of pulse compression based on the Fourier domain pulse shaping using SLM, section 3.5.2 gives detailed formula description illustrating the temporal field of the shaped pulse. In figure 6.7 (b), the pulse is compressed to ~2 fs using simulated pulse compressor with different SLM pixel numbers. Evidently, compressed pulse with 640-pixel SLM faithfully reproduces the pulse shape comparing to that of ideal compressor. 128-pixel SLM can also compensates the spectral phase very well; a small peak intensity drop for the compressed pulse is barely observable. This can be explained as a result of the combination of generated smooth continuum spectral phase and the total phase range (<60 rad) for the entire spectrum, as well as and phase compensation abilities of 128-pixel SLM discussed in the previous section.

Finally, we simulate supercontinuum pulse compression using DFMF for different fiber propagation lengths and input pulse peak powers. The pulse duration after phase compensation is calculated as the full-width-half-maximum (FWHM) of the compressed

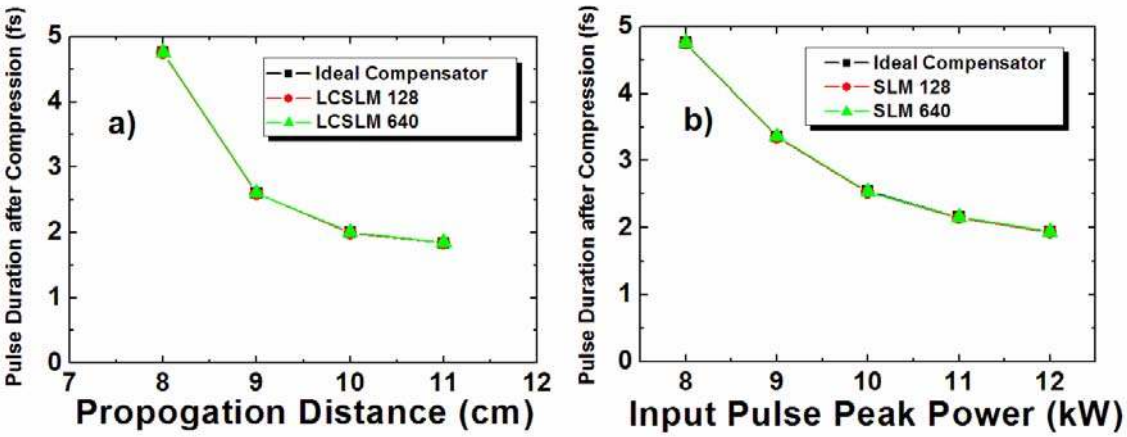

Figure 6.8: Simulated supercontinuum pulse compression results using DFMF for different fiber lengths and input pulse peak powers at 800 nm. (a) Compression results for different fiber lengths with 8 kW input power. (b) Compression results for different input pulse peak powers propagating through 8 cm fiber length.

pulse. Figure 6.8 (a) shows the compressed pulse durations as a function of fiber propagation distance using 30 fs T-L input pulse with 8 kW peak power. Pulse compression results for different input pulse peak power with a fixed 8 cm DFMF are shown in figure 6.8 (b). Both figures list the pulse compression results using three phase compensation resolutions: 128-pixel SLM, 640-pixel SLM and an ideal compensator. Pulse compression results of less than 2 fs are acquired with high input power and long propagation length. Note that for these simulation results, 128-pixel SLM is good enough to perform precise phase compensation and generating short compressed pulses.

6.4 Supercontinuum Pulse Compression 1550 nm

In this section we will briefly discuss the simulations of supercontinuum pulse compressions using DFMF at telecommunication wavelength 1550 nm. For this wavelength, the simulations and fabrications for the DFMFs have been well established and fibers are commercially available. Therefore, we use the dispersion property of a real DFMF [18] to simulate the supercontinuum generation and the feasibilities of pulse compression at 1550 nm.

The fiber dispersion and nonlinear parameters are listed in table 4.2. The dispersion curve is shown in figure 6.9 (a) inset. The dispersion shape is the same as the dispersion curve described in the previous section, except that the center wavelength is shifted to 1550 nm.

Figure 6.9 (a) is an example of supercontinuum generation using the DFMF at 1550 nm, with 30 fs 10 kW T-L input pulse propagating through 50 cm of fiber length. Comparing to figure 6.3 of the supercontinuum generation for DFMF at 800 with the same input pulse propagating through only 9 cm fiber, the supercontinuum generation ability for the DFMF at 1550 is greatly diminished. This is because of the relative large

Table 6.2: List of DFMF parameters in the NLSE simulation model at 1550 nm.

Parameter (unit)	Values
n_2 (cm^2W^{-1})	2.2×10^{-16}
γ $(km^{-1}W^{-1})$	2.03
A_{eff} (μm^2)	44
β_2 (ps^2km^{-1})	-1.55
β_3 (ps^3km^{-1})	6.5×10^{-3}
β_4 (ps^4km^{-1})	6.1×10^{-5}
β_5 (ps^5km^{-1})	-1.04×10^{-7}
β_6 (ps^6km^{-1})	-1.01×10^{-10}

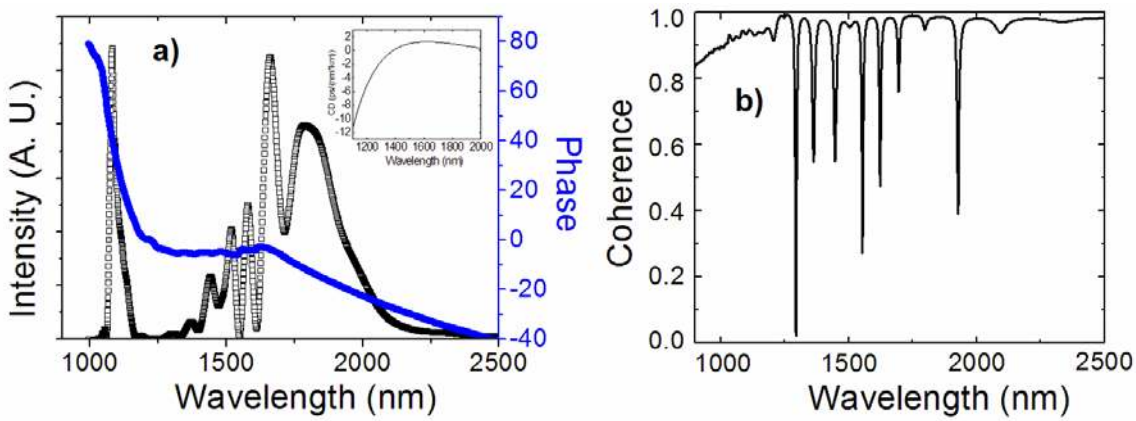

Figure 6.9: Simulated supercontinuum generation and coherence for DFMF at 1550 nm. (a) An example of generated continuum spectral intensity and phase. Inset: dispersion curve for the DFMF at 1550 nm. (b) Calculated coherence as a function of wavelength.

effective area, e.g., 44 μm^2 for 1550 nm and 11 μm^2 for 800 nm, the nonlinear coefficient is 8 times smaller than that for the DFMF at 800 nm. Meanwhile, the signature of the self-phase modulation nonlinear effect in the continuum envelope is quite

obvious. For the coherence properties at 1550 nm, we use 100-run simulations of supercontinuum generation with input pulse noise level of 1% RMS, which is realistic considering the input pulse shot-to-shot noise level of the order of 0.1%. The calculated coherence values as a function of wavelength are plotted in Figure 6.9 (b). Taking the coherence value of 0.7 as a standard to determine the compressibility of supercontinuum generation, the coherence curve is rather good for the entire spectral range, except a few dips corresponding to the modulations in the spectral envelope.

The longer propagation length leads to a larger phase range for the entire spectrum. In fact, although the phase range needs to be compensated is less than 120 rad, the compensation ability of 128-pixel SLM is not sufficient for precise phase compensation. Figure 6.10 shows the compressed pulse durations for different DFMF lengths and input pulse peak powers. The input pulse power for figure 6.10 (a) is 10 kW and the propagation length for figure 6.10 (b) is 20 cm. As evidenced in figure 6.10 (a), the compressed pulse durations have visible discrepancies for phase compensation performed by the 128-pixel SLM and ideal phase compensator. Although the compressed pulse shapes using 640-pixel SLM still faithfully follow that of the ideal compensator, the compressed pulse temporal range for the 128-pixel SLM is much wider than the other two cases. An example of this deficient phase compensation ability for the 128-pixel SLM will be given later in this chapter. In fact, the simple FWHM metric to describe pulse duration is no longer valid in this case. However, experimentally performing the precise phase compensation is still feasible by using 640-pixel SLM. Meanwhile, the continuum pulse compression results shown in figure 6.10 have a lower limit of ~ 5 fs,

which is comparable to the current state-of-art supercontinuum pulse compression experimental record.

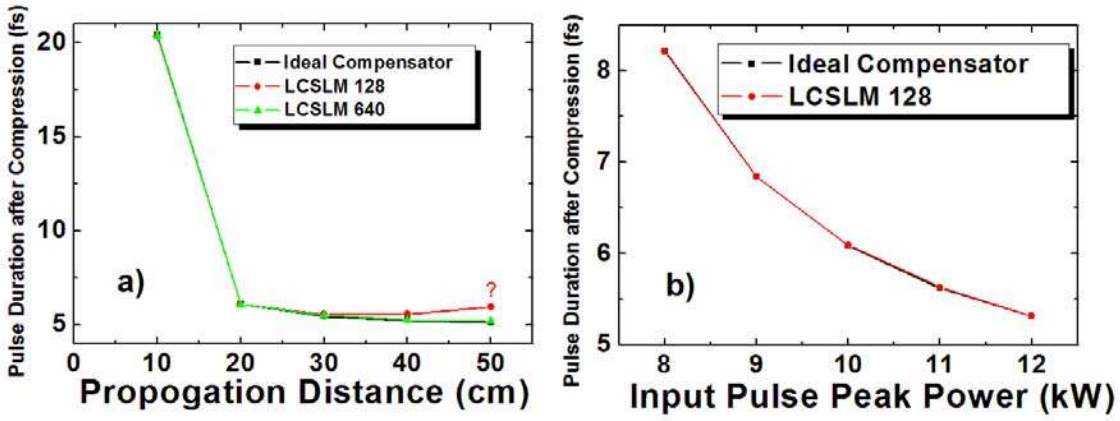

Figure 6.10: Simulated supercontinuum pulse durations after compression using DFMF at 1550 nm for different fiber lengths and different input pulse peak powers. (a) Compression results for different fiber lengths. (b) compression results for different input power.

6.5 Supercontinuum Pulse Compression 1050 nm

For comparison of the supercontinuum pulse compression using DFMFs, we simulate the compression results using a commercially available nonlinear microstructured fiber (Crystal Fibre, NL-1050-ZERO-2) at 1050 nm. The dispersion curve and fiber parameters are shown in figure 6.11 and table 4.3, respectively. This fiber has a relative high nonlinearity of 37 $km^{-1}W^{-1}$ compare to the DFMFs in the previous discussion, e.g., 2.03 $km^{-1}W^{-1}$ for DMFM at 1550 nm and 15.7 $km^{-1}W^{-1}$ for DMFM at 800 nm. This is the direct result of the extremely small effective area of only 3.52 μm^2 associated with this fiber. Although the nonlinearity of the fiber is relative high, it is still smaller than the other high nonlinearity fibers (range from 70 $km^{-1}W^{-1}$ to above 100 $km^{-1}W^{-1}$). Meanwhile, the dispersion is 10 times larger than that of DFMFs in the previous discussions.

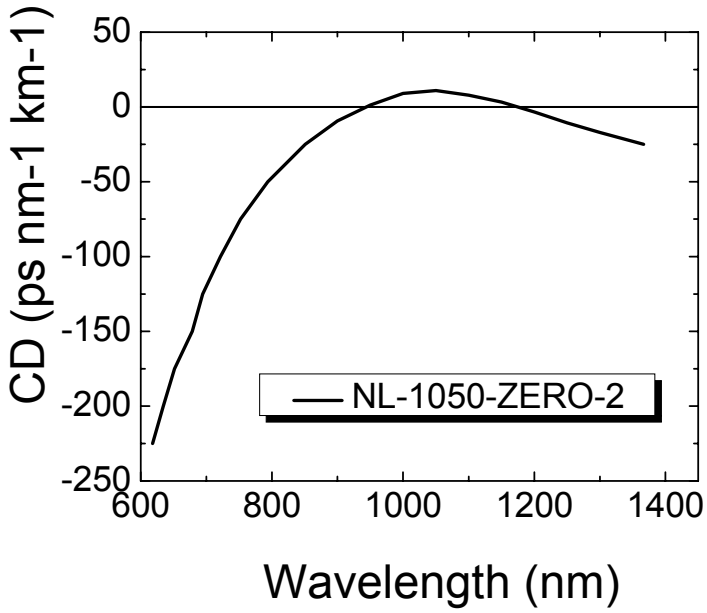

Figure 6.11: Dispersion curve for a nonlinear microstructured fiber.

Table 6.3: List of the nonlinear microstructured fiber parameters in the NLSE simulation model at 1050 nm.

Parameter (unit)	Values
n_2 (cm^2W^{-1})	2.2×10^{-16}
γ $(km^{-1}W^{-1})$	37.35
A_{eff} (μm^2)	3.52
β_2 (ps^2km^{-1})	-5.205
β_3 (ps^3km^{-1})	1.38×10^{-3}
β_4 (ps^4km^{-1})	2.416×10^{-4}
β_5 (ps^5km^{-1})	-7.542×10^{-7}
β_6 (ps^6km^{-1})	1.174×10^{-9}
β_7 (ps^7km^{-1})	-6.712×10^{-13}

The dispersion Taylor expansion coefficients up to 7th order are used in the simulation model with all the other input pulse and simulation parameters same as previous discussion.

Because of the large fiber dispersion, as we discussed in the first section of this chapter, extremely short fiber length has to be used to ensure the stabilities of generated continuum spectral phase. Unlike the tens of cm of fiber length used in the DFMFs, a fiber length on the order of mm has to be used for continuum pulse compression based on the dispersion properties of this nonlinear fiber. On the other hand, compare to the other nonlinear fiber used to perform continuum pulse compression, the nonlinearities of this fiber is very low. Therefore, to get a short compressed pulse, the input pulse power has to be large enough to generate sufficient continuum bandwidth. Figure 6.12 (a) is an example of broadband supercontinuum generation

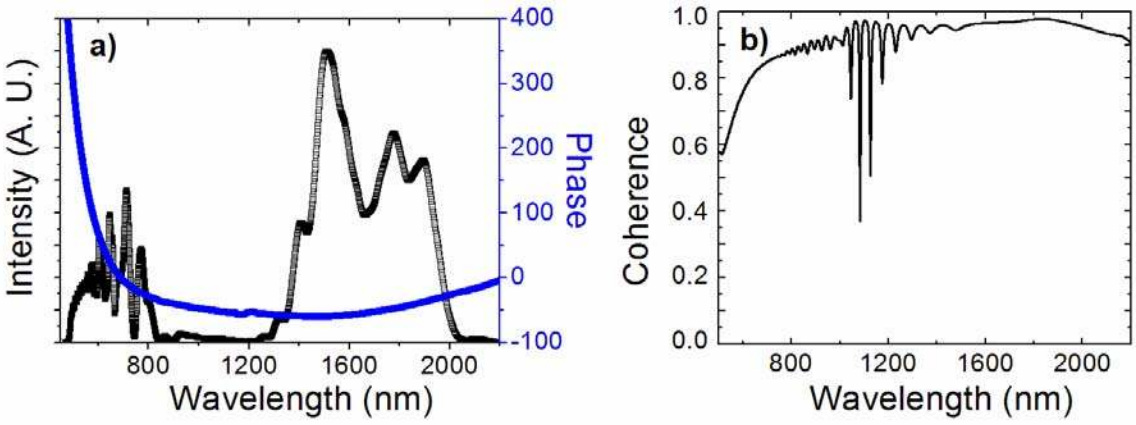

Figure 6.12: Supercontinuum generation and the coherence in the nonlinear fiber for 1 cm fiber length and 400 kW input pulse peak power. (a) Spectral intensity and phase for the supercontinuum generation. (b) Calculated Coherence as a function of wavelength.

with fiber length of only 1 cm and input pulse peak power 400 kW (or pulse energy of 1 mJ assuming 100 MHz pulse repetition rate). The peak power level is 40 times larger than that for the DFMF with the same generated continuum bandwidth. The coherence

results are calculated from 100-run continuum generation with 1% RMS input pulse noise. The coherence results shown in figure 6.12 (b) indicate a good compressibility. However, due to the large dispersion presented for this nonlinear fiber, the total phase range for the entire spectral window is over 400 rad.

From the previous discussion, it is not surprising that 128-pixel SLM can not compensate the phase within this range. This effect is shown in figure 6.13 (b) inset, where the deficiency of the phase compensation by the 128-pixel SLM manifests itself through the low intensity central feature and many small peaks on the larger time scale. Figure 6.13 (a) gives an example of the temporal pulse before the phase compensation, a much longer pulse comparing to that for the DFMFs. It is also clearly shown in figure 6.13 (b) that there is some discrepancy in the compressed pulse peak intensity even for the 640-pixel SLM phase compensation when compared to that of ideal phase compensator. Although a short compressed pulse is generated in

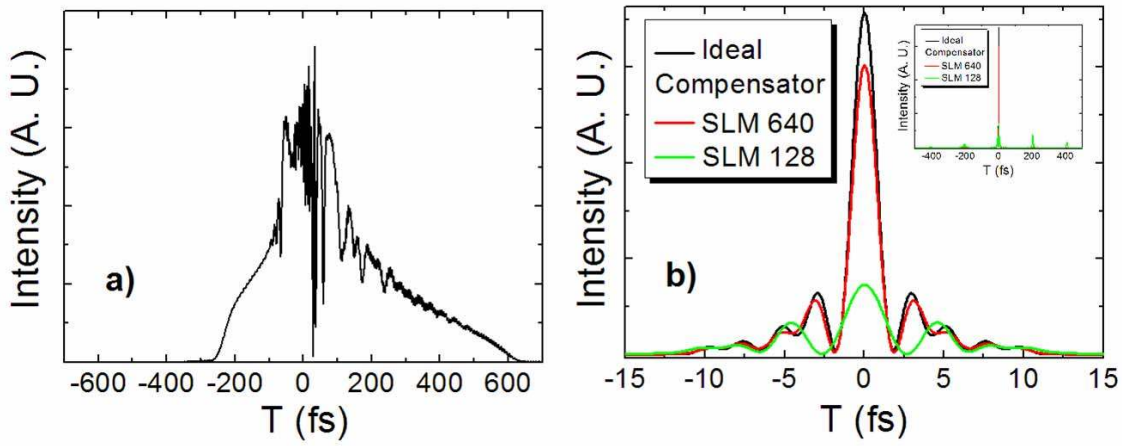

Figure 6.13: An example of continuum temporal pulse before and after phase compensation for the nonlinear fiber at 1050 nm. (a) Temporal pulse before compression. (b) Temporal pulse after the phase compensation with different SLM pixel numbers. Figure (b) shows the effects of insufficient SLM phase compensation.

the simulation, the insufficient phase compensation for the large phase range presented because of the dispersion properties of the nonlinear fiber may cause serious problems in the real experiment.

CHAPTER 7
CONCLUSION

In this work, we have presented both experimental and simulation results of characterizing and controlling the extreme nonlinear supercontinuum generations in photonic crystal fibers using two different approaches: the input pulse characteristics and photonic crystal fiber properties.

Owing to the ability to tailor the waveguiding properties of microstructured fibers, the zero group-velocity-dispersion point of the fiber can be engineered at any wavelength from 500 nm to above 1500 nm. This allows for the control of the dispersive properties of the fiber, and in particular, allows us to shift the dispersion point below 800 nm, Ti:Sapphire laser wavelength. Thus, femtosecond pulses can be easily generated in the anomalous dispersion region of the microstructured fiber. Meanwhile, the high nonlinearities of the microstructured fiber due to the extremely small effective area, in particular, higher order soliton generation followed by the subsequent soliton splitting and other nonlinear effects, lead to the greater than octave-spanning ultrabroadband supercontinuum generation with pulses only a few nanoJoules in energy.

The supercontinuum generation properties in the microstructured fibers depend critically on the input pulse characteristics. We have used femtosecond pulse shaping to change the intensity temporal profiles of the Ti:Sapphire lasers input pulses. Depending on whether an intuitive control pulse can be directly derived, we have used both open-loop and closed loop control to study how the input pulse characteristics can affect the temporal and spectral evolutions of the supercontinuum generations. Also, we have

developed a simulation tool based on the extended nonlinear Schrödinger equation to model our experiments and predict the continuum outputs. For open-loop control, we investigate the effects of input pulse quadratic and cubic phase to the bandwidth of supercontinuum generation. The broadest supercontinuum generation occurs with transform-limited input pulses, (i.e., pulses without any residual spectral phase), when the input pulse central wavelength is in the anomalous dispersion region of the microstructured fibers. This is because the magnitude of the nonlinear effects that lead to the supercontinuum generation is directly proportional to the input pulse peak power; our simulation results also verify that the transform-limited pulse has the largest peak intensity. Furthermore, the input pulse cubic phase plays an important role when the input pulse center wavelength is near to the zero group-velocity-dispersion point of the microstructured fiber. Our experimental results show that input pulses with cubic spectral phase that has the same magnitude and opposite sign when compared to the fiber third order dispersion-induced pulse spectral phase lead to the supercontinuum generation with the largest bandwidth. This is can be explained as the corresponding pulse self-compression leading to the increased peak intensity; therefore enhancing the magnitude of the pulse nonlinear interaction with the microstructured fiber, followed by the broader supercontinuum generation. Meanwhile, the self-steepening nonlinear effect is responsible for the blue-shifted supercontinuum generation asymmetry. We have generated phase-sculpted temporal ramp pulses to suppress the self-steepening effect. The FROG measurements were used to verify the generation of the temporal ramp pulse. Both experimental and simulation results show that more symmetric supercontinuum generations are achieved due to the suppression of the self-steepening nonlinear effect.

For the closed-loop control experiments, we have used “adaptive” pulse shaping with genetic algorithm to investigate the nonlinear broadening enhancement and soliton self-frequency shift for the supercontinuum generation. The feedback controls use the genetic algorithm to efficiently search all the parameter spaces and derive suitable driving pulses for different control goals. A nonlinear broadening enhancement of 20% was achieved. A close examination of the driving pulse spectral phase evolutions for each generation reveals that the genetic algorithm is able to generate the driving pulse with the optimized spectral phase that interacts with the all orders of fiber dispersion. Also, by carefully design the parameter space and cost function, we perform the controls of both the magnitude of soliton self-frequency shift and the width of the generated soliton. By feeding the spectral phases of the driving pulses into the simulation model, it is clear that the phase-only pulse shaper acts as a sensitive amplitude filter and the genetic algorithm generates the driving pulse with suitable peak intensity and duration; therefore solitons generation with different widths and self-frequency shift magnitudes are achieved.

The tailorable dispersion properties of the microstructured fiber yield another way to perform the control of supercontinuum generation. We have used the simulated dispersion flattened microstructured fiber to investigate the possibility of supercontinuum pulse compression. Simulated pulse compression results using DFMFs at different center wavelengths are presented. In particular, for both Ti:Sapphire laser wavelength and telecommunication wavelength, our simulation results have shown that using DFMFs greatly enhances the stabilities of the generated supercontinuum spectral phase, therefore improves the qualities of the supercontinuum pulse compression. Meanwhile, we have also discussed the phase compensation abilities associate with the practical SLM pixel

number and present the pulse compression results corresponding to the different input pulse peak power and fiber lengths. For comparison, we present the simulation results using a nonlinear microstructured fiber with high dispersion property and discuss the limitations of conventional supercontinuum pulse compression.

To our knowledge, we have presented for the first time how the femtosecond pulse shaping can be used to control the supercontinuum generation by controlling the evolution of the temporal and spectral structure of optical pulses propagating in the microstructured fibers. Also, supercontinuum pulse compression using DFMFs has presented itself as a new approach to stabilize the continuum spectral phase and improve the quality of compressed pulses.

LIST OF REFERENCES

1. T. Miya, Y. Terunuma, T. Hosaka and T. Miyashita, "Ultimate low-loss single-mode fibre at 1.55 μm," *Electronics Letters*, 15, 106, 1979.

2. G. Keiser, *Optical Fiber Communications*, 3rd ed., McGraw-Hill, New York, 2000.

3. G. P Agrawal, *Nonlinear Fiber Optics*, 3rd ed., Academic Press, San Diego, 2001.

4. J. C. Knight, T. A. Birks, P.S. Russell and D. M. Atkin, "All-silica single-mode optical fiber with photonic crystal cladding," *Optics Letters*, 21, 1547, 1996.

5. J. K. Ranka, R. S. Windeler and A. J. Stentz, "Optical properties of high-delta air silica microstructure optical fibers," *Optics Letters*, 25, 796, 2000.

6. J. K. Ranka, R. S. Windeler and A. J. Stentz, "Visible continuum generation in air-silica microstructure optical fibers with anomalous dispersion at 800 nm," *Optics Letters*, 25, 25, 2000.

7. R. F. Cregan, B. J. Mangan, J. C. Knight, T. A. Birks, P. S. Russell, P. J. Roberts, and D. C. Allan, "Single-mode photonic band gap guidance of light in air," *Science*, 285, 1537, 1999.

8. Nobelprize.org, "The Nobel Prize in Physics 2005," 2005, http://nobelprize.org/physics/laureates/2005/index.html, last accessed March, 2006.

9. A. L. Gaeta, "Nonlinear propagation and continuum generation in microstructured optical fibers," *Optics Letters*, 27, 924, 2002.

10. A. V. Husakou and J. Herrmann, "Supercontinuum generation of higher-order solitons by fission in photonic crystal fibers," *Physical Review Letters*, 87, 203901, 2001.

11. J. Herrmann, U. Griebner, N. Zhavoronkov, A. Husakou, D. Nickel, J. C. Knight, W. J. Wadsworth, P. S. Russell, and G. Korn, "Experimental evidence for supercontinuum generation by fission of higher-order solitons in photonic fibers," *Physical Review Letters*, 88, 173901, 2002.

12. K. L. Corwin, N. R. Newbury, J. M. Dudley, S. Coen, S. A. Diddams, K. Weber and R. S. Windeler, "Fundamental noise limitations to supercontinuum generation in microstructure fiber," *Physical Review Letters*, 90, 113904, 2003.

13. X. Gu, L. Xu, M. Kimmel, E. Zeek, P. O'Shea, A. P. Shreenath, R. Trebino, and R. S. Windeler, "Frequency-resolved optical gating and single-shot spectral measurements reveal fine structure in microstructure-fiber continuum," *Optics Letters*, 27, 1174, 2002.

14. J. M. Dudley and S. Coen, "Fundamental limits to few-cycle pulse generation from compression of supercontinuum spectra generated in photonic crystal fiber," *Optics Express*, 12, 2423, 2004

15. G. Q. Chang, T. B. Norris and H. G. Winful, "Optimization of supercontinuum generation in photonic crystal fibers for pulse compression," *Optics Letters*, 28, 546, 2003.

16. K. Yamane, Z. Zhang, K. Oka, R. Morita and M. Yamashita, "Optical pulse compression to 3.4 fs in the monocycle region by feedback phase compensation," *Optics Letters*, 28, 2258, 2003.

17. B. Schenkel, R. Paschotta and U. Keller, "Pulse compression with supercontinuum generation in microstructure fibers," *Journal of the Optical Society of America B*, 22, 687, 2005.

18. W. H. Reeves, D. V. Skryabin, F. Biancalana, J. C. Knight, P. S. Russell, F. G. Omenetto, A. Efimov and A. J. Taylor, "Transformation and control of ultrashort pulses in dispersion-engineered photonic crystal fibres," *Nature*, 424, 511, 2003.

19. J. Hecht, *City of Light*, Oxford University Press, New York, 1999.

20. J. A. Buck, *Fundamentals of Optical Fibers*, John Wiley & Sons, Inc., New York, 1995.

21. H. Takara, et al., "More than 1000 channel optical frequency chain generation from single supercontinuum source with 12.5 GHz channel spacing," *Electronics Letters*, 36, 2089, 2000.

22. A. W. Snyder and J. D. Love, *Optical Waveguide Theory*, Chapman and Hall, London, 1983.

23. A. J. Antos, K. Smith, "Design and characterization of dispersion compensating fiber based on the LP_{01} mode," *Journal of Lightwave Technology*, 12, 1739, 1994.

24. T. A. Birks, D. Mogilevtsev, J. C. Knight, P. S. Russell, "Dispersion compensation using single-material fibers," *IEEE Photonics Technology Letters*, 11, 674, 1999.

25. J. P. Laude, *DWDM Fundamentals, Components, and Applications*, Artech House, Boston, 2002.

26. L. F. Mollenauer, R. H. Stolen and J. P. Gordon, "Experimental observation of picosecond pulse narrowing and solitons in optical fibers," *Physical Review Letters*, 45, 1095, 1980.

27. R. R. Alfano and S. L. Shapiro, "Emission in the region 4000 to 7000 Å via four-photon coupling in glass," *Physical Review Letters*, 24, 584, 1970.

28. G. A. Nowak, J. Kim and M. N. Islam, "Stable supercontinuum generation in short lengths of conventional dispersion-shifted fiber," *Applied Optics*, 38, 7364, 1999.

29. V. E. Zakharov and A. B. Shabat, "Exact theory of two-dimensional self-focusing and one-dimensional self-modulation of waves in nonlinear media," *Soviet Physics Journal of Experimental and Theoretical Physics*, 34, 62, 1972.

30. P. Yeh and A. Yariv, "Bragg reflection waveguides," *Optics Communications*, 19, 427, 1976.

31. P. S. Russell, "Photonic crystal fibers," *Science*, 299, 358, 2003.

32. J. C. Knight, T. A. Birks, P. S. Russell, J. P. de Sandro, "Properties of photonic crystal fiber and the effective index model," *Journal of the Optical Society of America A*, 15, 749, 1998.

33. J. C. Knight, J. Broeng, T. A. Birks, and P. S. Russel, "Photonic band gap guidance in optical fibers," *Science*, 282, 1476, 1998.

34. S. O. Konorov, A. B. Fedotov and A. M. Zheltikov, "Enhanced four-wave mixing in a hollow-core photonic-crystal fiber," *Optics Letters*, 28, 1448, 2003.

35. F. Fogli, L. Saccomandi, P. Bassi, G. Bellanca and S. Trillo, "Full vectorial BPM modeling of index-guiding photonic crystal fibers and couplers," *Optics Express,* 10, 54, 2002.

36. R. Ghosh, A. Kumar and J. P. Meunier, "Waveguiding properties of holey fibres and effective-V model," *Electronics Letters*, 35, 1873, 1999.

37. C. E. Kerbage, B. J. Eggleton, P. S. Westbrook, and R. S. Windeler, "Experimental and scalar beam propagation analysis of an air-silica microstructure fiber," *Optics Express*, 7, 113, 2000.

38. S. G. Johnson and J. D. Joannopoulos, "Block-iterative frequency-domain methods for Maxwell's equations in a planewave basis," *Optics Express*, 8, 173, 2001.

39. J. M. Fini, "Analysis of microstructure optical fibers by radial scattering decomposition," *Optics Letters*, 28, 992, 2003.

40. Z. Zhu and T. G. Brown, "Full-vectorial finite-difference analysis of microstructured optical fibers," *Optics Express*, 10, 853, 2002.

41. M. Koshiba, “Full-vector analysis of photonic crystal fibers using the finite element method,” *IEICE Transactions on Electronics*, E85C, 881, 2002.

42. T. A. Birks, J. C. Knight and P. S. Russell, “Endlessly single-mode photonic crystal fiber,” *Optics Letters*, 22, 961, 1997.

43. J. C. Knight, T. A. Birks, R. F. Cregan, P. S. Russell and J. P. de Sandro, “Large mode area photonic crystal fibre,” *Electronics Letters*, 34, 1347, 1998.

44. J. C. Baggett, T. M. Monro, K. Furusawa and D. J. Richardson, “Comparative study of large-mode holey and conventional fibers,” *Optics Letters*, 26, 1045, 2001.

45. K. Saitoh and M. Koshiba, “Single-polarization single-mode photonic crystal fibers,” *IEEE Photonics Technology Letters*, 15, 1384, 2003.

46. C. Kerbage and B. J. Eggleton, “Numerical analysis and experimental design of tunable birefringence in microstructured optical fiber,” *Optics Express*, 10, 246, 2002.

47. A. B. Fedotov, A. N. Naumov, S. O. Konorov, V. I. Beloglazov, L. A. Mel’nikov, N. B. Skibina, D. A. Sidorov-Biryukov, A. V. Shcherbakov, and A. M. Zheltikov, “Photonic-molecule modes of a microstructure cobweb fiber,” *Laser Physics*, 12, 1363, 2002.

48. J. C. Knight, J. Arriaga, T. A. Birks, A. Ortigosa-Blanch, W. J. Wadsworth and P. S. Russell, “Anomalous dispersion in photonic crystal fiber,” *Photonics Technology Letters*, 12, 807, 2000.

49. N. G. R. Broderick, T. M. Monro, P. J. Bennett and D. J. Richardson, “Nonlinearity in holey optical fibers: measurement and future opportunities,” *Optics Letters*, 24, 1395, 1999.

50. S. Coen, A. H. L. Chau, R. Leonhardt and J. D. Harvey, J. C. Knight, W. J. Wadsworth and P. S. J. Russell, “Supercontinuum generation by stimulated Raman scattering and parametric four-wave mixing in photonic crystal fibers,” *Journal of the Optical Society of America B*, 19, 753, 2002.

51. A. V. Husakou and J. Herrmann, “Supercontinuum generation, four-wave mixing, and fission of higher-order solitons in photonic-crystal fibers,” *Journal of the Optical Society of America B*, 19, 2171, 2002.

52. F. G. Omenetto, A. J. Taylor, M. D. Moores, J. Arriaga, J. C. Knight, W. J. Wadsworth and P. S. J. Russell, “Simultaneous generation of spectrally distinct third harmonics in a photonic crystal fiber,” *Optics Letters*, 26, 1158, 2001

53. I. Cristiani, R. Tediosi, L. Tartara and V. Degiorgio, “Dispersive wave generation by solitons in microstructured optical fibers,” *Optics Express*, 12, 124, 2004.

54. N. Akhmediev and M. Karlsson, “Cherenkov radiation emitted by solitons in optical fibers,” *Physical Review A,* 51, 2602, 1995.

55. Q. Cao, X. Gu, E. Zeek, M. Kimmel, R. Trebino, J. Dudley and R. S. Windeler, “Measurement of the intensity and phase of supercontinuum from an 8-mm-long microstructure fiber,” *Applied Physics B: Lasers and Optics*, 77, 239, 2003.

56. S. Kawanishi and H. Kubota, “Photonic crystal fibers and their application to optical communications,” *NTT Review*, 15, 28, 2003.

57. D. G. Ouzounov, K. D. Moll, M. A. Foster, W. R. Zipfel, W. W. Webb and A. L. Gaeta, “Delivery of nanojoule femtosecond pulses through large-core microstructured fibers,” *Optics Letters*, 27, 1513, 2002.

58. Y. L. Hoo, W. Jin, C. Shi, Hoi L. Ho, D. N. Wang and S. C. Ruan, “Design and modeling of a photonic crystal fiber gas sensor,” *Applied Optics*, 42, 3509, 2003.

59. F. Benabid, J. C. Knight and P. S. Russell, “Particle levitation and guidance in hollow-core photonic crystal fiber,” *Optics Express*, 10, 1195, 2002.

60. F. Benabid, J. C. Knight, G. Antonopoulos and P. S. J. Russell, “Stimulated Raman scattering in hydrogen-filled hollow-core photonic crystal fiber,” *Science*, 298, 399, 2002.

61. T. Brabec and F. Krausz, “Intense few-cycle laser fields: frontiers of nonlinear optics,” *Reviews of Modern Physics,* 72, 545, 2000.

62. I. Hartl, X. D. Li, C. Chudoba, R. K. Ghanta, T. H. Ko, J. G. Fujimoto, J. K. Ranka and R. S. Windeler, “Ultrahigh-resolution optical coherence tomography using continuum generation in an air silica microstructure optical fiber,” *Optics Letters*, 26 , 608, 2001.

63. D. L. Marks, A. L. Oldenburg, J. J. Reynolds and S. A. Boppart, “Study of an ultrahigh-numerical-aperture fiber continuum generation source for optical coherence tomography,” *Optics Letters*, 27, 2010, 2002.

64. Y. Wang, Y. Zhao, J. S. Nelson, Z. Chen and R. S. Windeler, “Ultrahigh-resolution optical coherence tomography by broadband continuum generation from a photonic crystal fiber,” *Optics Letters*, 28, 182, 2003.

65. D. J. Jones, S. A. Diddams, J. K. Ranka, A. Stentz, R. S. Windeler, J. L. Hall and S. T. Cundiff, “Carrierenvelope phase control of femtosecond mode-locked lasers and direct optical frequency synthesis,” *Science* 288, 635, 2000.

66. S. T. Cundiff and J. Ye, “Colloquium: femtosecond optical frequency combs,” *Reviews of Modern Physics,* 75, 325, 2003.

67. T. Udem, R. Holzwarth and T. W. Hansch, "Optical frequency metrology," *Nature*, 416, 233, 2002.

68. S. A. Diddams, T. Udem, J. C. Bergquist, E. A. Curtis, R. E. Drullinger, L. Hollberg, W. M. Itano, W. D. Lee, C. W. Oates, K. R. Vogel, and D. J. Wineland, "An optical clock based on a single trapped 199Hg+ ion," *Science*, 293, 825, 2001.

69. S. Diddams, L. Hollberg, L.S. Ma and L. Robertsson, "Femtosecond-laserbased optical clockwork with instability < 6.3×10−16 in 1 s," *Optics Letters*, 27, 58, 2002.

70. K. Robinson, "Photonic crystal fiber enables optical clock," *Photonics Spectra*, 36, 45, 2002.

71. D. R. Goff and K. S. Hansen, *Fiber Optic Reference Guide: A Practical Guide to Communications Technology*, Third Edition, Focal Press, Woburn, 2002.

72. R. Kienberger, M. Hentschel, M. Uiberacker, Ch. Spielmann, M. Kitzler, A. Scrinzi, M. Wieland, T. Westerwalbesloh, U. Kleineberg, U. Heinzmann, M. Drescher and F. Krausz, "Steering attosecond electron wave packets with light," *Science*, 297, 1144, 2002.

73. T. H. Jeys, K. A. Smith, F. B. Dunning and R. F. Stebbings, "Investigation of fine-structure quantum beats in sodium Rydberg atoms by field ionization," *Physical Review A*, 23, 3065, 1981.

74. A. P. Heberle, J. J. Baumberg and K. Koehler, "Ultrafast coherent control and destruction of excitons in quantum wells," *Physical Review Letters*, 75, 2598, 1995.

75. B. Kohler, V. V. Yakovlev, J. Che, J. L. Krause, M. Messina, "Quantum control of wave packet evolution with tailored femtosecond pulses," *Physical Review Letters*, 74, 3360, 1995.

76. D. N. Fittinghoff, P. W. Wiseman, J. A. Squier, "Widefield multiphoton and temporally decorrelated multifocal multiphoton microscopy," *Optics Express*, 7, 273, 2000.

77. J. M. Girkin, "Optical physics enables advances in multiphoton imaging," *Journal of Physics D, Applied Physics*, 36, R250, 2003.

78. N. Katzenellenbogen and D. Grischkowsky, "Efficient generation of 380 fs pulses of THz radiation by ultrafast laser pulse excitation of a biased metal-semiconductor interface," *Applied Physics Letters*, 58, 222, 1991.

79. P. A. Norreys, et. al., "Observation of a highly directional gamma-ray beam from ultrashort, ultraintense laser pulse interactions with solids," *Physics of Plasmas*, 6, 2150, 1999.

80. S. A. Hosseini, B. Ferland and S. L. Chin, "Measurement of filament length generated by an intense femtosecond laser pulse using electromagnetic radiation detection," *Applied Physics B: Lasers and Optics*, 76, 583, 2003.

81. M. D. Shirk and P. A. Molian, "A review of ultrashort pulsed laser ablation of materials," *Journal of Laser Applications*, 10, 18, 1998.

82. C. Rulliere, Editor, *Femtosecond Laser Pulses: Principles and Experiment*, Springer, New York, 1998.

83. E. B. Treacy, "Compression of picosecond light pulses," *Physics Letters A*, 28, 34, 1968.

84. P. Lacovara, L. Estorowitz and M.Kokta, "Growth, spectroscopy, and lasing of titanium- doped sapphire," *IEEE Journal of Quantum Electronics,* QE 21, 1614, 1985.

85. C. E. Byvik and A. M. Buoncristiani, "Analysis of vibronic transitions in titanium doped sapphire using the temperature of the fluorescence spectra," *IEEE Journal of Quantum Electronics*, QE 21, 1619, 1985.

86. D. H. Sutter, G. Steinmeyer, L. Gallman, N. Matuscheck, F. Morier-Genoud and U. Keller, "Semiconductor saturable-absorber mirror-assisted kerr-lens mode-locked ti:sapphire laser producing pulses in the two-cycle regime," *Optics Letters*, 24, 631, 1999.

87. Wikipedia, the free encyclopedia, "Kerr-lens modelocking," March 17, 2006, http://en.wikipedia.org/wiki/Kerr-lens_modelocking, last accessed March, 2006.

88. Coherent Inc., *Mira 900 Modelocked Ti:Sapphire Lasers*, 2002, http://www.coherent.com/downloads/MIRA900.pdf, last accessed March, 2006.

89. M. Maier, W. Kaiser and J. A. Giordmaine, "Intense light bursts in the stimulated Raman effect," *Physical Review Letters*, 17, 1275, 1966.

90. J. H. Chung and A. M. Weiner, "Ambiguity of ultrashort pulse shapes retrieved from the intensity autocorrelation and the power spectrum," *IEEE Journal of Selected Topics in Quantum Electronics*, 7, 656, 2001.

91. D. J. Kane and R. Trebino, "Characterization of arbitrary femtosecond pulses using frequency-resolved optical gating," *IEEE Journal of Quantum Electronics*, 29, 571, 1993.

92. R. Trebino and D. J. Kane, "Using phase retrieval to measure the intensity and phase of ultrashort pulses: frequency-resolved optical gating," *Journal of the Optical Society of America A*, 10, 1101, 1993.

93. D. N. Fittinghoff, K. W. DeLong, R. Trebino and C. L. Ladera, "Noise sensitivity in frequency-resolved optical-gating measurements of ultrashort pulses," *Journal of the Optical Society of America B,* 12, 1955, 1995.

94. V. A. Zubov and T. I. Kuznetsova, "Solution of the phase problem for time-dependent optical signals by an interference system," *Soviet. Journal of Quantum Electronics*, 21, 1285, 1991.

95. V. Wong and I. A. Walmsley, "Analysis of ultrashort pulse-shape measurement using linear interferometers," *Optics Letters*, 19, 287, 1994.

96. T. M. Shuman, M. E. Anderson, J. Bromage, C. Iaconis, L. Waxer and I. A. Walmsley, "Real-time SPIDER: ultrashort pulse characterization at 20 Hz," *Optics Express*, 5, 134, 1999.

97. M. Takeda, H. Ina and S. Kobayashi, "Fourier-transform method of fringe pattern analysis for computer based tomography and interferometry," *Journal of the Optical Society of America*, 72, 156, 1982.

98. K. W. DeLong, R. Trebino and D. J. Kane, "Comparison of ultrashort-pulse frequency-resolved-optical-gating traces for three common beam geometries," *Journal of the Optical Society of America B*, 11, 1595, 1994.

99. A. M. Weiner, "Femtosecond pulse shaping using spatial light modulators," *Review of Scientific Instruments*, 71, 1929, 2000.

100. W. S. Warren, R. Rabitz and M. Dahleh, "Coherent control of chemical reactions: the dream is alive," *Science*, 259, 1581, 1993.

101. C. W. Siders, J. L. W. Siders, A. J. Taylor, S. G. Park, M. R. Melloch and A. M. Weiner, "Generation and characterization of terahertz pulse trains from biased, large-aperture photoconductors," *Optics Letters,* 24, 241, 1999.

102. D. Yelin, D. Meshulach and Y. Silberberg, "Adaptive femtosecond pulse compression," *Optics Letters,* 22, 1793, 1997.

103. A. Efimov, M. D. Moores, N. M Beach, J. L. Krause and D. H. Reitze, "Adaptive control of pulse phase in a chirped-pulse amplifier," *Optics Letters,* 23, 1915, 1998.

104. E. Zeek, K. Maginnis, S. Backus, U. Russek, M. Murnane, G. Mourou, H. Kapteyn and G. Vdovin, "Pulse compression by use of deformable mirrors," *Optics Letters,* 24, 493, 1999.

105. F. Verluise and V. Laude, Z. Cheng, C. Spielmann and P. Tournois, "Amplitude and phase control of ultrashort pulses by use of an acousto-optic programmable dispersive filter: pulse compression and shaping," *Optics Letters*, 25, 575, 2000.

106. A. Monmayrant, M. Joffre, T. Oksenhendler, R. Herzog, D. Kaplan and P. Tournois, "Time-domain interferometry for direct electric-field reconstruction by use of an acousto-optic programmable filter and a two- photon detector," *Optics Letters*, 28, 278, 2003.

107. L. Gallmann, D. H. Sutter, N. Matuschek, G. Steinmeyer, U. Keller, C. Iaconis and I. A. Walmsley, "Chracterization of sub-6-fs optical pulses with spectral phase Interferometry for direct electric-field reconstruction," *Optics Letters*, 24, 1314, 1999.

108. A. M. Weiner, D. E. Leaird, J. S. Patel and J. R. Wullert, "Programmable shaping of femtosecond optical pulses by use of 128 element liquid crystal phase modulator," *IEEE Journal of Quantum Electronics*, 28, 908, 1992.

109. R. R. Alfano and S. L. Shapiro, "Observation of self-phase modulation and small-scale filaments in crystals and glasses," *Physical Review Letters*, 24, 592, 1970.

110. A. Apolonski, B. Povazay, A. Unterhuber, W. Drexler, W. Wadsworth, J. Knight and P. Russell, "Spectral shaping of supercontinuum in a cobweb photonic-crystal fiber with sub-20-fs pulses ," *Journal of the Optical Society of America B*, 19, 2165, 2002.

111. R. S. Judson and H. Rabitz, "Teaching lasers to control molecules," *Physical Review Letters*, 68, 1500, 1992.

112. A. M. Weiner, J. P. Heritage, R. J. Hawkins, R. N. Thurston, E. M. Kirschner, D. E. Leaird and W. J. Tomlinson, "Experimental observation of the fundamental dark soliton in optical fibers," *Physical Review Letters*, 61, 2445, 1988.

113. A. P. Heberle, J. J. Baumberg and K. Köhler, "Ultrafast coherent control and destruction of excitons in quantum wells," *Physical Review Letters*, 75, 2598, 1995.

114. R. Fanciulli, A. M. Weiner, M. M. Dignam, D. Meinhold and K. Leo, "Coherent control of Bloch oscillations by means of optical pulse shaping," *Physical Review B*, 71, 153304, 2005.

115. G. Boyer, "Shock-wave-assisted ultrafast soliton generation," *Optics Letters*, 25, 601, 2000.

116. A. Rundquist, A. Efimov and D. H. Reitze, "Pulse shaping with the Gerchberg-Saxton algorithm," *Journal of the Optical Society of America B*, 19, 2468, 2002.

117. S. Sastry and M. Bodson, *Adaptive Control: Stability, Convergence, and Robustness*, Prentice-Hall, Englewood Cliffs, 1994.

118. M. Mitchell, *An Introduction to Genetic Algorithms*, MIT Press, Cambridge, 1996.

119. B. Schenkel, J. Biegert, U. Keller, C. Vozzi, M. Nisoli, G. Sansone, S. Stagira, S. De Silvestri and O. Svelto, "Generation of 3.8-fs pulses from adaptive compression of a cascaded hollow fiber," *Optics Letters*, 28, 1987, 2003.

120. K. Ohno, T. Tanabe and F. Kannari, "Adaptive pulse shaping of phase and amplitude of an amplified femtosecond pulse laser by direct reference to frequency-resolved optical gating traces," *Journal of the Optical Society of America B,* 19, 2781, 2002.

121. D. Meshulach, D. Yelin and Y. Silberberg, "Adaptive real-time femtosecond pulse shaping," *Journal of the Optical Society of America B*, 15, 1615, 1998.

122. D. H. Reitze, S. Kazamias, F. Weihe, G. Mullot, D. Douillet, F. Aug, O. Albert, V. Ramanathan, J. P. Chambaret, D. Hulin and P. Balcou, "Enhancement of high order harmonic generation at tuned wavelengths via adaptive control," *Optics Letters*, 29, 86, 2004.

123. F. G. Omenetto, A. J. Taylor, M. D. Moores and D. H. Reitze, "Adaptive control of nonlinear femtosecond pulse propagation in optical fibers," *Optics Letters*, 26, 938, 2001.

124. A. Efimov, A. J. Taylor, F. G. Omenetto and E. Vanin, "Adaptive control of femtosecond soliton self-frequency shift in fibers," *Optics Letters*, 29, 271, 2004.

125. B. Povazay, K. Bizheva, A. Unterhuber, B. Hermann, H. Sattmann, A. F. Fercher and W. Drexler, "Submicrometer axial resolution optical coherence tomography," *Optics Letters*, 27, 1800, 2002.

126. L. Nugent-Glandorf and T. T. Perkins, "Measuring 0.1-nm motion in 1 ms in an optical microscope with differential back-focal-plane detection," *Optics Letters*, 29, 2611, 2004.

127. B. R. Washburn, S. E. Ralph and R. S. Windeler, "Ultrashort pulse propagation in air-silica microstructure fiber," *Optics Express*, 10, 575, 2002.

128. I. G. Cormack, D. T. Reid, W. J. Wadsworth, J. C. Knight and P. S.. J. Russell, "Observation of soliton self-frequency shift in photonic crystal fibre," *Electronics Letters*, 384, 167, 2002.

129. D. V. Skryabin, F. Luan, J. C. Knight and P. S. J. Russell, "Soliton self-frequency shift cancellation in photonic crystal fibers," *Science*, 301, 1705, 2003.

130. K. S. Abedin and F. Kubota, "Widely tunable femtosecond soliton pulse generation at a 10-GHz repetition rate by use of the soliton self-frequency shift in photonic crystal fiber," *Optics Letters*, 28, 1760, 2003.

131. R. Fork, C. Brito Cruz, P. Becker and C. Shank, "Compression of optical pulses to six femtoseconds by using cubic phase compensation," *Optics Letters*, 12, 483, 1987.

132. M. Nisoli, S. D. Silvestri and O. Svelto, "Generation of high energy 10 fs pulses by a new pulse compression technique," *Applied Physics Letters*, 68, 2793, 1996.

133. M. Nisoli, S. D. Silvestri, O. Svelto, R. Szipcs, K. Ferencz, C. Spielmann, S. Sartania and F. Krausz, "Compression of high-energy laser pulses below 5 fs," *Optics Letters*, 22, 522, 1997.

134. S. O. Konorov , E. E. Serebryannikov , A. A. Ivanov , D. A. Akimov , M. V. Alfimov , M. Scalora and A. M. Zheltikov, "Self-compression of subgigawatt femtosecond laser pulses in a hollow photonic-crystal fiber," *Journal of Experimental and Theoretical Physics Letters*, 81, 58, 2005.

135. R. Szipöcs, K. Ferencz, C. Spielmann and F. Krausz, "Chirped multilayer coatings for broadband dispersion control in femtosecond lasers," *Optics Letters*, 19, 201, 1994.

136. F. X. Kärtner, N. Matuschek, T. Schibli, U. Keller, H. A. Haus, C. Heine, R. Morf, V. Scheuer, M. Tilsch and T. Tschudi, "Design and fabrication of double-chirped mirrors," *Optics Letters*, 22, 831, 1997.

137. J. M. Dudley and S. Coen, "Coherence properties of supercontinuum spectra generated in photonic crystal and tapered optical fibers," *Optics Letters*, 27, 1180, 2002.

138. M. Adachi, K. Yamane, R. Morita and M. Yamashita, "Pulse compression using direct feedback of the spectral phase from photonic crystal fiber output without the need for the Taylor expansion method," *IEEE Photonic Technology Letters*, 16, 1951, 2004

139. M. Adachi, K. Yamane, R. Morita and M. Yamashita, "Sub-5-fs pulse compression of laser output using photonic crystal fiber with short zero-dispersion wavelength," *Japanese Journal of Applied Physics*, 44, 1423, 2005.

140. M. A. Foster and A. L. Gaeta, Q. Cao and R. Trebino, "Soliton-effect compression of supercontinuum to few-cycle durations in photonic nanowires," *Optics Letters*, 13, 6848, 2005.

141. P. J. Roberts, B. J. Mangan, H. Sabert, F. Couny, T. A. Birks, J. C. Knight and P. S. J. Russell, "Control of dispersion in photonic crystal fibers," *Journal of Optical and Fiber Communications Reports*, 2, 435, 2005.

142. A. Ferrando, E. Silvestre, J. J. Miret, J. A. Monsoriu, M. V. Andŕes and P. St. J. Russell, "Designing a photonic crystal fibre with flattened chromatic dispersion," *Electronics Letters*, 35, 325, 1999.

143. A. Ferrando, E. Silves tre, J. J. Miret and P. Andr´es, “Nearly zero ultraflattened dispersion in photonic crystal fibers,” *Optics Letters*, 25, 790, 2000.

144. K. Saitoh, M. Koshiba, T. Hasegawa and E. Sasaoka, “Chromatic dispersion control in photonic crystal fibers: Application to ultra-flattened dispersion,” *Optics Express*, 11, 843, 2003.

145. F. Poli, A. Cucinotta, S. Selleri and A. H. Bouk, “Tailoring of flattened dispersion in highly nonlinear photonic crystal fibers,” *IEEE Photonics Technology Letters*, 16, 1065, 2004.

146. L. Shen, W. Huang and S. Jian, “Design of photonic crystal fibers for dispersion-related applications,” *Journal of Lightwave Technology*, 21, 1644, 2003.

147. W. Reeves, J. Knight, P. Russell and P. Roberts, “Demonstration of ultra-flattened dispersion in photonic crystal fibers,” *Optics Express*, 10, 609, 2002.

148. K. P. Hansen, “Dispersion flattened hybrid-core nonlinear photonic crystal fiber,” *Optics Express*, 11, 1503, 2003.

149. A. Ferrando, E. Silvestre, P. Andrés, J. J. Miret and M. V. Andrés, “Designing the properties of dispersion-flattened photonic crystal fibers,” *Optics Express*, 9, 687, 2001.

150. E. Kerrinckx, L. Bigot, M. Douay and Y. Quiquempois, “Photonic crystal fiber design by means of a genetic algorithm,” *Optics Express*, 12, 1990, 2004.

BIOGRAPHICAL SKETCH

Shengbo Xu was born in Xinjiang, China, in May 1975. He received the degree of Bachelor of Science in physics in 1997 and the degree of Bachelor of Engineering in computer science in 1998 from the University of Science and Technology of China, Hefei, China. In 2000, he received the degree of Master of Science in physics from the University of Science and Technology of China. Since then, he has been working in the ultrafast optics group under the advisement of Professor David Reitze in Department of Physics, University of Florida.